Preparation and characterisation of magnetic single and double barrier junctions

PhD thesis in physics
by **Andy Thomas**
born May 14, 1975
in Minden, Germany

University of Bielefeld
Department of physics
Nano device group

August 26, 2003

Declaration

I wrote this thesis by myself and used none but the indicated resources.

Bielefeld, August 26, 2003

(Andy Thomas)

Reviewers:

Prof. Dr. Günter Reiss
Prof. Dr. Dario Anselmetti

Date of submission: August 26, 2003

Preface

In recent years, a lot of new developments in solid state physics have been related to the field of spin electronics. The spin electronic or spintronic device not only uses the charge of electrons to carry information, but also their spin. For example, this allows one to use magnetic fields to manipulate the output in logic circuits. Because these magnetic fields can be induced by electric currents on the chip, it is possible to fully implement these new devices in conventional electronics.

One can think of several ways to build spin electronic devices. One approach does not use conventional electronic such as transistors at all. COWBURN showed how to get all basic functions (a branch of one into two signal lines, a crossover of two signal lines, a NOT gate, and an OR gate) using only magnetic logics in specially structured Iron-Nickel lines. With these ingredients it is possible to build any logic circuit.

The second more conventional approach uses spin polarised currents in CMOS environments. This is easier to implement, because only electrical signals are used. The challenge of this approach is to get and to manipulate spin polarised currents. The easiest way of getting these spin polarised currents is by using a device with an unpolarised current input and a polarised output. Therefore, this is called a spin filter device, often realised as a tunnel barrier with different opacity for each spin state.

The approach investigated in this thesis is the use of a ferromagnetic electrode in tunnel barrier junctions. Because the density of states in ferromagnetic electrodes is not equal for spin up and spin down, the current after tunnelling through the barrier is spin polarised. The spin direction usually does not change during the tunnelling process.

This method is a way to create spin polarised currents, but the question, how to manipulate them remains. To solve that problem, two ferromagnetic electrodes are used at both sides of the barrier. Then, two different alignments of the magnetisations of the two electrodes are possible: parallel and anti-parallel. Investigations of the density of states in both electrodes show that the resistance of this device is related to the orientation of the magnetisation of the ferromagnets. Usually the resistance is higher in the anti-parallel case.

Because the resistance is an electrical signal, it is easy to read out this information with a CMOS environment, for example. This leads to many possible applications such as hard disk read heads, magnetic random access memories or logic circuits.

iv
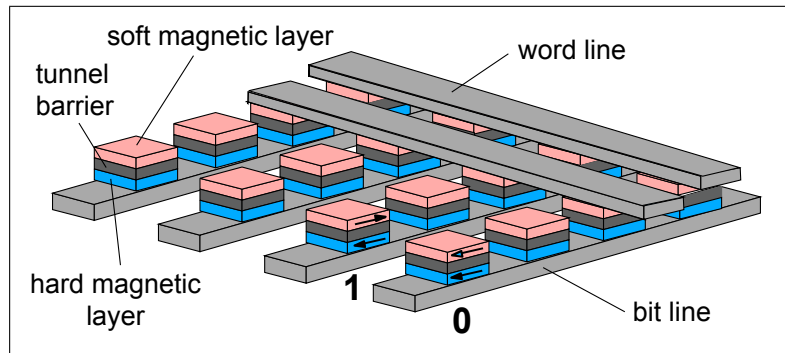
Figure 1: Scheme of a MRAM cell based on magnetic tunnel junctions. The magnetic field of a current in a bit and word line is used to switch an addressed bit (junction). The lines also measure the resistance of the magnetic tunnel junctions. Original picture by courtesy of G. Reiss.

Applications

One application that uses the so called tunnel magnetoresistance is, as mentioned above, a read head in hard disk drives. A read head converts the signal from the stray field of each bit into an electrical signal. The stray field switches the magnetic state in the tunnel magnetoresistance device. The sensitivity of this novel device (up to $50\,\%$ resistance change at only a few Oerstedt at room temperature) is higher than in any conventional magnetic field sensor. This leads to higher storage densities, because it is already conventionally possible to write at higher densities than to read.

Many companies such as IBM, Infinion and Motorola are developing magnetic random access memories called MRAM. Figure 1 shows the principle of the device. This device combines the advantages of hard disk and random access memories:

- it is non volatile (no refresh cycle necessary)

- all signals, reading and writing, are purely electrical leading to

    - an easy integration into the established CMOS technology
    - very short reading and writing times
    - decreased failure rate, because of no mechanical parts

- low power consumption for reading and writing process (no refresh cycle)

- good scalability down to nanometer scale lateral dimensions

In summary, this combined (hard disk = RAM) memory has huge advantages in a personal computer for example. In a further step, it is possible to replace even the logic circuits in a computer by devices based on the tunnel magneto resistance effect. Current software runs slowly, because the central processing unit performs universal tasks. Therefore, computers

already have some specialised chips for specific functions (e.g. graphic and sound processing). A program running on a new magnetic CPU would rewire the circuit itself and run very fast. Rewiring a circuit consisting of magnetic tunnel junctions is done by switching the magnetic electrodes, which changes the logic function. This new kind of programming is called re-configurable computing.

This thesis

In this thesis the basics of tunnel magneto resistance are introduced in the first chapter. This includes a simple model which explains electron tunnelling through a thin insulating barrier, the definition of spin polarisation in relation to the tunnel magnetoresistance ratio, how to avoid artefacts by current crowding effects and exchange bias. Anyone familiar with spin polarised tunnelling can skip this chapter. More recent theoretical models are (if needed) given in the experimental part, because every section is intended to have as less references as possible.

In the second chapter, measurement tools and methods are presented. When introducing the transport and magnetic measurements, the structural analysis and the preparation tools, the thesis focuses on the equipment. It is intended to show anyone familiar with these techniques the limitations and the resolution of the measurements.

Next, the experimental results are presented. They are divided into two chapters: one concerning junctions with a single tunnel barrier, and one about those using two tunnel barriers. Chapter 3 concerning single barrier junctions was included for several reasons. First, it was necessary to address certain physical questions that existed at the beginning of this investigation. Second, in order to prepare double barrier junctions and other devices (e.g. bio-sensor, magnetic logic) of which tunnel junctions are components, one must understand the fundamental component - the single tunnel junction - and establish reliable, reproducible ways of preparing it. The creation and use of double barrier junctions can be built upon this solid foundation.

The chapter about double barrier junctions demonstrates the preparation of junctions with two tunnel barriers in two different ways. It shows the behaviour of these junctions and whether they can be described by a serial connection of two junctions with one tunnel barrier. Besides possible spin accumulation and ballistic effects, physical systems with a very short length scale in at least one dimension are always very interesting. In that case quantum well states might occur. Then, summary, outlook, references and acknowledgements conclude this thesis.

Publications

- J. Schmalhorst, A. Thomas, M. Justus, G. Reiss, and H. Brückl: *Evolution of barrier properties in magnetic tunnel junctions by annealing*, Tagungsband Statusseminar Magnetoelektronik, 325-327 (2000)

- J. Schmalhorst, H. Brückl, M. Justus, A. Thomas, G. Reiss, M. Vieth, G. Gieres, and J. Wecker: *Evolution of the dielectric breakdown in* $Co/Al_2O_3/Co$ *junctions by annealing*, J. Appl. Phys. **89**, 586-589 (2001)

- G. Reiss, H. Brückl, J. Schmalhorst, and A. Thomas: *Stability of magnetic tunnel junctions*, Springer Lecture Notes in Physics **91**, 2593-2613 (2002)

- G. Reiss, H. Brückl, A. Hütten, J. Schmalhorst, M. Justus, A. Thomas, and S. Heitmann: *Spinelectronics and its applications*, Phys. Stat. Sol. B **236**, 289-302 (2003)

- S. Kämmerer, S. Heitmann, D. Meyners, D. Sudfeld, A. Thomas, A. Hütten, and G. Reiss: *Room-temperature preparation and magnetic behavior of* Co_2MnSi *thin films*, J. Appl. Phys. **93**, 7945-7947 (2003)

- W. K. Park, J. S. Moodera, J. Taylor, M. Tondra, J. M. Daughton, A. Thomas, and H. Brückl: *Noise properties and comparison of magnetic and non-magnetic tunnel junctions*, J. Appl. Phys. **93**, 7020-7022 (2003)

- H. Brückl, A. Thomas, J. Schotter, J. Bornemeier, and G. Reiss: *New developments with Magnetic Tunnel Junctions*, Springer, Advances in Solid State Physics, accepted for publication

- A. Thomas, H. Brückl, J. Schmalhorst, and G. Reiss: *Temperature and bias voltage dependence of* $CoFe/AlO_x/Py/AlO_x/CoFe$ *double barrier junctions*, IEEE Trans. Magn., accepted for publication

- A. Thomas, H. Brückl, M. D. Sacher, J. Schmalhorst, and G. Reiss: *Aluminum oxidation by a remote electron cyclotron resonance plasma in magnetic tunnel junctions*, J. Vac. Sci. Technol. B, accepted for publication

- M. Urbaniak, J. Schmalhorst, A. Thomas, H. Brückl, G. Reiss, T. Lucinski, and F. Stobiecki: *Unidirectional anisotropy in* MnIr/CoFe/Al + Ox/NiFe *multilayer systems*, Phys. Stat. Sol. B, accepted for publication

- A. Thomas, H. Brückl, and G. Reiss: *Bulk and interface contributions to the spin polarization decay in magnetic tunnel junctions with composite electrodes*, to be submitted

Conferences

- A. Thomas, M. Justus, J. Schmalhorst, H. Brückl, and G. Reiss: *JMR in ferromagnetic double tunnel junctions with different Co interlayer thicknesses*, Symposium on Spin-Electronics 2000 Halle, PB-17

- A. Thomas, M. Justus, J. Schmalhorst, H. Brückl, and G. Reiss: *Tunnelmagnetowiderstand in* Al_2O_3-*Doppelbarrieren*, DPG Frühjahrstagung 2000 Regensburg, AM 18.8

- A. Thomas, J. Schmalhorst, M. Justus, H. Brückl, and G. Reiss: *Präparation von Tunnelbarrieren in magnetischen Tunnelelementen durch mikrowellenunterstützte Plasmaoxidation*, DPG Frühjahrstagung 2002 Regensburg, MA 7.2

- A. Thomas, H. Brückl, J. Schmalhorst, and G. Reiss: *Temperature and bias voltage dependence of CoFe/ AlO_x/ Py/ AlO_x/ CoFe double barrier junctions*, Intermag 2003 Boston, GD-11

Contents

Chapter 1

Basics

Since the tunnel magnetoresistance effect was discovered in 1975 [1], the interest in magnetic tunnel junctions has been renewed after the discovery of another novel magnetoresistive effect: the giant magnetoresistance [2, 3]. Because the tunnel magnetoresistance value has been improved significantly at room temperature [4, 5], magnetic tunnel junctions became a promising candidate for sensors and memories [6], e.g. in recording heads for hard discs or magnetic random access memory devices [7].

1.1 Tunnel magnetoresistance

If a magnetic field is applied to a device with two ferromagnetic materials separated by an insulator (called Magnetic Tunnel Junction, MTJ), the resistance changes with changing the relative orientation of the two magnetisations. This is called Tunnel Magneto Resistance, or TMR. Figure 1.1 shows schematically a TMR device with higher resistance at anti-parallel alignment.

It is possible to change the relative orientation of the two magnetisations if the hysteresis
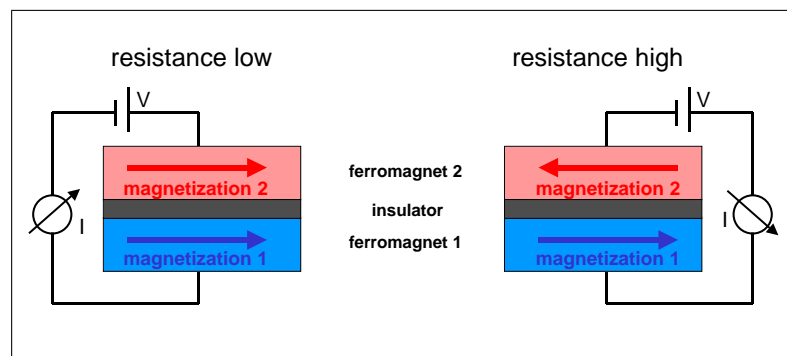
Figure 1.1: Scheme of a TMR element: The resistance of the device is higher if the magnetisations of the two ferromagnets are aligned anti-parallel.
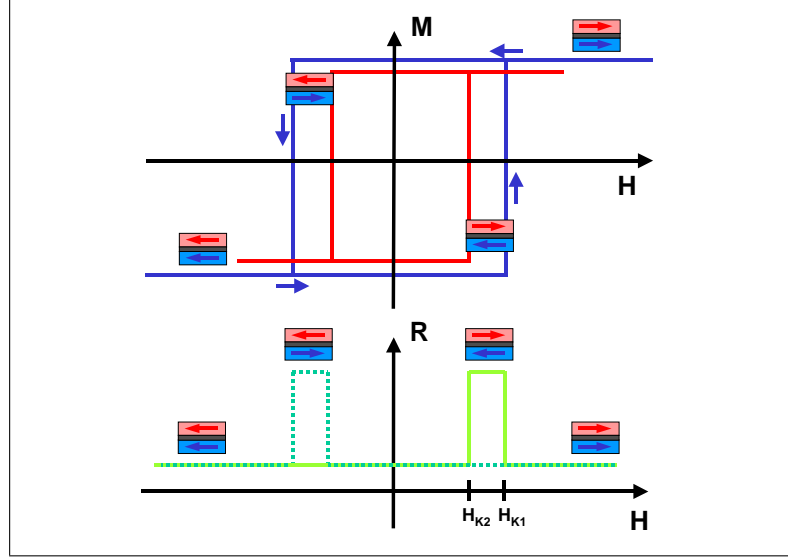
Figure 1.2: Hysteresis loops and corresponding resistance values (increasing field light green and decreasing field broken green line) of the TMR device shown in figure 1.1.

loops of the two ferromagnetic layers are not exactly identical. A simple example is shown in figure 1.2: Two rectangular hysteresis loops with different coercive fields and a layer stack identical to figure 1.1.

Starting at high negative values of the field H, the magnetisations of both layers are parallel in field direction and the resistance $R = R^{\downarrow\downarrow}$. If the coercive field H_{K2} of the magnetically softer layer is reached the magnetisation switches to anti-parallel alignment ($H_{K1} > H > H_{K2}$) and the resistance R increases to $R^{\uparrow\downarrow}$. Further increase of the field ($H > H_{K1}$) results in switching of the second layer and the resistance drops to its initial value $R^{\uparrow\uparrow}$, indicated by the light green curve for increasing field. Starting from this point and decreasing the field leads to the symmetric broken green curve. Because the magnetisation of both layers is changed this is called *major loop*. If only the magnetisation of one layer is changed it is called *minor loop*.

With these two resistance values, it is possible to define the tunnel magneto resistance ratio (TMR ratio):

$$\text{TMR} \equiv \frac{R^{\uparrow\downarrow} - R^{\uparrow\uparrow}}{R^{\uparrow\uparrow}} \qquad \text{JMR} \equiv \frac{R^{\uparrow\downarrow} - R^{\uparrow\uparrow}}{R^{\uparrow\downarrow}} \qquad (1.1)$$

$R^{\uparrow\uparrow}$ is normally lower than $R^{\uparrow\downarrow}$ and TMR/ JMR are mostly positive. By the same reason TMR is higher than JMR (Junction Magneto Resistance). So TMR is called the optimistic and JMR the pessimistic value. Because this is an optimistic work, the TMR value is always used. A second reason: the parallel state is always clearly defined in saturation. The mean area resistance R_A and the current density j are defined:

$$R_A \equiv \frac{R^{\uparrow\uparrow} + R^{\uparrow\downarrow}}{2} \times A \qquad j \equiv \frac{I}{A} \qquad (1.2)$$

with the junction area A and the current I. This definition is used because the values of R_A and j are independent of the junction area A (at a certain voltage).

1.2 Electrical characterisation of magnetic tunnel junctions

The concepts of electron tunnelling [8, 9] are described in this section, as far as it is necessary to understand the tunnelling process in magnetic tunnel junctions. The possibility of electron tunnelling through a potential barrier was already known more than 60 years ago and is of purely quantum-mechanical origin.

The most obvious approach to investigate this effect is a metal insulator metal structure (e.g. $\mathrm{Cu} - \mathrm{Al_2O_3} - \mathrm{Cu}$), called tunnel junction. In the classical model an electron encountering the insulator can't pass it, if the energy of the electron is lower than the potential barrier. In the quantum mechanical picture, the electron wave function is reflected at the potential step, but a certain "amount" of the wave function penetrates the insulator. The probability of being found in the counter-electrode exponentially decreases with the insulator thickness.

Normally, tunnel junctions are characterised by investigating the current as a function of the bias voltage at the junction. With this bias voltage V, the Fermi level of one side is shifted by eV, e is the electron charge. The current from one electrode trough the barrier to the other electrode $I_{1,2}$ is determined by five factors: the density of states (DOS) at a given energy (E) in the first electrode $\rho_1(E)$, the DOS at the same energy (plus the energy the electron gains by the applied voltage) in the second electrode $\rho_2(E + eV)$, the probability of transmission through the barrier $|T|^2$, the occupation probability of the states in the first electrode $f(E)$, and the probability that the states in the second electrode are empty $1 - f(E + eV)$, where $f(E)$ is the Fermi-Dirac function. In summary, an electron with a given energy tunnels from one side of the barrier with a certain probability in an empty state on the other side of the barrier. The resulting current is given by:

$$I_{1,2} = \int_{-\infty}^{\infty} \rho_1(E)\rho_2(E + eV)|T(E)|^2 f(E)(1 - f(E + eV))dE \qquad (1.3)$$

Electrons are also tunnelling in the opposite direction, the total current is given by: $I = I_{1,2} - I_{2,1}$. To simplify the calculation (only this 'simplification' makes the calculation possible) 3 different approaches have been used. The approximation used by SIMMONS is to replace the barrier height by an average height with a certain thickness [10, 11, 12]. Already this simple model leads to the correct dependence of the resistance R on the barrier thickness d and the square root of the barrier height ϕ: $R \propto d\sqrt{\phi}$. STRATTON et. al. expanded the Matrix element $|T|^2$ for electrons close to the Fermi energy [13, 14, 15], leading to awkward expressions for the current. BRINKMAN investigated two extreme cases to explain the asymmetry of measured IV curves [16]. This model is also used in this thesis. Therefore, it is explained in more detail.

BRINKMAN calculated the tunnelling current for a trapezoidal barrier numerically by a computer. The conductance G is determined by direct differentiation of the result either in the WKB approximation [17] or assuming sharp boundaries between the electrodes and the insulator [18]. The first terms of the WKB approximation leads to a conductance of $G = A \cdot V^2 + B \cdot V + C$. Otherwise, if the conductance is measured, it is possible to determine the barrier parameters: effective height $\bar{\varphi}$, thickness d, and asymmetry $\Delta\varphi$ [19]. To do that, the *IV* curve is numerically differentiated, the result is fitted (Marquard-Levenberg [20]), and the 3 parameters A,B, and C are received, respectively the barrier parameters:

$$
\begin{aligned}
\bar{\varphi}^2 &= \frac{\mathrm{e}^2 C}{32A} \ln^2\left(\frac{\mathrm{h}^3}{\sqrt{2}\pi\mathrm{e}^3\mathrm{m_{eff}}}\sqrt{AC}\right) \\
d &= -\frac{\hbar}{8\sqrt{\bar{\varphi}}\mathrm{m_{eff}}} \ln\left(\frac{\mathrm{h}^3}{\sqrt{2}\pi\mathrm{e}^3\mathrm{m_{eff}}}\sqrt{AC}\right) \\
\Delta\varphi &= -\frac{12\hbar B}{\sqrt{2\mathrm{m_{eff}}}\mathrm{e}C}\frac{\bar{\varphi}^{\frac{3}{2}}}{d}
\end{aligned}
\tag{1.4}
$$

$\mathrm{m_{eff}}$ is the effective electron mass, it is set to 0.4 [21]. All barrier parameters presented in this thesis are determined by an *IV* curve fit and equation 1.4. This model is used, because it takes the important asymmetry into account. If a $Cu - Al_2O_3 - Al$ junction is investigated, the SIMMONS model discards the difference between the two metals. BRINKMAN on the other hand neglects the image force. But he also showed that the image force only reduces the mean barrier height and rounds off the edges of the potential wall. This has the effect of increasing the conductance, but does not qualitatively change the overall shape of the $G(V)$ curve.

All these approaches neglect any dependence of the transport characteristics on the electronic density of states of the electrodes. At first glance, equation 1.3 looks like taking the DOS of the two electrodes into account. But a closer look leads to the result, that $|T|^2$ is reciprocally proportional to these density of states and, therefore, cancels the dependence. But this means that no tunnel magneto-resistance is possible, because the current for both (parallel and anti-parallel) alignments is the same, even if ferromagnetic electrodes are used.

To solve this discrepancy, many body interactions have to be taken into account. It is not possible to explain the results of superconductivity measurements (Cooper coupling [22, 23]) as well as the tunnel magneto-resistance (ferromagnetic interactions) in a single particle picture [8, 18], these interactions change $|T|^2$ and ρ in equation 1.3.

1.3   Spin polarisation vs. tunnel magneto resistance ratio

In his seminal work, GIAVER (Nobel-Prize 1973) measured the energy gap in a superconductor/ insulator/ metal junction ($Pb - Al_2O_3 - Al$) [24, 25]. Later, MESERVEY and

TEDROW investigated the spin polarised tunnelling in ferromagnet/ insulator/ superconductor junctions (e.g. $Ni - Al_2O_3 - Al$). If a magnetic field is applied at these junctions, Zeeman splitting of the quasi-particle states occurs. The DOS in the superconductor is now split in the spin up DOS and the spin down DOS. The splitting can be seen as peaks in the conductance vs. bias voltage plots. Without taking spin orbit scattering into account, it is possible to define the spin polarisation as the relative height of the conductance peaks. Additionally, MESERVEY and TEDROW showed at superconductor-insulator-superconductor junctions, that no spin flips take place during tunnelling [26].

The first time, tunnel magneto-resistance was measured in magnetic tunnel junctions was 1975 by JULLIERE [1]. He already introduced a simple model to explain the TMR: At low voltages electrons tunnel without spin flip through the insulator. Define a and $á$ as the fraction of electrons whose magnetic moments are parallel to the magnetisation of the first and the second ferromagnet. The spin polarisation of the two ferromagnets is defined as $P \equiv 2a - 1$ and $\acute{P} \equiv 2á - 1$. This and the earlier work of MESERVEY and TEDROW [27] leads to a relative conductance variation of

$$\text{TMR} = \frac{2P\acute{P}}{1 - P\acute{P}} \qquad \text{JMR} = \frac{2P\acute{P}}{1 + P\acute{P}} \qquad (1.5)$$

The tunnelling spin polarisation is often used in a magnetic tunnel junction to separate the contributions of the two ferromagnetic electrodes from each other. This spin polarisation is not the same spin polarisation determined by other techniques like Andreev reflection [28] or photoemission. Not only the DOS of the electrodes is measured, but also the matrix element $|T|^2$ of equation 1.3.

A closer look at the spin polarisation values in MTJs with different materials at both sides of the tunnel barrier reveals a wrong sign of the polarisation of the 3d-ferromagnets. At the Fermi level 3d ferromagnets show a larger minority contribution to the DOS [29], the sign of the spin polarisation should be negative. Although this is still discussed, an explanation is given by STEARNS [30]: First, in 3d ferromagnets the s bands are spin polarised with opposite sign via hybridisation with d bands. Second, the s electrons have a higher transmission probability through the barrier, because the probability depends on the effective mass of the electrons. Furthermore, in barriers of a few nanometer the transmissions probability has a stronger influence on the tunnelling current. And this finally explains the opposite sign of the spin polarisation in tunnelling experiments.

But that model is still too simple. The interfacial DOS of a ferromagnet at the barrier differs from the bulk DOS. The tunnel conductance and also the sign of the spin polarisation depends on the binding between the barrier and the electrode atoms [31]. The reader more interested to the problems concerning this topic is encouraged to have a closer look at [32] and the cited original literature. Nevertheless, while magnetic tunnel junctions are going to be used as MRAM memories in the next years, a deep understanding of the fundamental physical mechanisms is still lacking. Especially the connection of the spin-polarisation of the different electron bands to the measured TMR ratio is not finally answered.
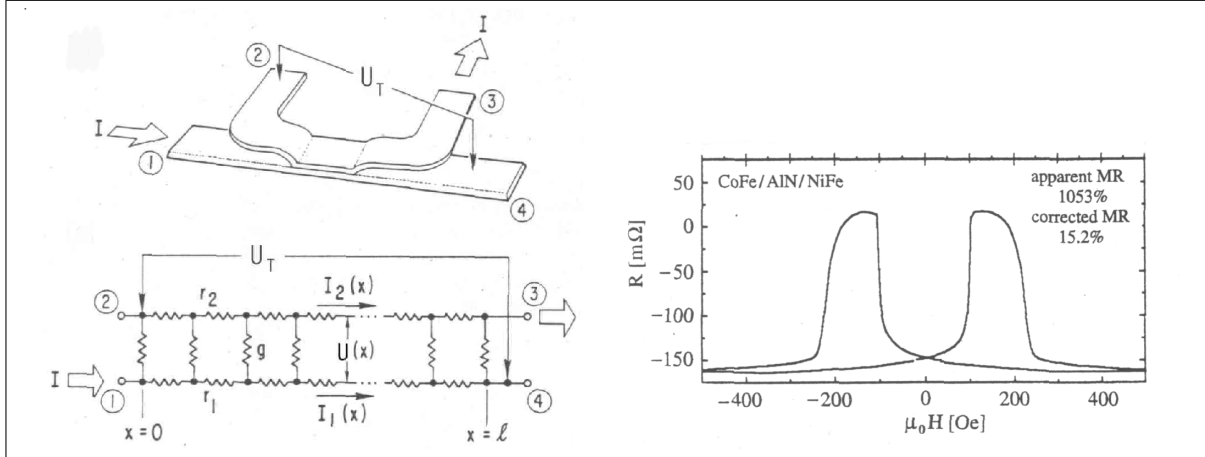
Figure 1.3: 4 probe resistance measurement of a tunnel junction with high lateral resistance. Left: Sketch of the measurement as a network of many resistors [33]. Right: Real measurement with its apparent and corrected TMR ratio [34].

## 1.4   Geometrical enhancement of the TMR value

It is very important to take influence of measurement geometry on the resistance into account, also called 'current crowding effect'. Geometrical enhancement can lead to absolutely wrong results. The sketch in figure 1.3 shows a 4 probe measurement of a tunnel junction. The current I flows from probe 1 to 3 and the voltage U_T is measured between 2 and 4. Normally this avoids the measurement of the line resistors to the junction, i.e. only the resistance of the junction itself is determined (if the resistance of the voltage meter is infinite).

PEDERSON figured out that a finite film resistance can't be neglected [33], because most of the current follows the path of lowest resistance. If the resistance of the tunnel barrier is lower than the resistance of the electrode, the potential of the electrodes is not uniform. Then, most of the electrodes tunnel immediately through the outermost part of the tunnel barrier. Assuming a uniform thickness of films and insulator, it is possible to calculate the measured resistance R_m and the result is:

$$R_m = \alpha \ell R_T \left[\frac{1}{\sinh(\alpha \ell)} + \frac{2R_2}{R_1 \left(1 + R_2/R_1\right)^2} \tanh\left(\frac{\alpha \ell}{2}\right) \right] - \frac{R_1 R_2}{R_1 + R_2} \qquad (1.6)$$

$R_1 = r_1 \ell$ and $R_2 = r_2 \ell$ are the film resistances along the junction, ℓ is the junction length, $R_T = 1/g\ell$ is the tunnelling resistance and $(\alpha \ell)^2 = (R_1 + R_2)/R_T$. Because the last term in equation 1.6 is negative, it is possible to measure even negative resistances. Together with equation 1.1 this leads to a wrong TMR ratio, as shown in figure 1.3. The situation becomes even more complex because the electrodes in MTJs are ferromagnetic. They show the anisotropic magneto resistance [35] and change their resistance with the applied field.

The MTJs in this work do not show any geometrical enhancement, because (a) the
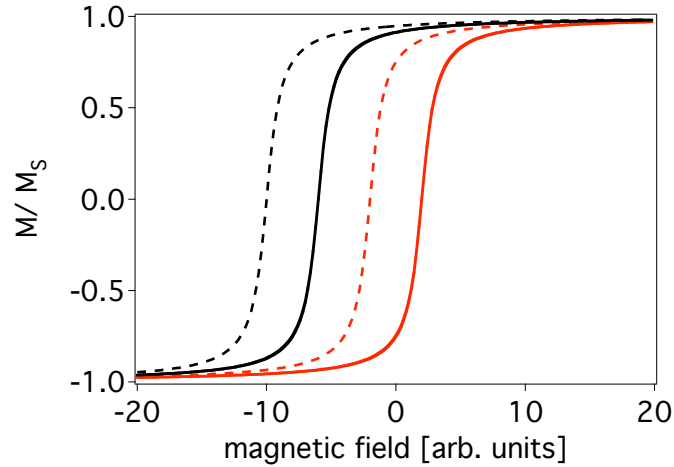
Figure 1.4: (Calculated) hysteresis loops of a ferromagnet in contact with an antiferromagnet (afm) when cooled in zero field (red) and after cooling in an applied field (black curve).

enhancement is calculated: The resistance of the junction is always $R_T \geq 30\,\Omega$ and the films have a resistance of $R_1 \simeq R_2 \equiv R \leq 1\,\Omega$. With these values equation 1.6 reduces to [33]:

$$R_m \approx R_T(1 - R/3R_T) \tag{1.7}$$

and the difference R/R_T is less than $1\,\%$. (b) MTJs are always prepared with different sizes. Because R_m is junction size dependent equal TMR ratios of all junctions prove the absence of geometrical enhancement. (c) It is also possible to measure the TMR ratio by a 2 probe technique. The TMR ratio is lower because the resistances to the junctions are also measured but the absolute resistance change has to be the same.

1.5 Exchange bias

In 1956 MEIKLEJOHN and BEAN discovered a new type of magnetic anisotropy [36, 37]. This anisotropy is the result of an interaction between an anti-ferromagnetic and a ferromagnetic material. The result is shown in figure 1.4. The hysteresis loop of a ferromagnet in contact with an anti-ferromagnet is shifted when cooled in an applied field. This shift is generally along the field axis in the negative/ opposite direction of the cooling field. This loop shift is called exchange bias.

Already MEIKLEJOHN and BEAN showed that the loop shift is equivalent to the assumption of an unidirectional anisotropy energy term:

$$E = HM_S \cos\Theta - K_u \cos\Phi + \dots$$
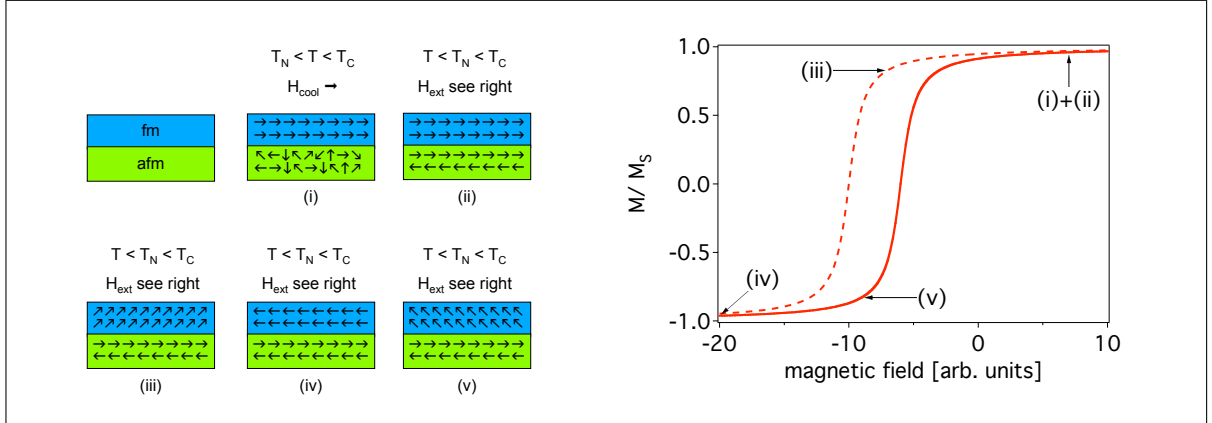
Figure 1.5: Scheme of the magnetic states during the field sweep (left) and corresponding hysteresis loop of the ferromagnet (right) with cooling field H_{cool}, external field H_{ext}, Neel-temperature of the antiferromagnet T_N and Curie-temperature of the ferromagnet T_C.

where Θ is the angle between the magnetisation and the applied magnetic field H, M_S is the saturation magnetisation of the ferromagnet and Φ is the angle between the applied field and the direction of the cooling field. If cooling field and applied field are aligned, solutions of this equation lead to an effective field $\acute{H}$:

$$\acute{H} = H - K_u/M_S$$

Thus, one can take the unidirectional anisotropy into account by using $\acute{H}$ instead of H.

In the next paragraph a simple model is given, explaining the origin of the exchange bias. Although this model is only phenomenological, the overall behaviour is correctly described. Furthermore, there is no model that gives a clear, quantitative understanding of exchange anisotropy at the nanometer (atomic) scale up to now.

Figure 1.5 describes the mechanism of exchange bias in principle. Starting at high positive fields and high temperatures (Neel-T. $T_N < T < T_C$ Curie-T.), the ferromagnet is aligned and the antiferromagnetic spins remain random. When decreasing the temperature, the spins of the afm start to align. Because of exchange interaction, the spins at the interface in contact with the ferromagnet order in one direction. The next layer aligns antiparallel and so forth. Further decreasing the temperature freezes the spin-configuration of the antiferromagnet in this state.

Figure 1.5 also shows the magnetic hysteresis loop of the ferromagnet well below the Neel-Temperature of the antiferromagnet. Assuming that the afm remains totally static (its anisotropy-energy is very large), the interface spins of the antiferromagnet couple ferromagnetically with the ferromagnet. Because of this interaction, the magnetisation reversal occurs later when sweeping from positive to negative field and earlier when sweeping from negative to positive field. For a closer look at all issues concerning exchange bias see [38, 39]. Please mind the fact, that a model explaining the exchange bias is still lacking. For a very interesting recent investigation see [40, 41].

Chapter 2

Analytical and preparation tools

The analytical tools used in this work are described in this chapter. Not the physical background of every method is explained but the specifications of the used devices. So this chapter is technical but important to understand some limitations of the measurements and sample preparation.

2.1 Transport measurements

Two stations are built up to measure the (magneto) resistance of the prepared samples. One operates at room temperature and one inside a cryostat. Within the scope of this work, MAIK JUSTUS'S phD [42], and my own diploma [43] these stations have been built and programmed.

2.1.1 Room temperature measurements

All room temperature measurements are done with a special device optimised for magnetic tunnel junctions using conventional 2,3 and 4 probe DC technique [42]. It is possible to apply a voltage of maximal $\pm$ 2 V (20 mV, 200 mV) with a resolution of 4096 steps controlled by a PlugIn CIO-DDA06 card in a computer. The current is measured by an electrometer with 6 amplification ranges (max. 100 mA $\dots$ 1 μA). The resolution of the current measurement in the whole equipment is $\sim 0.05\,\%$ of the signal. This leads to a resolution of e.g. $\leq 5\,\mu$A in the 10 mA range. The smallest junctions $(0.1\,\mu\text{m}^2)$ measured in this equipment had a resistance of 200 MΩ and the noise ratio was $\leq 1\,\%$ in the 1 μA range at 100 mV bias voltage [44]. The output of the electrometer is $\pm$10 V and measured by a Keithley K2000 multimeter. The resolution of this instrument is $10\,\mu$V in the used 10 V range, the input resistance is ≥ 10 GΩ [45].

The magnetic field is produced using two coils with a ferrite rod supplied by two BOS/S 36 V - 12 A power supplies with an error of $\pm$ 5 mV [46]. The power supplies are also controlled by the CIO-DDA06 card in the computer. The resolution of this card is 12 bits (full scale) the linearity is $\pm$ 1/2 bit [47]. The maximum magnetic field produced

by this equipment is $\pm$ 3500 Oe. The magnetic field is measured using a Bell 6010 Gauss/ Tesla meter. In the used 3 kG range the resolution is 1 G the accuracy $\pm$ 0.25 % of reading, $\pm$ 3 counts [48].

2.1.2   Cryostat

The low temperature measurements are done with the same transport measurement equipment but the used coils are different. The magnetic field is produced using two coils without a ferrite rod and a maximum field of 2000 Oe is possible. The coils are also supplied by two similar BOS/S power supplies but digitally controlled by Gpib. The resolution of the digital card inside the power supplies is 16 bits. The error of the power supply ($\pm$ 5 mV [46]) and the maximum field of the coils lead to a theoretical resolution of 0.5 Oe. The strength of the magnetic field is determined by current calibration of the coils which are without ferrite rod. The cryostat itself is a closed cycle Helium cryostat with a lowest (highest) temperature of 9.0 K (330 K) [49]. The (empirically determined) temperature stability is better 0.02 K (0.01 K) during the measurements.

2.2   Magnetic characterisation

Two different methods are available to magnetically characterise the layer stacks. The alternating gradient magnetometer (AGM) is a commercial MicroMag 2900 AGM. The magneto optical Kerr effect (MOKE) device was build by JAN SCHMALHORST and DANIELA SUDFELD [50] and within this work improved and programmed.

2.2.1   Magneto Optical Kerr Effect (MOKE)

The setup of the MOKE is straight forward: A red laser (0.5 mW) is polarised ($\leq 10^{-8}$) and after passing the sample a second polariser ($\leq 10^{-8}$) is used as an analyser, and the signal is detected. The signal of the photodiode detector is measured by a Keithley K2000 multimeter (see sec. 2.1.1). The samples are measured using s-polarised longitudinal MOKE with an angle between the filters of 89° [51]. Ferrite rod coils are used to produce the magnetic field. The maximum field is about 3500 Oe @ 2.5 cm air gap and the coils are supplied by a BOS/S 36 V - 12 A power supply (see sec. 2.1.2). The magnetic field is measured using a similar Bell 6010 in the same range as described in section 2.1.1.

2.2.2   Alternating Gradient Magnetometer (AGM)

To determine the absolute magnetisation of the samples, a MicroMag Model 2900 AGM system is used. The electromagnet has a maximum field of 14 kOe @ 12 mm air gap (with furnace equipped 10 kOe @ 20 mm air gap) and an accuracy of 2 % of indication $\pm$1 Oe. The magnetic moment measurement has a range of 1 μemu to 5 emu with an accuracy of 2 % vs. calibration with a pure Nickel standard. It is possible to equip it with a high temperature

furnace with a temperature range of $100\,°C$ to $400\,°C$. The temperature accuracy is $\pm 0.75\,\%$ of set temperature $\pm 2.2\,°C$ [52].

2.3 Auger Electron Spectroscopy (AES)

A Scanning Auger Microscope (SAM) by Physical Electronics, Model 660 was used to get (element specific) depth profile measurements. The spatial resolution of this instrument is about $100\,nm$. The used parameters are showed in table 2.1.

primary energy of the electrons	$10\,keV$
current	$\leq 200\,nA$
diameter of the analysis area	$\sim 70\,\mu m$
sputter gas	Argon
Ar-ion energy	$500\,eV$
rotation speed of the sample	$1/min$
scanning area of the ion beam	$\geq 1.6 \times 1.6\,mm^2$
angle of incidence of the ions	$70\,°$
typical sputter rate	$1\,Å/min$

**Table 2.1:** Used parameters of the Auger microscope for depth profiling

The resolution of this instrument in z-direction is about $1.8\,nm$ determined by measuring a $\{Cu\ 1.74\,nm/\ Ni\text{-}Fe\ 1.51\,nm\}_{20}$ multilayer and calculated via [53].

2.4 Atomic Force Microscope (AFM)

The topography (particularly with regard to the roughness) was measured by a MultiMode Scanning Probe Microscope from Digital Instruments. The maximum scanning area of this microscope is $140 \times 140\,\mu m^2$ with a resolution of $16\,bit \times 16\,bit$. The z-axis resolution is also $16\,bit$ but with a stroke of $5.9\,\mu m$ and a maximum voltage of $440\,V$ at the piezo crystal [54]. To determine the roughness, a few $1 \times 1\,\mu m^2$ areas were scanned and the Root Mean Square (RMS) of the roughness calculated (by the Digital Instruments software).

2.5 X-Ray Diffraction (XRD)

To determine e.g. the texture of the samples a Philips analytical X'Pert Pro MPD X-ray diffractometer with a $2\,kW$ copper cathode is used.
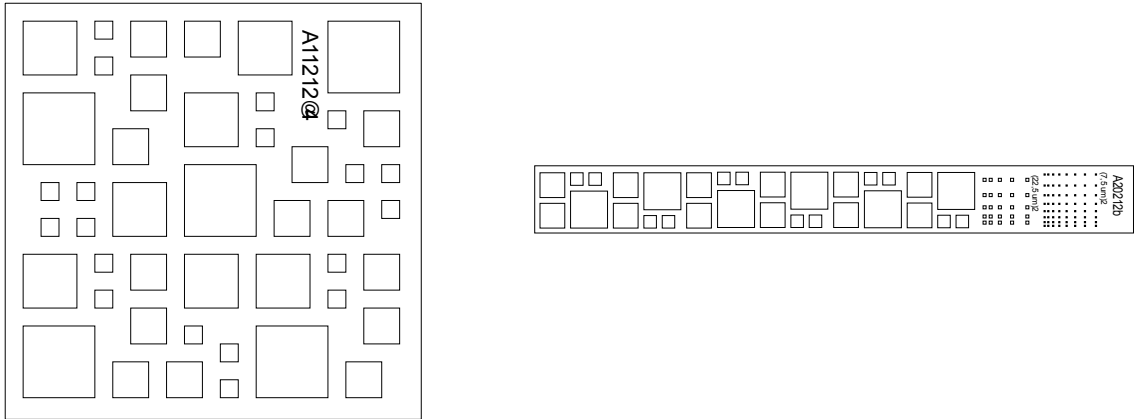
Figure 2.1: The two standard TMR designs with sample name. Left: squared MTJs with sizes of 400, 300, 200, 100 μm length. Right: squared MTJs with sizes of 300, 200, 100, 22.5 and 7.5 μm length. Nearly all MTJs presented in this work use the right design. Please note the different magnifications.

2.6   Optical lithography

The photoresist AR-P 535 by Allresist is used to prepare the samples. The Si-wafer pieces are spin coated for 30 secs at 6000 rounds/min leading to a resist thickness of 800 nm [55]. To expose the samples a Heidelberg Instruments DWL66 optical lithography system with a 4 mm write head is used. It is possible to expose 4" wafers with a resolution of 700 nm. The x-y alignment is done by a stage controlled by 2 laser interferometers. Because AR-P 535 is a special lift off resist, the resolution is decreased to $\lesssim 2\,\mu$m after developing with AR 300-35 developer. Figure 2.1 shows the layout of the prepared structures.

2.7   Ion beam milling

To transfer the structures of the photo resist into the metal layers an ion beam etching machine UniLab (Roth & Rau, Germany) is used. The chamber has a base pressure of 5×10^{-6} mbar and a working Argon pressure of 1.2×10^{-3} mbar. It is possible to rotate the sample holder and the ions hit the sample under an angle of 30°. Additionally, the ion beam is scanned in x and y direction leading to a homogenous etching area of about 30 mm. The Ar-ions are produced by an ion beam source RR-ISQ 40 and a power supply unit MPS-3000 PBN. The discharge voltage is 55 V, the beam voltage is 400 V, and the accelerator voltage is 30 V. The etching process is controlled by integrating the current at the sample to determine the stopping point. Because Copper (besides Gold at the top) is the only metal with a different colour, the etching is checked optically. Figure 2.2 shows an overview of the whole lithography process.
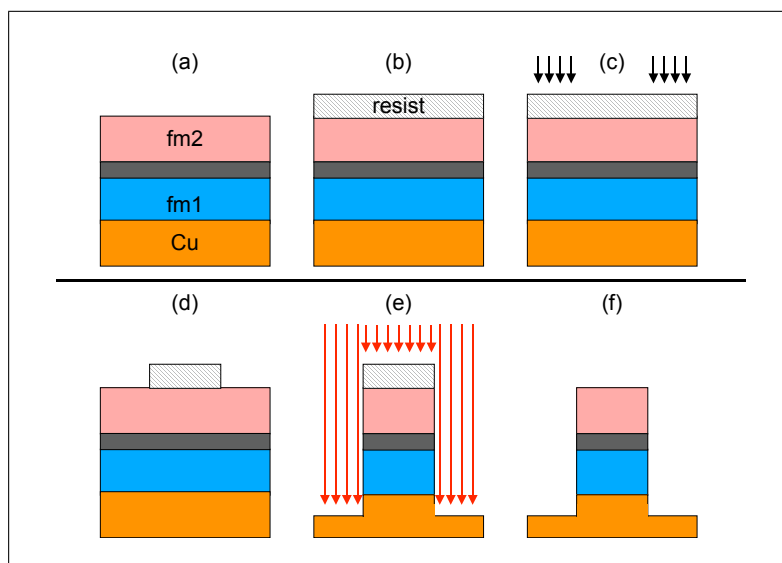
Figure 2.2: Overview of the lithography process. (a) The whole substrate is covered by the sputtered layers. (b) The photoresist is spin coated. (c) The photoresist is exposed by a scanning laser. (d) The exposed area is developed. (e) The uncovered area is etched by ion-beam milling. (f) The resist is removed and the TMR stack remains.

2.8 Vacuum furnace

Within this and JAN SCHMALHORST'S work a vacuum furnace has been built and programmed. The base pressure is 2×10^{-8} mbar and it is possible to anneal two 2 inch wafers at a maximum temperature of $550\,^{\circ}\text{C}$. Two different permanent magnets (1000 Oe/ 6500 Oe) are available to allow field cooling of the samples. Figure 2.3 shows the typical temperature course of a sample with a target temperature of 1h @ 250 °C. The annealing always starts at a pressure of 1×10^{-7} mbar.
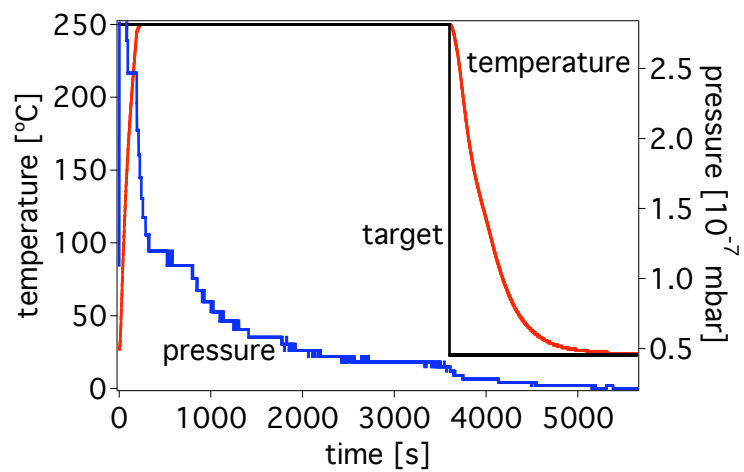
Figure 2.3: Typical temperature profile of the vacuum furnace (red line). Target is $1\mathrm{h}\,@\,250\,^\circ\mathrm{C}$ (black line). The pressure is additionally plotted (blue line).

Chapter 3

Single barrier junctions

All the samples are prepared in a "Leybold CLAB600 Clustertool" sputter system. It consists of six 4" magnetron sputter sources, an oxidation chamber and a handler system with a 8 place load lock for 4" wafers. Within the scope of this work the sputter system was put into operation, extended by a second oxidation chamber and a 7th sputter source (2"), the SPS control was reprogrammed and different computer programs were developed to fulfil the conditions to prepare magnetic tunnel junctions.

3.1   Preparation and experimental details

The layer stack of the standard TMR sample (system 5 with anti-ferromagnet, AF5) consists of Cu (30nm)/ Py (4 nm)/ Mn-Ir (15nm)/ Co-Fe (3nm)/ Al (1.4 nm)+Ox/ Py (4 nm)/ Ta (3nm)/ Cu (55nm)/ Au (20nm) on top of a thermally oxidized ($t_{ox} = 100\,nm$) silicon (100) wafer. The low electric resistance of less than $1\,\Omega$ of the first layer in the patterned tunnel junction avoids geometrical artefacts in 4 terminal DC measurements [33] discussed in section 1.4. Permalloy ($Ni_{80}Fe_{20}$ = Py) is used as a seed layer [56] for the antiferromagnetic $Ir_{17}Mn_{83}$ which exchange biases the lower $Co_{70}Fe_{30}$ electrode. A pinned bottom electrode is used instead of a pinned top electrode to maximise the exchange field [57, 58, 59]. The composition of the lower electrode is chosen due to the high TMR values reported in ref. [60]. The composition of the Iridium-Manganese leads to a high Neel- and blocking temperature [57, 39, 61]. Mn-Ir itself is used because of high values of the exchange field [62, 63, 64] and easy handling [65]. The layer thicknesses are optimised with respect to the magnetic properties discussed in section 3.2.

The Aluminium layer is oxidised with pure oxygen using a 2.46 GHz remote ECR plasma source RR 160 PQE from Roth und Rau GmbH. This method allows the adjustment of five independent parameters in the oxidation process: oxygen pressure (fixed at $2 \times 10^{-3}\,mbar$), oxygen flow (fixed at $13\,sccm$), plasma input power (fixed at $275\,W$), oxidation time and DC bias at the sample which was additionally installed. The oxidation time and bias voltage are systematically varied in order to evaluate the influence of the ion energy on the barrier formation. This will be discussed in section 3.3.
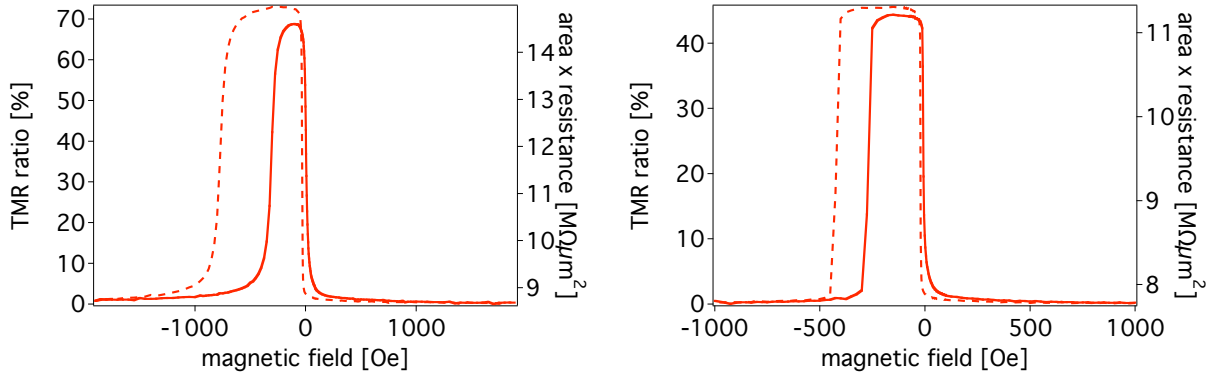
Figure 3.1: Major loop of an optimised Mn-Ir15(nm)/ Co-Fe6/ AlO$_x$ 1.8/ Py4 tunnel junction at 10 K (left) and at room temperature (right) after annealing (2' @ 250 °C). Please note the different x-axis.

The stacks are patterned by optical lithography and ion beam etching yielding squared MTJs with sizes of 300, 200, 100, 22.5 and 7.5 μm length. The properties of the junctions reported here are independent of the junction size. To activate the exchange biasing, the layer stack is annealed after sputtering at 250 °C for 2 minutes in a magnetic field of 1000 Oe. The dependence of the biasing on the annealing temperature is discussed in section 3.4. Figure 3.1 shows the typical major loop of an optimised MTJ (AF5) at 10 K and room temperature.

3.1.1   Structural properties

Figure 3.2 shows a X-Ray Diffractometer (XRD) measurement of the layer stack AF5 without the upper Copper and Gold layers, because their structural properties do not influence the TMR stack. The micro-structure of 2 layers and the Silicon substrate can be seen: the Copper layer and the Iridium-Manganese. All other layers are too thin and their signal is below the noise limit.

Four peaks corresponding to the Silicon (100) wafer are visible [66, 67, 68]. There are two Si (400) peaks, because the signal is so high that the parasetical Cu-K-β Si (400) peak is visible. The structure of the substrate has no influence on the stack growth on top of thermally grown, amorphous Silicon oxide (50/ 100 nm). The intensity of the Copper peaks, if compared with reference spectra of polycristalline Copper reveals a weak (111) texture. The relative intensity of the Cu (111) peak is 2.5 times higher than in polycrystalline material [69].

The Mn-Ir is deposited by rf magnetron sputtering to get a better (111)-texture and larger crytallites [70], all other materials are sputtered by dc magnetron sputtering. It is difficult to interpret the spectrum of the Iridium-Manganese. Although the used alloy
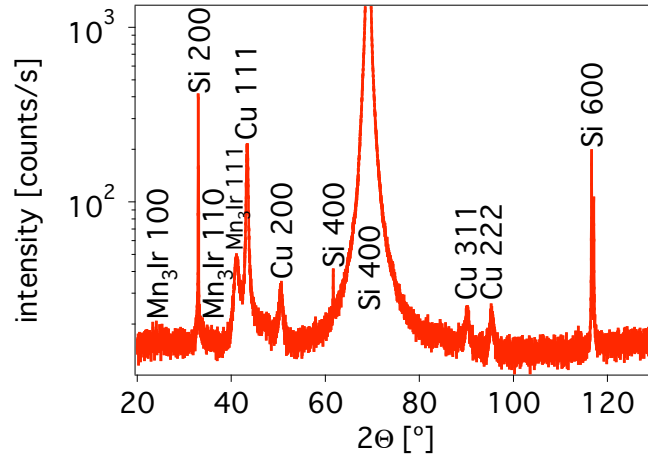
Figure 3.2: XRD measurement (Cu-K-α line = 1.54 Å) of the layer stack Cu30 (nm)/ Py4/ Mn-Ir15/ Co-Fe3/ Al1.4 + ox./ Py4/ Ta3. Within the resolution of the instrument only the thick Copper and Mn-Ir layers and the Silicon wafer can be seen.

is different ($Mn_{83}Ir_{17}$) from the reference polycrystalline Mn_3Ir, there are no major differences if the alloy has the same crystalline structure. But Auger measurements of the deposited Mn-Ir and comparison with a known $Mn_{84}Ir_{16}$ alloy (determined by x-ray fluorescence analysis) resulted in a ratio of $Mn_{88}Ir_{12}$ corresponding to the (γ-Mn)-phase [71]. No reference spectra of the (γ-Mn)-phase were found. If compared to the also cubic Mn_3Ir, the Iridium-Manganese layer might be strongly (111) textured, only the Mn-Ir (111) peak is visible. In polycrystalline material [72] the Iridium-Manganese (100)/ (110) peaks show an intensity of 0.68/ 0.45 of the Mn-Ir (111) peak. Note that (111) texture of the Mn-Ir was intended to get strong exchange coupling. The texture of the ferromagnetic electrode could not be determined, although the texture of the top and bottom electrode directly affect the TMR effect [73].

To determine the roughness of the interfaces between the layers in the TMR stack and especially the roughness at both sides of the tunnel barrier, atomic force microscope (AFM) measurements are done. The stack was always sputtered up to the designated layer and then measured with the AFM. Because the vacuum is broken it is not possible to exclude oxidation of the investigated layers, but all measurements were done immediately after preparation.

Table 3.1 shows the results of these investigations. Already after the first Copper layer the roughness increases to 4.1 Å, but the Iridium-Manganese flattens the stack (2.8 Å). This behaviour is also observed in very similar TMR stacks [74]. The deposited Cobalt-Iron increases the roughness again to 3.5 Å at one side of the barrier. At the other side it is nearly the same value (3.6 Å) after oxidation. The value on top of the upper Permalloy

roughness	SiO$_x$	Cu	Py	Mn-Ir	Co-Fe	AlO$_x$	Py
RMS [Å]	2,6	4.1	3.9	2.8	3.5	3.6	5.6
error [Å]	≤0.1	0.1	0.4	0.4	0.1	0.1	0.5

Table 3.1: Roughness measurements (RMS) of the TMR stack (Cu30 (nm)/ Py4/ Mn-Ir15/ Co-Fe3/ Al1.4 + ox./ Py4) on top of every layer and standard error.
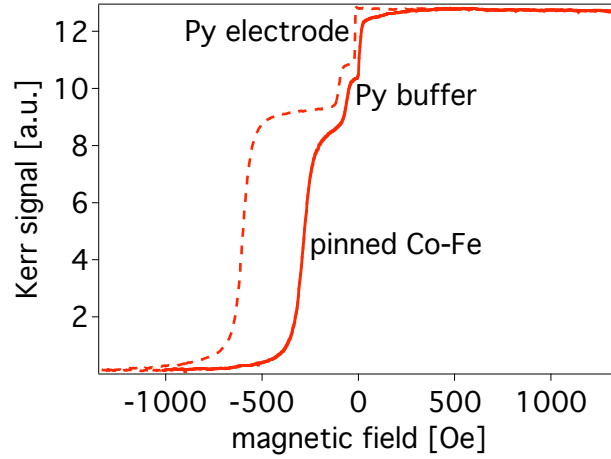
Figure 3.3: MOKE measurement of Cu30 (nm)/ Py4/ Mn-Ir15/ Co-Fe3/ Al1.4 + ox./ Py4/ Ta3 annealed at 250 °C for 2 minutes in a magnetic field of 1000 Oe.

electrode becomes important only in double barrier junctions (chap. 4). The influence of these roughnesses on the magnetic properties of the junctions is discussed in section 3.2.

3.2   Unidirectional anisotropy and magnetic properties

The properties and especially the unidirectional anisotropy of the layer stack Cu30 (nm)/ Py4/ Mn-Ir15/ Co-Fe3/ Al1.4 + ox./ Py4/ Ta3 are investigated to tailor the magnetic properties and finally to get an optimised TMR system. All sample are annealed 2' @ 250 °C in a magnetic field of 1000 Oe to obtain the exchange bias and the maximum TMR ratio. It is important to investigate only TMR systems with high TMR ratio, because in junction with very low TMR ratios misinterpretations due to spurious effects are highly likely. The dependence of transport and magnetic properties on annealing temperature is discussed in detail in section 3.4.

The magnetic properties are measured by the Magneto Optical Kerr Effekt (MOKE).
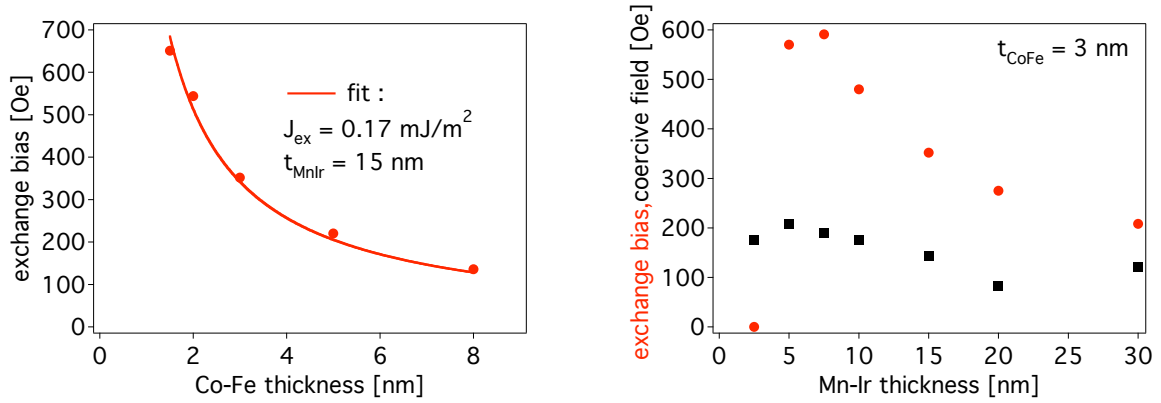
Figure 3.4: Left: The exchange bias of the Co-Fe layer in dependence on its thickness. The solid line corresponds to a theoretical fit described in the text. Right: Exchange bias and coercive field of the Co-Fe layer in dependence on the Mn-Ir thickness. All samples after annealing (2' @ 250 °C). Coercive field black, layer stack (Cu30 (nm)/ Py4/ Mn-Ir15 (varied)/ Co-Fe3 (varied)/ Al1.4 + ox./ Py4/ Ta3).

Figure 3.3 shows a typical magnetisation curve of the standard sample AF5. Pinning and coercive field of the 3 magnetic layers are determined by fitting (using the Marquart-Levenberg fit [20]) the minor loops with the commonly used function representing a ferromagnetic hysteresis loop [75]:

$$M(H) = \frac{2M_s}{\pi} \tan^{-1}\left[\frac{(H - H_p \pm H_c)}{H_c} \tan\left(\frac{\pi S}{2}\right)\right]$$

M_s is the saturation magnetisation of the ferromagnet, S is the squareness of the hysteresis loop, H_c is the coercive and H_p the pinning field (the horizontal shift of the hysteresis loop). Due to the complete separation of the two magnetic electrodes the anti-parallel state in MTJs can be obtained.

Figure 3.4 (left) shows the dependence of the exchange bias field on the thickness of the Cobalt-Iron layer. By fitting the theoretical expression $J_{ex} = H_{ex}\mu_0 M_{CoFe} t_{CoFe}$ [38] the surface coupling energy J_{ex} is determined, H_{ex} is the pinning field, $M_{CoFe} = 1.65 \times 10^6$ A/m [76] is the magnetisation of saturated Co-Fe and t_{CoFe} its thickness. This leads to a value of $J_{ex} = 0.17$ mJ/m^2 (15 nm Mn-Ir), which is only roughly half the value reported for bottom spin valve type systems with Mn-Ir and Co-Fe [59, 63], due to the not optimised annealing temperature and Mn-Ir thickness.

The dependence of the exchange bias and coercive field on the Iridium-Manganese thickness shows figure 3.4 (right). A steep increase of the exchange bias between 2.5 and 5.0 nm is followed by a flat decrease above 7.5 nm Mn-Ir thickness. This behaviour is typical for thin Mn-Ir films [57, 38, 77]. This might be due to a change of the (111)
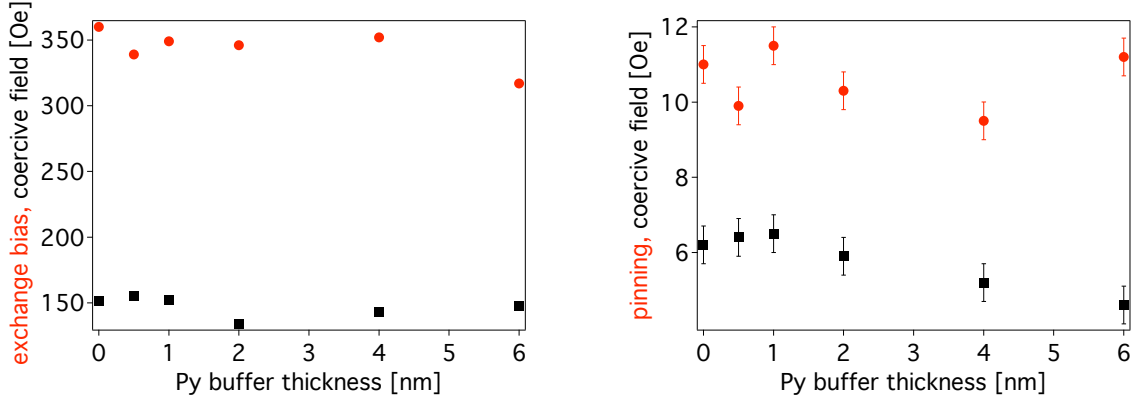
Figure 3.5: The exchange bias and coercive field of the Co-Fe layer (left) and the pinning and coercive field of the upper Py (right) in dependence on the Py buffer layer after annealing (2' @ 250 °C). Coercive fields black, layer stack (Cu30 (nm)/ Py x/ Mn-Ir15/ Co-Fe3/ Al1.4 + ox./ Py4/ Ta3).

orientation for the Mn-Ir films thicker than 7.5 nm [57, 58, 77] although these changes could not be determined. If again the maximum surface coupling energy is calculated it equals $J_{ex} = 0.27 \, mJ/m^2$ @ 7.5 nm Mn-Ir, which is close to the maximum value reported [59, 63].

The coercive field of the Cobalt-Iron layer has its maximum at 5 nm Mn-Ir thickness and slowly decreases afterwards corresponding to the exchange bias. The behaviour is also typical [59, 38, 78]. The Co-Fe interacts with thin Iridium-Manganese film which has a weak crystalline anisotropy and pulls the Mn-Ir spins during the magnetisation reversal, because the condition $K_{afm}t_{afm} >> J_{ex}$ is violated, with $K_{afm}t_{afm}$ as the product of anisotropy and thickness of the anti-ferromagnet [38].

All interpretations concerning the pinning field and the coercivity of the Co-Fe electrode are most likely from today's point of view. But (as mentioned earlier) a model describing all details of exchange bias is still lacking. Even the simple question, how compensated surfaces can result in exchange bias is not answered. Therefore, other effects such as dependence of blocking temperature or domain structure on thickness might play a significant role.

Figure 3.5 shows the dependence of the exchange bias/ pinning and coercive field of the two electrodes on the thickness of the bottom Permalloy layer. As mentioned in section 3.1 the Py is used as a seed layer for the Iridium-Manganese in early experiments [56]. But figure 3.5 clearly shows that this is not necessary. Neither the exchange bias or the coercive field of the Cobalt-Iron nor the pinning (the origin of this pinning field is discussed in section 3.2.2) or coercive field of the top Py electrode show any systematic and significant dependence on the buffer thickness. Even, if there is no Permalloy buffer at all, the properties of the magnetic layers are the same. This allows the preparation of different top electrodes in the six source magnetron sputter system.

In summary, the magnetic properties of the exchange biased layer stack Cu30 (nm)/

values in %	Fe	Ni	Co	$Ni_{80}Fe_{20}$	$Co_{50}Fe_{50}$	$Co_{70}Fe_{30}$	$Co_{84}Fe_{16}$
RT	33	19	36	43 (44)	44	43 (45)	–
10 K	43	28	38	53	48	50	–
[80]	44	33	45	48	51	–	49

Table 3.2: Effective spin polarisation of different ferromagnetic electrodes at 10 mV bias voltage at room temperature (RT) and 10 K and comparison with literature. Highest values at RT without corresponding 10 K measurements in brackets. Layer stack (Cu30 (nm)/ Mn-Ir15/ Co-Fe3/ Al1.4 + ox./ X4/ Ta3/ Cu55/ Au20).

Py4/ Mn-Ir15/ Co-Fe3/ Al1.4 + ox./ Py4/ Ta3 (AF5) were investigated. It is possible to tailor the magnetic properties to fulfil the needs of a TMR system and to completely separate the two magnetic electrodes, which is the main requirement to get a high TMR ratio ($46.3 \pm 0.2\%$). The maximum surface coupling energy of the exchange bias was in accordance with literature [59, 63] $J_{ex} = 0.27\,mJ/m^2$. This value can be further increased by using higher annealing temperatures. This is discussed in section 3.4. The results of this section are published in [79].

3.2.1 Spin polarisation of different ferromagnetic electrodes

The spin polarisation of different ferromagnets are determined by using different top electrodes. First, two $Co_{70}Fe_{30}$ electrodes are used to calculate the spin polarisation of $Co_{70}Fe_{30}$ as a reference value for all other materials, because the lower electrode always remains the same. Then, with the assumption of equal spin polarisation of the two Co-Fe electrodes all other values can be calculated using the polarisation of the Cobalt-Iron. Equation 1.5 leads to

$$P^2_{CoFe} = \frac{TMR}{2 + TMR} \qquad P_X = \frac{TMR}{TMR P_{CoFe} + 2 P_{CoFe}} \qquad (3.1)$$

Table 3.2 shows the values for all tested materials and the comparison with literature [80]. All values are related to Aluminium oxide barriers.

It is very difficult to find newer values for materials apart from Co-Fe and Ni-Fe alloys, because these materials show the highest TMR ratios. Therefore, these materials are the most interesting in view of applications and devices. The highest spin polarisation for these kind of junctions is reported by TSUNODA: 48 % (58.8 % TMR ratio) at room temperature in $Co_{70}Fe_{30}$/ Al-O/ $Co_{70}Fe_{30}$ tunnel junctions [81]. These junctions are prepared using a special oxidation technique ($Kr - O_2$ mixture) resulting in very low trap densities and uniform oxidation depth as known from the use in semiconductor gate-oxides.

When investigating table 3.2, one would prefer Ni-Fe/ Al_2O_3/ Ni-Fe junctions for tunnel elements, because Permalloy (Ni-Fe) shows the highest spin-polarisation value. But the prepared junctions exhibit only a TMR ratio of roughly 30 % at room temperature. The explanation for this behaviour is most likely the changed texture of the Permalloy on top

of the Mn-Ir [73]. Very recent results show that the introduction of a Gd seed layer leads to very high TMR ratios [82].

It is very difficult to put the obtained values on a solid physical base. The so-called effective spin-polarisation in magnetic tunnel junctions can not be calculated (so far). It is not even possible (as mentioned earlier) to explain its sign. When taking electron scattering induced magnon excitations into account, it is questionable if the TMR directly probes the intrinsic spin-polarisation at all. Surprisingly, all ferromagnetic materials show an effective spin-polarisation of roughly 50 %, when using TMR experiments (and the Julliere model) or spin-polarised tunnelling in a superconductor (all in relation to Aluminium-oxide barriers). This includes the 3d-ferromagnets, their alloys and even an (half-metallic) Heusler alloy (cf. table 3.2 and [83, 84])!

3.2.2 Orange peel coupling

To understand the shift of the magnetisation curve of the upper Permalloy electrode in AF5, the so called orange peel coupling (or Neel coupling) is investigated with the approach of KOOLS [85]. The original Neel model [86] explains the magnetostatic interaction between two ferromagnetic films of infinite thickness. One layer is free and one pinned and they are separated by a nonmagnetic spacer.

A more exact analysis of ZHANG [87] takes into account the finite thickness of the ferromagnetic layers because the magnetic poles created at the outer interfaces of the magnetic layers lead to additional interactions. This is further investigated by KOOLS. Here we consider only the case of columnar structures with conformable waviness.

Equation 3.2 shows the dependence of the pinning field H_P on the properties of the pinned and the free layer:

$$H_P = \frac{\pi^2 h^2 M_P}{\sqrt{2}\lambda t_F} \left[1 - \exp(-2\pi\sqrt{2}t_F/\lambda) \right] \times \left[1 - \exp(-2\pi\sqrt{2}t_P/\lambda) \right] \exp(-2\pi\sqrt{2}t_S/\lambda) \quad (3.2)$$

M_P (M_F) is the saturation magnetisation of the pinned (free) layer, t its thickness, λ the wave length, and h the amplitude of the sinusoidal interface roughness. It is easy to see the effect of the 3 different contributions: The two (1-exp) terms increase with increasing thickness of the pinned and free layer. The thicker the magnetic layers are, the higher is the Neel coupling. The last exp term decreases with increasing thickness of the spacer layer.

To find out the interface waviness (i.e. λ and h), atomic force microscope (AFM) pictures are used. Figure 3.7 shows 30 nm Copper on top of a thermally oxidised (100 nm) Si-wafer. The amplitude h is proportional to the RMS value directly determined by the microscope software. To find out the grain size (i.e. the waviness), the picture is edited by low and high pass filters and the number of grains are counted in different line scans.

For equation 3.2 the parameters of the Co-Fe and the Aluminum-oxide surface are needed. The Cobalt-Iron has a grain size of 24.3 ± 3.0 nm and a RMS value of 3.5 ± 0.1 Å, the Aluminium oxide layer shows values of 21.4 ± 1.6 nm grain size and 3.6 ± 0.1 Å RMS.
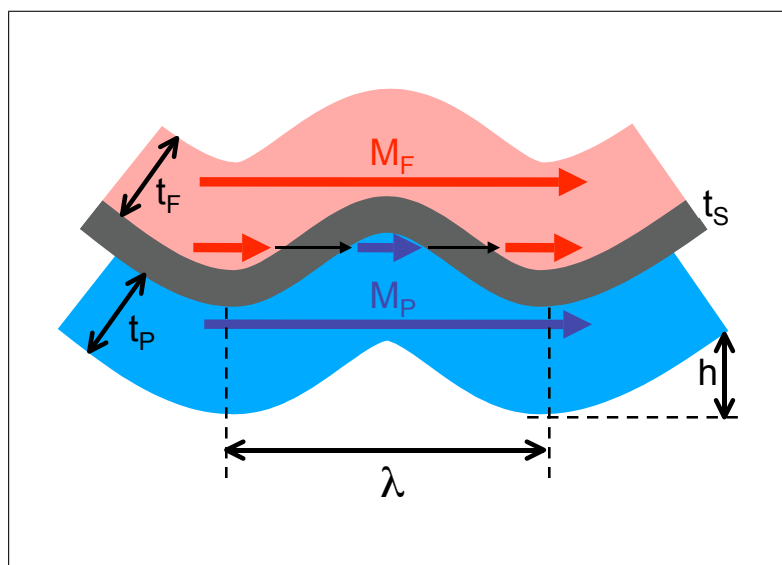
Figure 3.6: Scheme of the magnetostatic interaction in the case of columnar structure with conformable waviness, introducing all values used in the calculation. Magnetic free layer red, spacer grey and pinned layer blue.
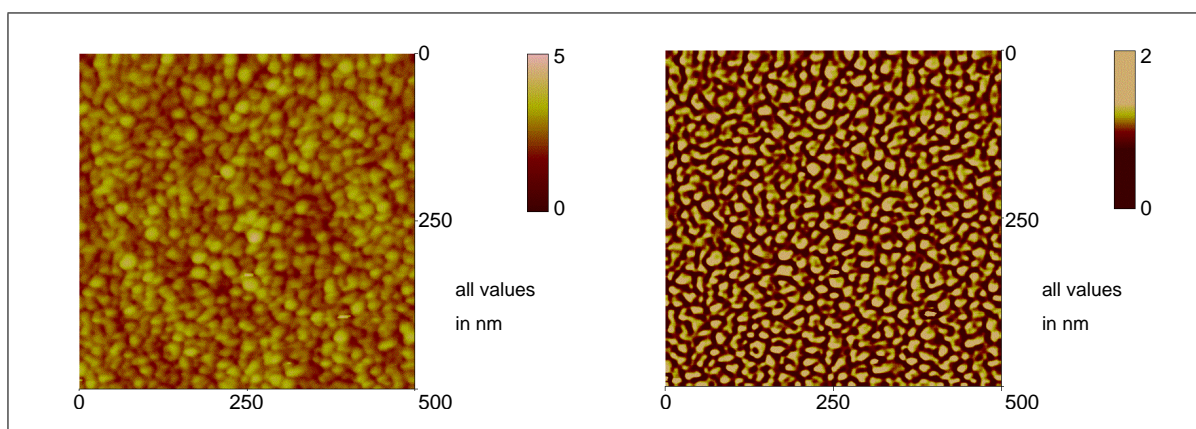
Figure 3.7: AFM measurement of $30\,\text{nm}$ Copper on top of a thermally oxidised ($100\,\text{nm}$) Si-wafer. Raw picture (left) and edited (right) to visualise the grains.
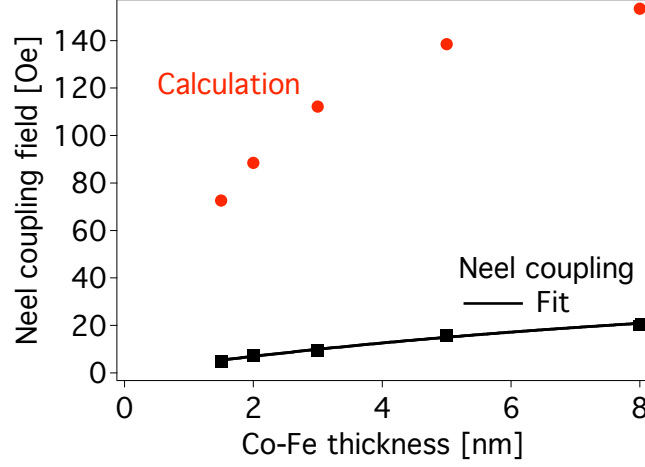
Figure 3.8: Measurement and calculation of the Neel (orange peel) coupling of the Py top electrode in dependence on the thickness of the Co-Fe electrode. The solid line corresponds to a theoretical fit described in the text. Layer stack (Cu30 (nm)/ Py4/ Mn-Ir15/ Co-Fe x/ Al1.4 + ox./ Py4/ Ta3).

First, this does not contradict the premise of conformable waviness, because these values are equal within the error.

Figure 3.8 shows the calculation of the orange peel coupling based on equation 3.2 and the experimental values determined by MOKE. The calculated values are much larger than the experimental ones, but if using any reasonable values for a TMR layer stack (RMS ≥ 0.2 nm, $t_P = t_F = 3$ nm, $t_S = 2$ nm, $M_{CoFe} = 1.65 \times 10^6$ A/m [76], $\lambda \leq 30$ nm), the calculated values are always higher than the experimental ones.

Thus, the model of KOOLS is extended with regard to the correlation of the roughness of the two ferromagnetic electrodes. To take into account, that the correlation is not perfect, the factor ξ is introduced. Indeed, experiments indicate, that the tunnel barrier in magnetic tunnel junctions does not completely image the underlying layer [88, 89]. Therefore, the correlation can not be perfect. An effective waviness $\xi\lambda$ is used and leads to:

$$H_P = \frac{\pi^2 h^2 M_P}{\sqrt{2}\xi\lambda t_F} \left[1 - \exp(-2\pi\sqrt{2}t_F/\xi\lambda)\right] \times \left[1 - \exp(-2\pi\sqrt{2}t_P/\xi\lambda)\right] \exp(-2\pi\sqrt{2}t_S/\xi\lambda)$$

The parameter $\xi = 3.5$ was determined by a fit and a very good correlation between the calculated value and the fit is obtained (cf. fig. 3.8). The value of 3.5 seems reasonable, but free parameters always increase the quality of a fitting procedure, sometimes without physical meaning. But in this case, the parameter ξ changes the slope of the fitting curve and a systematic discrepancy would be clearly visible. Further investigations have to show whether the extension of the model using this correlation factor is always reasonable.

3.3 Tunnel barrier formation by ECR plasma oxidation

The formation of the tunnel barrier is a challenging preparation step for the MTJs [80]. The simplest approach is direct Al_2O_3 sputtering [90], but better results are yielded by postoxidation of thin Aluminium films. A lot of different oxidation techniques have been developed, e.g. plasma [91], thermal [92], ultra violet light assisted [93] and natural oxidation [94]. The MTJs prepared by different oxidation methods show different barrier properties and TMR effects. For instance, natural and UV assisted oxidation is better for low resistance MTJs in read heads, whereas plasma oxidation is favoured for medium resistance memory cells in MRAM devices [95]. However, aggressive plasma methods do not allow the control of the oxidation depth in very thin Aluminium-oxide barriers.

Here a novel and flexible oxidation method is used: A remote electron cyclotron resonance (ECR) plasma. The bias voltage applied to the sample can be chosen independently in this technique in order to adjust the kinetic energy of the oxygen ions impinging on the Aluminium film. This is in contrast to the commonly used floating substrate during plasma oxidation and gives another free parameter. The method is discussed with regard to area resistance, TMR amplitude and the barrier properties.

The described tunnel stack (Cu30 (nm)/ Py4/ Mn-Ir15/ Co-Fe3/ Al1.4 + ox./ Py4/ Ta3/ Cu55/ Au20) is oxidised by varying the substrate bias voltage ($-3.3\,V$, $-10\,V$, $-30\,V$, $-70\,V$) and the oxidation time ($10\,s$ to $300\,s$). Oxygen pressure ($2 \times 10^{-3}\,mbar$), oxygen flow ($13\,sccm$) and plasma input power ($275\,W$) are held constant at appropriate values. The change in the properties is evaluated by inspecting TMR ratio and area resistance (R_A) (fig. 3.9) and compared to the change of the barrier properties like barrier height and effective thickness evaluated from current/voltage characteristics. The measured current during oxidation is not sufficient to account for the observed oxidation rates [96].

A clear tendency of R_A with increasing substrate bias is found (fig. 3.9). Whereas bias voltages (V_B) of $-3.3\,V$ and $-10\,V$ give almost the same (R_A), further increase of V_B also increases the area resistance. The resistance changes 4 orders of magnitude from $500\ k\Omega\mu m^2$ ($10\,s$ at $-10\,V$) up to nearly $10\,G\Omega\mu m^2$ ($130\,s$ at $-70\,V$). The highest TMR ratios are observed at $-10\,V$ and $100\,s$ or $-3.3\,V$ and 150-$200\,s$. The behaviour is typical: A steep increase of the TMR ratio is followed by a flat decrease [93]. The samples with substrate bias of $-70\,V$ do not follow this behaviour.

In order to get a better insight in the physical mechanism of the described behaviour, we evaluate the barrier parameters (height and effective thickness) from current-voltage characteristics. This is done by fitting the experimental results to the formula of BRINKMAN et al. [16] (discussed in section 1.2) with an effective electron mass of $0.4\,m_e$ [97]. The absolute values of the barrier characteristics obtained by applying this relatively simple model may not be very precise. Nevertheless, the trends for different oxidation parameters turn out to provide a physically consistent picture, which explains the variation of the TMR and the resistance of the MTJs.

Figure 3.10 shows fit parameters of the same MTJs investigated in figure 3.9. Pro-
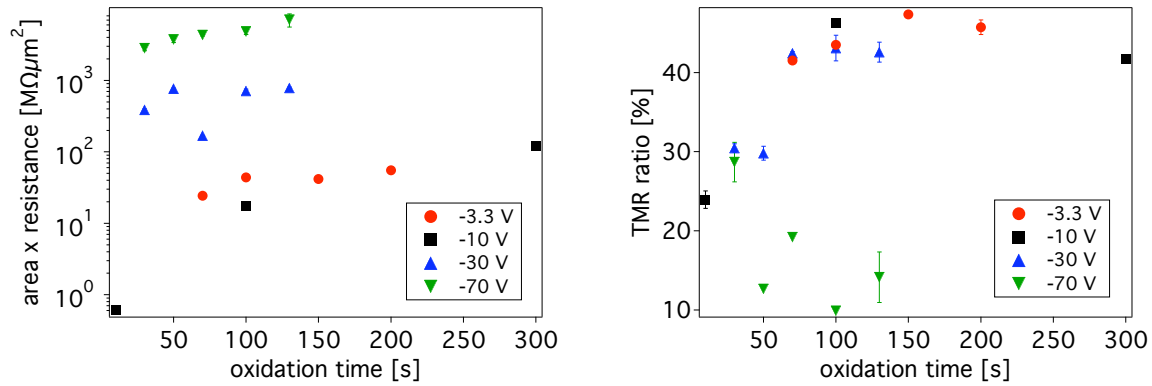
Figure 3.9: Area resistance and TMR ratio at room temperature in dependence of the oxidation time at different substrate bias voltages during oxidation. Layer stack (Cu30 (nm)/ Py 4/ Mn-Ir15/ Co-Fe3/ Al1.4 + ox./ Py4/ Ta3/ Cu55/ Au20).
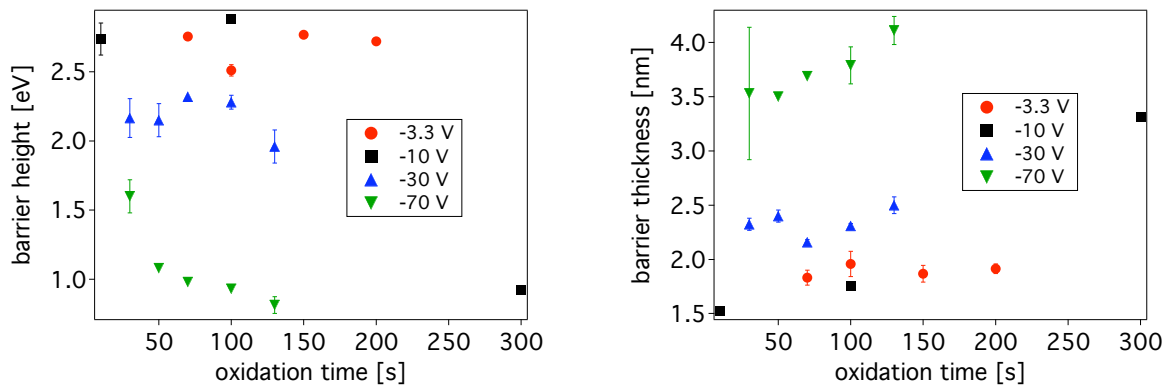
Figure 3.10: Barrier height and thickness (via BRINKMAN'S formula at room temperature in the parallel state [16]) in dependence of the oxidation time at different bias voltages. Layer stack (Cu30 (nm)/ Py4/ Mn-Ir15/ Co-Fe3/ Al1.4 + ox./ Py4/ Ta3/ Cu55/ Au20).

vided only all of the Aluminium is oxidised, the barrier thickness should be 1.8-2.0 nm. This is obtained only for the bias voltage of -3.3 V and -10 V and times between 50 s and 200 s. The junctions prepared at these substrate voltages additionally show a barrier height of about 2.8 eV corresponding to the highest values reported using different oxidation techniques [81]. Thus, we conclude that these parameters are at optimum for obtaining completely oxidised barriers. This is in agreement with the large TMR values found at these MTJs. For a lower oxidation time at these bias voltages the TMR and the barrier thickness is smaller than in the optimum state pointing to a slight underoxidation and remaining Aluminium at the interface, which leads to a strong suppression of spin dependent tunnelling.

MTJs prepared with these optimum oxidation parameters but Co-Fe at both barrier sides show a TMR ratio of 71 % at 10 K, leading to a spin polarisation of 51 % using JULLIERE'S formula [1]. This corresponds well to the experimental data (50 %-52 %) for $Co_{60}Fe_{40}$, $Co_{50}Fe_{50}$ and $Co_{84}Fe_{16}$ at 4.2 K measured by PARKIN [98].

Although the samples prepared with -30 V substrate voltage also show high TMR ratios of more than 42 %, damage can be concluded from the lower barrier height and the larger barrier thickness of 2.2 nm-2.5 nm. The large R_A values are additional indicators for overoxidation. Thus, at these parameters the underlying Co-Fe film is also oxidized, resulting in a slightly decreased TMR ratio (fig. 3.9) and a strongly increased barrier resistance.

The barriers of the samples oxidized with a bias voltage of -70 V show extremely thick barriers (3.5 nm-4.1 nm) and an unphysically low barrier height (1.6 eV-0.8 eV) already at short oxidation times. Damaging of the Aluminium film and the Co-Fe electrode by bombardment effects of high energetic ions can be concluded in agreement with a penetration depth of more than 1.8 nm at this energy [99]. Note, that this leads effectively to a double step barrier, which is not described by BRINKMAN'S model.

In summary, a reproducible fabrication technique for the tunnel barrier in magnetic tunnel junctions was demonstrated using an ECR plasma oxidation and an additional DC substrate bias, enabling the control of the energy of the ions bombarding the Aluminium film. An ion energy between 3.3 eV and 10 eV leads to a high TMR ratio of 73 % at 10 K and a barrier height of 2.8 eV, i.e. at these energies an optimum oxidation of the Aluminium film is obtained without oxidising the underlying electrode. By varying the oxidation time, the resistance can be tailored maintaining the high TMR ratio. At larger energy, the results give evidence for an overoxidation, i.e. the barrier becomes thicker and the apparent height is reduced. This is accompanied by an extremely large area resistance and strongly reduced TMR ratios. These results are published in [100] and further investigated in [101].

3.4 Annealing temperature dependence

Besides the signal to noise ratio (cf. sec 3.6), the stability of MTJs in dependence on temperature, bias voltage or magnetic stray fields is most interesting from the application point of view [19]. This section focusses on the annealing temperature dependence. Inves-
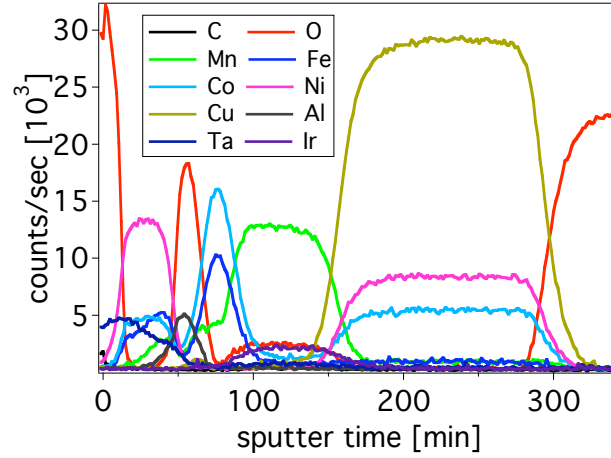
Figure 3.11: Raw Auger depth profile of a magnetic tunnel junction without top conducting layers after annealing for 1 hour at 400°C. Layer stack: SiO$_x$/ Cu30(nm)/ Mn-Ir15/ Co-Fe3/ Al1.4/ Py4/ Ta5.

tigation of many different groups show that the temperature stability of magnetic tunnel junctions is not an intrinsic parameter, but depends on the layer system. In most cases the tunnel barrier remains intact, there still is a tunnelling current even after annealing at higher temperatures. But diffusion processes affect the electrodes and destroy the spin polarisation and therefore the TMR effect [19].

Though the fundamental processes governing the loss of TMR due to diffusion (even in the used layer stack) is well understood (e.g. [60, 102, 91]). Therefore, it is expected to find Mn and Cu diffusion towards the barrier, finally destroying the TMR effect. But the details of these processes as they relate to the specific samples discussed in this thesis are of importance to establish reliable, reproducible magnetic tunnel junctions. The following section is included to explore these specifies.

3.4.1 Diffusion processes

Figure 3.11 shows the Auger depth profile of a MTJ without the conducting top layers Gold and Copper. It is a raw profile, no target factor analysis is made. For detailed analysis, the data has to be processed first. All measurement artefacts have to be addressed, such as the asymmetric Ta peak (caused by the lower sputter rate of Ta in the Ta-Py mixture caused by ion bombardment [19]) and the earlier increase of the Aluminium compared to the Oxygen (caused by the higher kinetic energy and therefore the decay length in the Py layer [103]). Thereafter, two main diffusion processes can be found in the investigated magnetic tunnel junctions: as expected, Copper (400°C) and Manganese (275°C) below the bottom electrode diffuse towards the tunnel barrier and accumulate there.
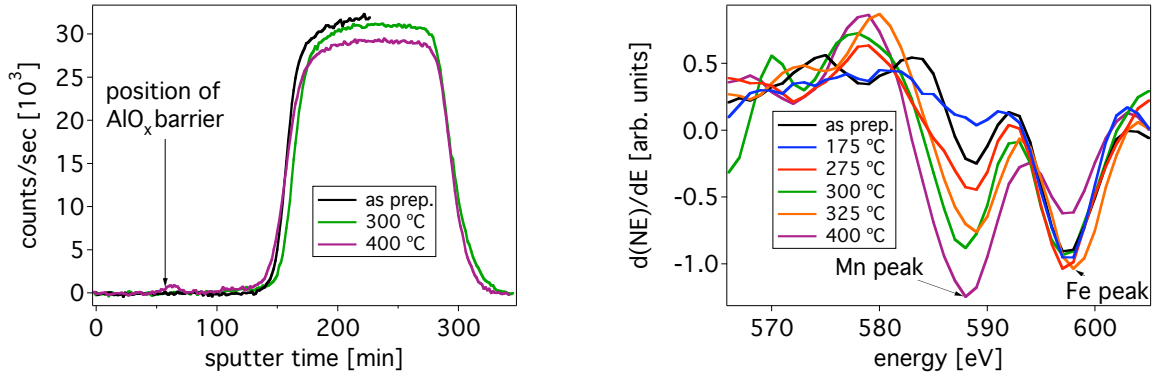
Figure 3.12: Depth profile analysis for different annealing temperatures (1 hour annealing time). Copper and Manganese diffuse towards the tunnel barrier. Left: The Copper signal of the Auger depth profile. Right: The Manganese and Iron signal at the barrier interface. Layer stack: SiO_x/ Cu30(nm)/ Mn-Ir15/ Co-Fe3/ Al1.4/ Py4/ Ta5 (+Cu55/ Au20).

Figure 3.12 shows this in two different ways to make the changes more obvious. The Copper diffusion is discussed first. The left part of figure 3.12 shows only the Copper signal of raw depth profiles like figure 3.11 for different annealing temperatures. Additionally, the position of the tunnel barrier is marked. It is taken as the maximum of the Oxygen peak in the profile. The accumulation of Copper at the barrier at 400°C annealing temperature is clearly visible.

The second diffusion process is the accumulation of Manganese at the barrier. This is easier to see directly in the peak shape between 570 and 605 eV (cf. fig. 3.12). Although, there is some noise in the signal, the Manganese signal increases with increasing the annealing temperature. All curves are also taken at the 'position' of the tunnel barrier, where the Oxygen signal is maximum. These processes are connected with the decrease of the TMR ratio at different annealing temperatures (cf. fig. 3.15). Both processes are already found and explained in very similar junctions. For a closer look see [102, 19].

3.4.2 Magnetic properties

The magnetic properties of the MTJs in dependence on the annealing temperature and the oxidation time are investigated by fitting the hysteresis loops. All samples are prepared with oxidation times of 10, 100 and 500 s and the magnetic behaviour of the top and bottom electrodes is determined: the exchange bias and coercive field of the Co-Fe and the Neel coupling and coercive field of the Py electrode.

Figure 3.13 shows the results for the bottom electrode. The exchange bias increases with increasing annealing temperature, even at 375 °C no saturation is visible. Two effects are responsible for this behaviour: (a) At low temperatures the anti-ferromagnet is only
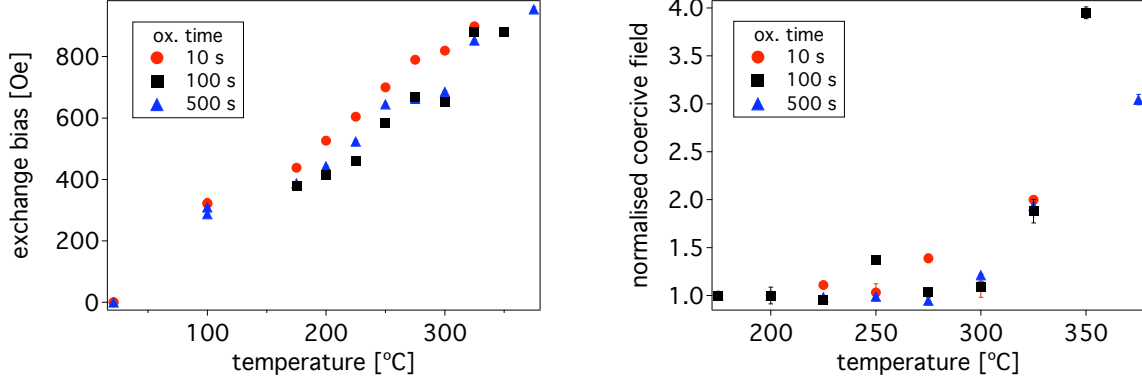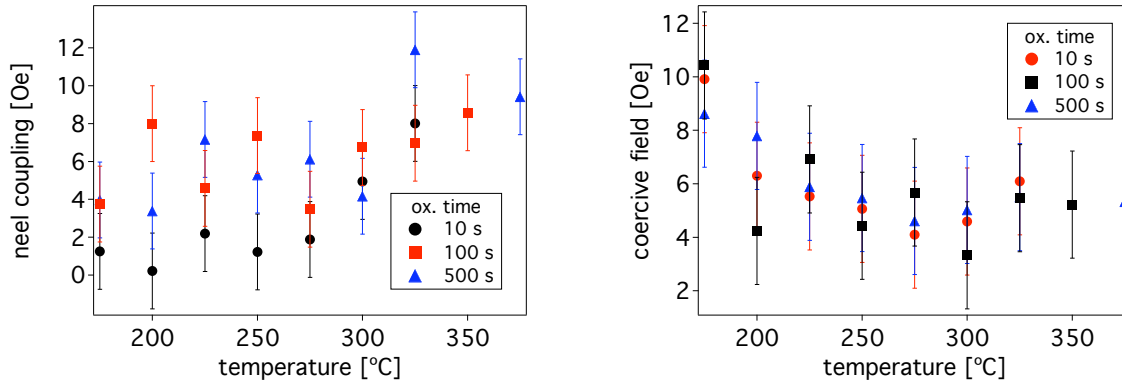
Figure 3.13: The dependence of the exchange bias (left) and coercive field (right) of the lower Co-Fe electrode on the annealing temperature and the oxidation time. Layer stack: SiO_x/ Cu30(nm)/ Mn-Ir15/ Co-Fe3/ Al1.4/ Py4/ Ta5 (+Cu55/ Au20).

partially aligned after the field cool. Increasing the temperature results in increasing the exchange bias until the blocking temperature is reached. Please note that all annealing processes in this section are made in an applied field. Therefore, the maximum field cool temperature is always the annealing temperature. (b) As discussed earlier, at higher temperatures the Manganese diffuses into the Co-Fe electrode. This diffusion reduces the Zeeman-energy of the electrode and increases the exchange bias field.

By using the theoretical expression $J_{ex} = H_{ex}\mu_0 M_{CoFe} t_{CoFe}$ [38] the surface coupling energy J_{ex} is determined, H_{ex} is the pinning field, $M_{CoFe} = 1.65 \times 10^6$ A/m [76] is the magnetisation of saturated Co-Fe and t_{CoFe} its thickness. This leads to a value of $J_{ex} = 0.32$ mJ/m^2 @ 275°C, which is the annealing temperature with the highest TMR ratio (cf. subsection 3.4.3). This fits the highest values reported for bottom spin valve type systems with Mn-Ir and Co-Fe [59, 63]. At higher temperatures the Mn-Ir and the Co-Fe are structurally changed due to the Mn diffusion towards the barrier. Hence, the used theoretical expression is not sufficient to calculate the surface coupling energy, because (at least) the Zeeman energy has changed.

The coercive field of the Co-Fe pinned at the Iridium-Manganese does not change until the annealing temperature reaches 300°C. At higher temperatures, the structural change of the Mn-Ir is also visible in the right part of figure 3.13. The coercive field suddenly increases and reaches 4 times the value of 175°C annealing temperature. This increase implies, that not only the properties of the Co-Fe are changed. The behaviour of the coercivity illustrates the changed properties of the anti-ferromagnet with reduced Manganese. The coercive field can be explained by assuming that the condition $K_{afm} t_{afm} >> J_{ex}$ is violated, with $K_{afm} t_{afm}$ as the product of anisotropy and thickness of the anti-ferromagnet. Then, the anti-ferromagnet changes its magnetisation during the hysteresis loop and increases the coercivity of the ferromagnet [38].

Figure 3.14: The dependence of the Neel coupling (left) and coercive field (right) of the upper Permalloy layer on the annealing temperature and the oxidation time. Layer stack: SiO_x/ Cu30(nm)/ Mn-Ir15/ Co-Fe3/ Al1.4/ Py4/ Ta5 (+Cu55/ Au20).

Figure 3.14 shows the dependence of the Neel coupling and coercive field of the Py top electrode on the oxidation time and the annealing temperature. Within the errors of the measurement, no significantly different behaviour is found at all. The coercive field seems to decrease slightly between 175 and 200°C annealing temperature due to an increased ordering and therefore less stray fields of the lower Co-Fe electrode. Increased ordering of the Permalloy itself is also possible. Beyond this, no dependence is found, in agreement with the results of the diffusion analysis. No diffusion was found in the top electrode up to temperatures of 400°C.

3.4.3 Transport measurements

To determine the transport properties, the TMR ratio and the IV curves are investigated in dependence on the annealing temperature and oxidation time. The TMR ratio is discussed first. The left part of figure 3.15 displays the major loop TMR ratio of the MTJs. The curve shows the typical behaviour: The TMR increases up to a certain temperature and then decreases again until it vanishes. This can be explained by two processes occurring in the junctions: One is the healing of defects in the tunnelling barrier and at its interfaces, experimentally verified by RBS and XPS [104, 105]. The second process is the diffusion of materials to the interface of the tunnelling barrier, reducing its effective spin-polarisation and decreasing the TMR ratio.

In figure 3.15 the TMR ratio increases up to 50 % (46 %, 23 %) at 275 °C at an oxidation time of 500 s (100 s, 10 s). Beyond 275 °C, it decreases again and at 400 °C the TMR ratio is nearly zero. The diffusion processes causing the decrease are already identified. The Manganese of the antiferromagnet diffuses towards the barrier and accumulates there and at 400 °C the copper also moves from the bottom conducting layer at the interface of the
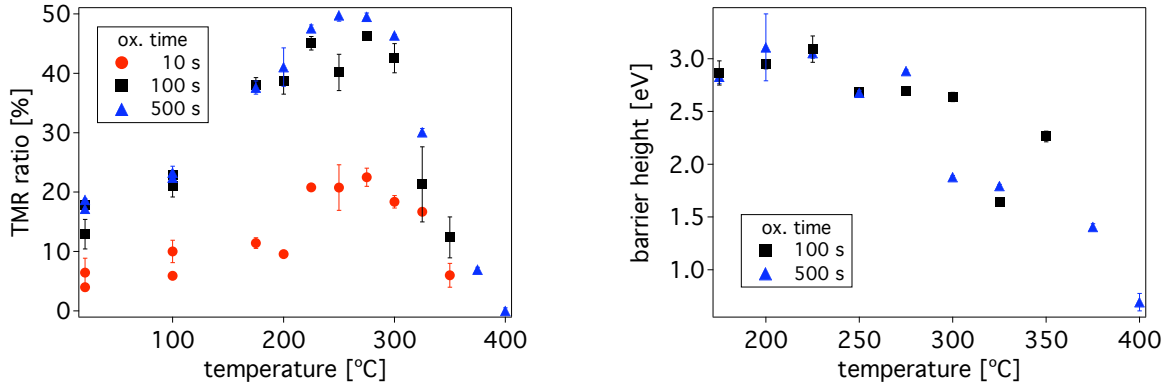
Figure 3.15: The dependence of the TMR ratio at 10 mV bias voltage (left) and the barrier height (right, using BRINKMAN's formula) on the annealing temperature and the oxidation time. Layer stack: SiO_x/ Cu30(nm)/ Mn-Ir15/ Co-Fe3/ Al1.4/ Py4/ Ta5 (+Cu55/ Au20).

Aluminium oxide.

Comparing the results for different oxidation times leads to the highest ratio at 500 s oxidation and 60 min annealing time. The earlier used standard procedure of 2 min @ 250 °C and 100 s oxidation also results in lower TMR ratios. Further investigations show an optimum annealing step of 60 min @ 275 °C at oxidation times of 100 s with an Aluminium thickness of 1.3-1.4 nm. Then, the TMR ratio reaches up to 52 %.*

Barrier parameters

The interpretation of the results obtained from the IV curves is a little bit more difficult. First, there are no values for the junctions with 10 s oxidation time. The quality of the barrier of these strongly 'underoxidised' junctions and therefore the dielectric stability of the barrier is very bad. It is not possible to apply bias voltages much higher than 10 mV and therefore every try of making an IV curve causes a broken tunnel junction. All the following figures show only the results of 100 and 500 s oxidation time.

Figure 3.15 (right) shows the barrier height, figure 3.16 (left) the barrier thickness of the investigated tunnel junctions. Both values remain constant up to roughly 300°C. Then, the height decreases from 3 eV to less then 1 eV. At 400°C the barrier thickness increases from 18 to 30 Å. Consequently, the change of the properties of the tunnel junctions and the starting diffusion processes are visible in the barrier parameters and also visible in the barrier asymmetry (fig. 3.16, right). The asymmetry remains at roughly 0.5 eV and changes extremely after 300°C. First, it increases up to 2.5 eV, then it drops again to nearly 0 eV.

---

*Because the sections in this work are not chronological, the changed oxidation and annealing procedure is not necessarily used in the next chapters.
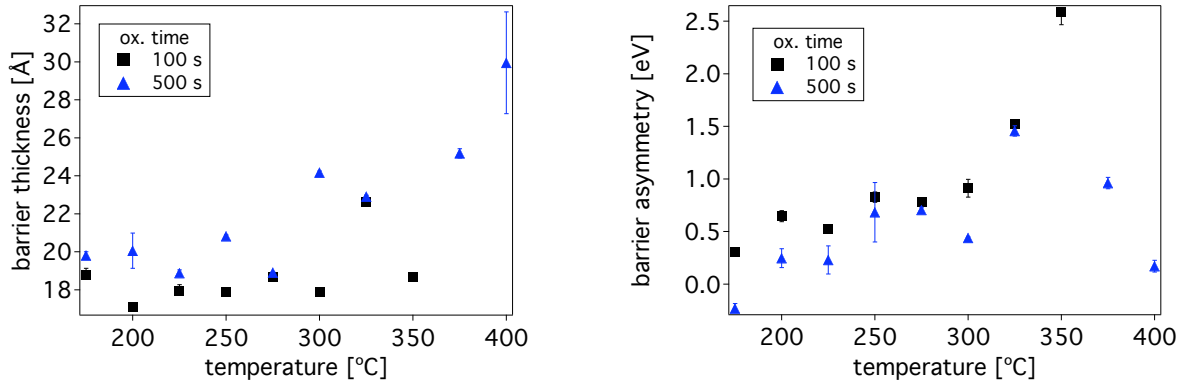
Figure 3.16: The dependence of the barrier thickness (left) and asymmetry (right) on the annealing temperature and the oxidation time using BRINKMAN'S formula. Layer stack: SiO_x/ Cu30(nm)/ Mn-Ir15/ Co-Fe3/ Al1.4/ Py4/ Ta5 (+Cu55/ Au20).

A possible explanation for the dependence of barrier parameters on the diffusion processes is given by SCHMALHORST in his PhD thesis [19]: the thin Copper layer at the interface of the barrier forms a $CuAl_2O_4$ spinel. This is possible at temperatures of more than 300°C [106, 107]. This spinel forms a second, lower potential next to the Aluminium oxide potential. With increasing thickness of this step, the barrier thickness increases, the height decreases and the asymmetry increases, too. With this model, it is possible to explain the behaviour of the barrier parameters up to 350°C. Thereafter, the two remaining data-points for 500 s oxidation time in the asymmetry plot are not sufficient to make additional conclusions.

3.5 Electric excitations in magnetic tunnel junctions

In this section the low temperature dependence of the TMR ratio is investigated. This is done by fitting the data with a simple model first discussed by MOODERA [108] (empirically) and justified by MACDONALD et. al. [109]. Even if this model might be too simple and the assumption of hopping centres might not be true, it shows the main concerns of all these kind of investigations and is used to describe the crucial points. This is followed by a comparison of different models in literature. Finally fundamental questions concerning the Julliere model and the connection between spin-polarisation and magnetisation of a ferromagnet are addressed.

The temperature dependence of the resistance was found in magnetic and non-magnetic tunnel junctions [80]. To take this into account, the Julliere model [1] is modified. The conductance G in a magnetic tunnel junction is taken as the sum of (a) the direct elastic tunnelling and (b) a part G_I independent of the relative orientation of the magnetisation

[110]:

$$G(\Theta, T) = G(T)(1 + P_1(T)P_2(T)\cos\Theta) + G_I \tag{3.3}$$

$G(T)$ is the pre-factor of the direct elastic tunnelling process. The theory predicts only a temperature dependence of a few percent due to the broadening of the Fermi distribution in the electrodes [13] and therefore $G(T)$ is assumed to be constant. Θ is the angle between the magnetisations in both electrodes.

One possibility to explain G_I is the assumption of electron hopping through N localised states, while emitting or absorbing a phonon. This leads to a temperature dependence of

$$G_I = \sum_N A_N T^\gamma \qquad \text{with} \qquad \gamma(N) = N - \frac{2}{N+1} \tag{3.4}$$

Please note that it is not possible to determine spin-polarisation and conductance independently during the fit process. The product $G(T) \times P(T)$ leads to a dependence of 1 during the fit process. Therefore, the spin-polarisation is first determined by using the Julliere model at low temperatures (10 K). The temperature dependence of the spin-polarisation scales with the magnetic moment of the electrode [111]. This leads to the Bloch $T^{3/2}$ dependence [68]:

$$P(T) = P_0(1 - \alpha T^{\frac{3}{2}}) \tag{3.5}$$

with α as a material-dependent constant. However, this relation between magnetisation and polarisation is not intrinsic [112]. It is believed that both values have the same temperature dependence, because the same physical process causes the decrease: the magnetic disorder due to thermal excitation of spin waves.

Figure 3.17 shows the temperature dependence of the TMR ratio in a $CoFe/Al_2O_3/CoFe$ junction between 10 K and 330 K. Fitting the experimental data using equation 3.3 in the parallel and antiparallel state and 3.5 leads to a spin-wave-stiffness of $\alpha = 7.6 \pm 0.4 \times 10^{-6}\,K^{2/3}$, which equals a Curie-temperature of 2600 K. This value is unphysically high (bulk Co-Fe), but addressed later. The calculation of α for different materials is waived, because all calculations need the Co-Fe value as an input parameter (the bottom electrode is always Co-Fe) and the quality of the fit process is further decreased.

As expected and previously discussed, this elastic contribution is not necessarily the only origin of the temperature dependence. There is still a big discrepancy between the experimental values and the curve only taking spin-wave excitations into account. During a second fitting process and using equation 3.4 (for example) the A_N values are calculated.

This leads to the main issue concerning all these kind of investigations. Because all parts of the sum in equation 3.4 (and other contributions of different models) have 'flat' dependencies on the temperature, it is not possible to separate them during the fit. The curve fits the better the more terms are used, but this has only limited physical meaning. The correlation matrix [20] shows a correlation close to 1 for all $N > 2$. Already only using $N = 2$ shows a good agreement of the experimental and calculated values. Figure 3.17
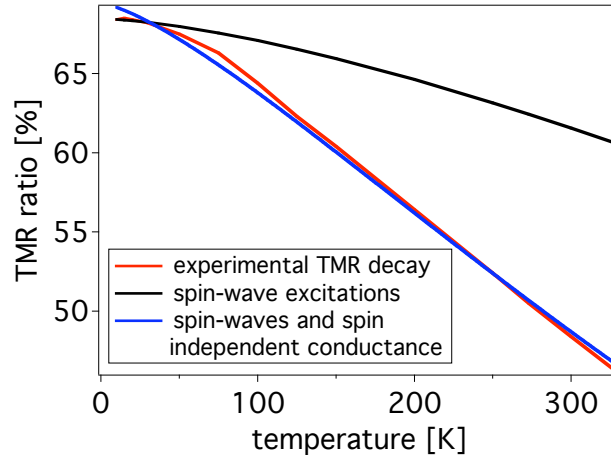
Figure 3.17: Experimental and calculated temperature dependence of a magnetic tunnel junction. The red line shows the experimental values, the black lines takes magnons into account. The blue line also considers phonon absorption and emission. A spin-wave-stiffness of $\alpha = 7.6\pm0.4\times10^{-6}\,\mathrm{K}^{2/3}$ was found. Layer stack: SiO_x/ Cu30(nm)/ Mn-Ir15/ Co-Fe3/ Al1.4+ox./ Co-Fe1.5/ Py4/ Ta5 (+Cu55/ Au20).

shows the fit for $N \leq 2$. Although, one might note that the assumption of two localised states in a 1.8 nm (6 monolayer) thick tunnel barrier might be questionable.

The strong correlation of the parameters makes it difficult to give more than qualitative explanations. This is also true assuming more sophisticated models. Another possibility to explain the inelastic current is electron scattering at paramagnetic impurities [113], because the bottom interface of the tunnel barrier could contain impurities due to overoxidation. The conductance and magnetoresistance is then approximately temperature independent [114]. This contradicts the experimental results. Moreover, the oxidised impurities of the Co-Fe electrode should become anti-ferromagnetic at lower temperatures and the spin scattering will be further reduced [108].

DIMOPOULOS explains in his PhD thesis the temperature dependence of the conductance and TMR ratio with excitation of magnons and phonons in the electrode of the junctions. Without describing his model in detail, the temperature dependence can also be fitted using this model. But carefully investigating the correlation matrix (at least when fitting our data) shows no separation of the coefficients. Therefore, no quantitative information can be received.

DAVIS explains the temperature dependence of the polarisation by a Stoner-like collapse of the exchange splitting [115]. The use of this model for bulk Co leads to a drop of the TMR ratio of only 30 % of the experimental values. However, the Curie temperature of the interface should be significantly lower. Furthermore, the model results in a more complicated dependence of magnetisation and polarisation, indicating that equation 3.5 is

not necessarily true (also found for our data) and G_I in equation 3.3 can be waived.

ZHANG introduces a cut-off energy E_C which replaces the maximum magnon energy [116] and sets the relevant energy scale. The cut-off frequency is justified by interface anisotropy and/or finite coherence length-scales due to grain sizes. The temperature dependence of the conductance is then described as $G(T) \simeq T \ln(k_B T / E_C)$.

The Curie temperature of 2600 K of the ferrromagnetic Co-Fe electrodes has still to be explained. Already DAVIS pointed out, that the connection between spin-polarisation and magnetisation might be more complicated than linear. But there was no way to prove this hypothesis, because larger spin-wave-stiffness values than expected were found. But surfaces (the TMR effect is surface sensitive) have normally a larger spin-wave-stiffness [117, 118] and also spurious effects could further decrease the spin-polarisation at higher temperatures.

In this thesis, a high initial spin-polarisation of Co-Fe more than 50 % and a lower spin-wave-stiffness, leading to a higher Curie temperature is found. Only 4 explanations are possible: (a) The spin-polarisation of $Co_{70}Fe_{30}$ is significantly higher and here reduced due to not-perfect preparation conditions. (b) The application of the Bloch $T^{3/2}$ dependence (cf. eqn. 3.5) on the spin polarisation is not justified. (c) The connection between conductance and spin-polarisation in the Julliere model is not correct (cf. eqn. 3.3). (d) The anti-ferromagnet increases the (virtual) Curie temperature of the lower Co-Fe electrode tremendously [119]. All these possibilities lead to very interesting questions and will be further investigated.

In summary, the temperature dependence of the TMR ratio in magnetic tunnel junctions is investigated. Assuming the Bloch $T^{3/2}$ law and the Julliere model for the spin polarisation, only spin-wave (magnon) excitations can not explain the strong decay between 10 K and 330 K and an un-physically high Curie temperature is found. The fundamental question remains, if the application of Julliere's model and Bloch's law are justified.

If it is justified, one has to take the spin-independent conductance into account. This conductance could originate from phonon emission or absorption due to 2 state hopping, for example. The more complex model of DIMOPOULOS leads to strongly correlated fit parameters. Therefore, it is not possible to give quantitative values. Nevertheless, it is not necessary to assume hopping to explain the temperature dependence of the TMR ratio. Different contributions in different models can also describe the temperature dependence of the TMR ratio, even without inelastic processes.

3.6   Noise measurements

Because different names for the same kind of noise in different publications are used, these names are shortly introduced: The noise caused by random fluctuations in the motion of quantised charge carriers in a conductor is called shot noise [120]. The noise generated by thermal excitation of electrons in a conductor is called thermal noise (or Johnson noise, Nyquist noise) and depends only on the temperature [120]. Shot noise and thermal noise show a very broad frequency distribution and therefore this is called white noise. Flicker

noise ($1/f$ noise) in a conductor is caused by charge traps. If the time constants of charge and discharge of the traps are homogeneously distributed the noise power is proportional 1/f [120].

Due to their potential applications as non volatile memory or sensor devices a lot of effort was put in the development of TMR junctions with high TMR ratio. But from the application point of view the signal to noise ratio (SNR) is equally important. In an integrated circuit the high TMR ratio is worthless if the noise is equally increased. Despite of the importance of noise measurements there are only several reports about the noise properties of magnetic tunnel junctions [121, 122, 123, 124, 125, 126].

NOWAK reported [121] that junctions with larger magnetoresistance (25 %-30 %) also have low noise power. Low MR (3 %-5 %) junctions exhibited random telegraph and flicker noise with higher noise power. The two-channel model leads to a noisy spin independent channel, these junctions' noise is field independent and as a consequence not magnetic in origin. This was further investigated [122] in junctions with higher TMR ratio (up to 35 %) and varying the Aluminium oxide thickness. The $1/f$ noise at large bias voltages is attributed to trapping processes and depends sensitively on the relative position of the oxide edge and the ferromagnet Aluminium interface.

INGVARSSON studied magnetic tunnel junctions (TMR ratio 25 %-30 %) of small dimensions ($\sim 1\,\mu m^2$) [123]. At low frequencies they observed noise with a Gaussian amplitude distribution and pure $1/f$ spectra. They found evidence of charge traps and noise caused by magnetic dynamics (e.g. reversible domain wall jumps), which is, however, a very individual property of every MTJ. The magnetic noise was further investigated [124] and a correlation between thermal stability of the magnetisation and low noise in MTJ was found.

NOWAK investigated the noise in MTJs with an additional Iron interlayer at one barrier interface [125]. The Iron interlayer increases the TMR ratio at the expense of higher noise, the origin is not further explained. In summary, all these investigations are made with at least 3 years old tunnel junctions prepared by PARKIN'S group and (from today's point of view) with MTJs of medium TMR ratios. KIM reported in 2002 an increase of noise power density in the field region of the switching from antiparallel to the parallel state in MTJs with a TMR ratio of 13.5 %. The noise density is reduced by thermal annealing because noise from magnetic origin is reduced. Further investigation of the noise is needed to understand and separate different reasons of noise in magnetic tunnel junctions.

At the Massachusetts Institute of Technology (MIT) a noise measurement setup adopting cross correlation techniques is available. The voltage noise is measured as a function of bias voltage, magnetic field, and temperature. The white noise of standard resistors is shown in figure 3.18, the not correlated noise caused by e.g. the amplifiers, wires, and contacts is removed for resistances down to $\sim 10\,\Omega$ by a two channel spectrum analyser HP35670A. The amplifiers have bandwidths of $\sim 20\,\mathrm{kHz}$ and a white noise level of $\sim 1.0\,\mathrm{nV/Hz^{1/2}}$. All measurements are done in a shielded room to avoid (radio)-frequency interference and evironmental vibrations. The measured samples are prepared in Bielefeld (BI), by Non Volatile Electronics (NVE1/2), and the MIT. The characteristics of these samples are shown in table 3.3. The Hooge parameter α_H is explained later.
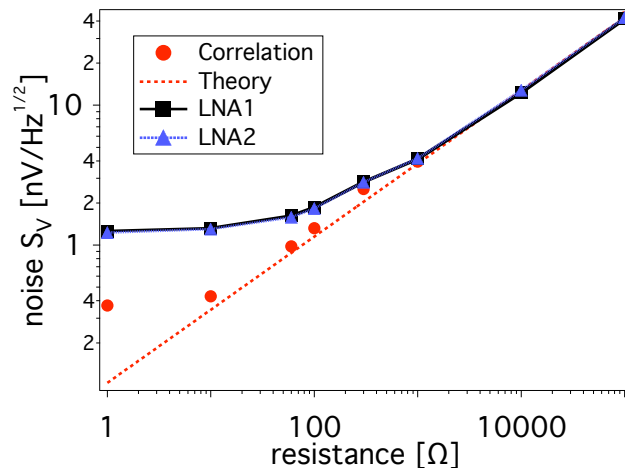
Figure 3.18: White noise level of standard resistors measured with two low noise amplifiers (LNA) and corrected by cross correlation technique.

sample	size $[\mu m^2]$	R(295 K) $[\Omega]$	R(77 K) $[\Omega]$	TMR(295 K) [%]	TMR(77 K) [%]	α_H $[\mu m^2]$
BI	400×400	77	85	50	60	5×10^{-8}
NVE1	33×20	2500	–	34	–	1×10^{-9}
NVE2	33×25	1900	3060	35	47	2×10^{-9}
MIT	$6.0 \cdot 10^4$	1500	–	8	–	1×10^{-6}
NTJ	$2.7 \cdot 10^6$	150	–	–	–	6×10^{-2}

Table 3.3: Characteristics of the samples for noise measurements, BI prepared in Bielefeld, NVE1/2 prepared by Non Volatile Electronics, MIT and NTJ by the MIT

Junctions show a sum of $1/f$ and white noise, the white noise consists of shot noise and Johnson noise. Theoretical predictions lead to a noise spectrum $S_V(f)$ described by [122]:

$$S_V(f) = 2\,\mathrm{e}\,I \coth\left(\frac{\mathrm{e}V}{2\mathrm{k_B}T}\right) R_d^2 + \alpha_H \frac{V^2}{Af^\gamma} \tag{3.6}$$

e is the electric charge, $\mathrm{k_B}$ the Boltzmann constant, R_d the differential tunneling resistance ($R_d = dV/dI$), I/V the current/ voltage, A the tunneling area, T the temperature, f the frequency. In the limit of high temperatures or zero bias voltage the noise is dominated by the white noise term. In the low frequency range the noise is mainly generated by flicker noise. γ is a parameter to decide if the frequency dependent noise is $1/f$ noise or e.g. $1/f^2$. The Hooge parameter α_H is a value to specify the size of the $1/f$ noise in junctions with different areas.

To understand the origin of noise in magnetic tunnel junctions it is important to separate the magnetic and the non magnetic part. To take this into account non magnetic tunnel junctions (NTJ) are prepared at the MIT. So 4 different systems are available: BI, NVE1(2), MIT, and the NTJ. BI is the well known and described system AF5. NVE1 and NVE2 are sputtered having exchange biased structures in a stack of Cr-Pt-Mn/ Fe-Co/ Ru/ Fe-Co/ AlO$_\mathrm{x}$/ Ni-Fe-Co [127]. MIT is prepared by vacuum evaporation in a stack of Si/ Co/ AlO$_\mathrm{x}$/ Py/ Co [4] and the NTJ is prepared by evaporation and oxygen plasma oxidation in a stack of Al/ AlO$_\mathrm{x}$/ Al [4].

The noise characteristics of all investigated junctions do not show any dependence on the magnetic state. Only at the switching field where one electrode changes its magnetisation an enhancement of the noise was found. This was also found by INVERSSON [124] but is here not further investigated. Because no field dependence was found in equilibrium states magnetisation fluctuations might not be the origin of the noise respectively their contribution to the total noise is not very high. Therefore, all investigation presented here are made in the parallel magnetisation state.

The bias voltage dependence of the voltage noise power spectral density is shown in figure 3.19. The plots on the left side are at 77 K, the plots on the right side are at room temperature. As mentioned before (discussing equation 3.6) the total noise is a sum of $1/f$ and white noise. The white noise consists of shot and thermal noise and is dominant at higher frequencies. With increasing bias voltage the frequency where the white noise is dominant is also increasing. This behaviour is often found in magnetic tunnel junctions. γ in equation 3.6 was determined to be: 1.0 (NVE2), 1.3 (BI) and 1.0 (MIT). The $1/f$ behaviour of the noise is due to charge traps and resistance fluctuations in the barrier and the interfaces [122].

Additionally, the junctions are cooled down to 77 K and measured again. The left plots in figure 3.19 show very different spectra, but the change is expected. The white noise dominates now up to lower frequencies. This can again be explained by the assumption of a sum of thermal noise, shot noise, and $1/f$ noise [122].

Moreover, a non-magnetic tunnel junctions was measured, this NTJ is shown in figure 3.20. A strong $1/f$ behaviour with a γ of 1.6 is found at room temperature. At 77 K the
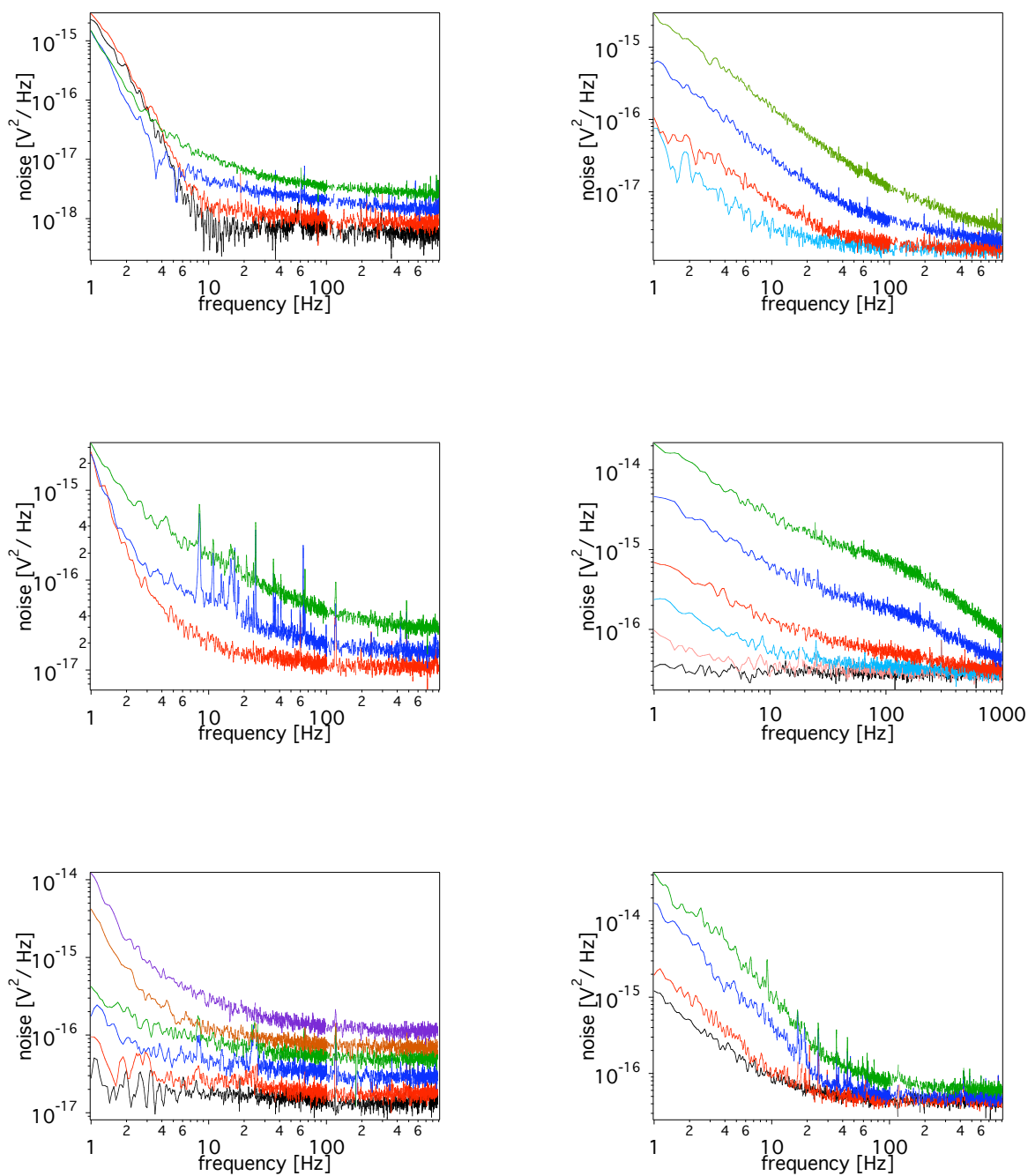
Figure 3.19: Bias voltage dependence of voltage noise power spectral density of MTJs. (Upper left) Prepared in Bielefeld (BI) and measured at 77 K, bias voltage from bottom to top: 0, 20, 50, 100 mV. (Upper right) BI @ 295 K, 10, 20, 50, 100 mV. (Middle left) NVE2 @ 77 K, 20, 50, 100 mV. (Middle right) NVE2 @ 295 K, 0, 5, 10, 20, 50, 100 mV. (Lower left) MIT @ 77 K, 0, 20, 50, 100, 200, 400 mV. (Lower right) MIT @ 295 K, 0, 20, 50, 100 mV.
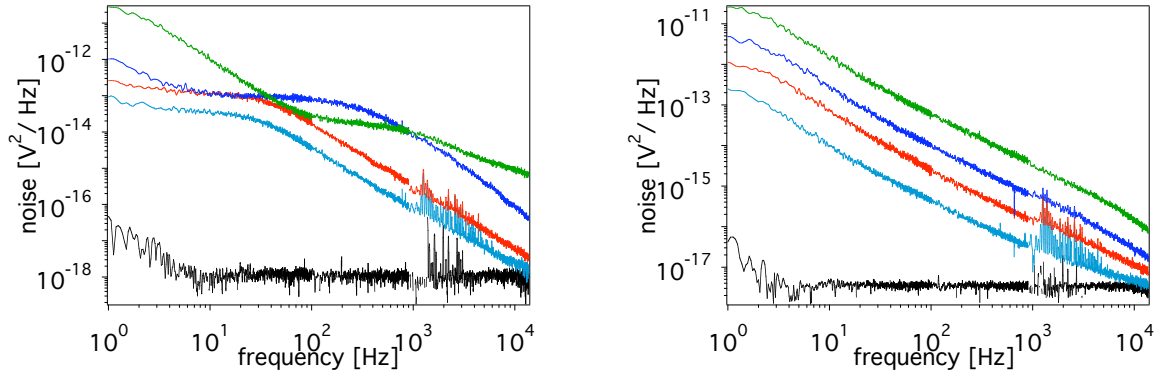
Figure 3.20: Bias voltage dependence of voltage noise power spectral density of the NTJ. Bias voltage from bottom to top: 0, 10, 20, 50, 100 mV. (Left) 77 K (Right) room temperature.

spectrum is absolutely different from the MTJs shown in figure 3.19. Lorentzian shaped noise spectra is found with increasing bias voltage. This is attributed to a single two level fluctuator in the barrier or at one interface.

This is even more evident looking at figure 3.21. The voltage vs. time plot measured at 10 mV clearly shows 2 different states. Theoretical predictions point out that the superposition of a lot of two level fluctuators will result in a $1/f$ behaviour at higher bias voltages. And indeed at 100 mV already two Lorentzians can be seen.

To compare the noise level of the different (non)[†] magnetic tunnel junctions the Hooge parameter α_H is used (cf. eqn. 3.6). The Hooge parameter is a measure to determine the $1/f$ noise independent of the junction area. α_H was measured in the noise spectra at 10 Hz and at a bias voltage of 100 mV. The result and the TMR ratio of the junctions is plotted in figure 3.21. It is believed that the noise level in magnetic tunnel junctions is caused by impurities at the barrier electrode interfaces [128]. Therefore, it is expected to find higher TMR ratios and lower noise levels and vice versa. But the results shown in figure 3.21 contradict this prediction. Although the noise of junction BI is higher by almost one order of magnitude, the TMR ratio is much higher (50 % cp. to 35 %). The noise seems to scale with $R \times A$ which is very interesting from the application point of view because MRAMs or magnetic read heads for hard disks should have a very low area resistance.

In summary, the noise properties of magnetic and non magnetic tunnel junctions prepared in 3 different labs were investigated. $1/f$ and white noise was found in the investigated frequency range of 1 to 10 kHz. The $1/f$ noise at 10 Hz and 100 mV scaled with the product of area and resistance. This is promising from the application point of view but the origin has to be further investigated.

This results presented in this section are a collaboration between WAN KYU PARK,

---

[†]The non-magnetic tunnel junctions are quite different from the MTJs. The oxidation process leads to different Oxygen distributions and chemical bonding, due to similar electrode and barrier materials.
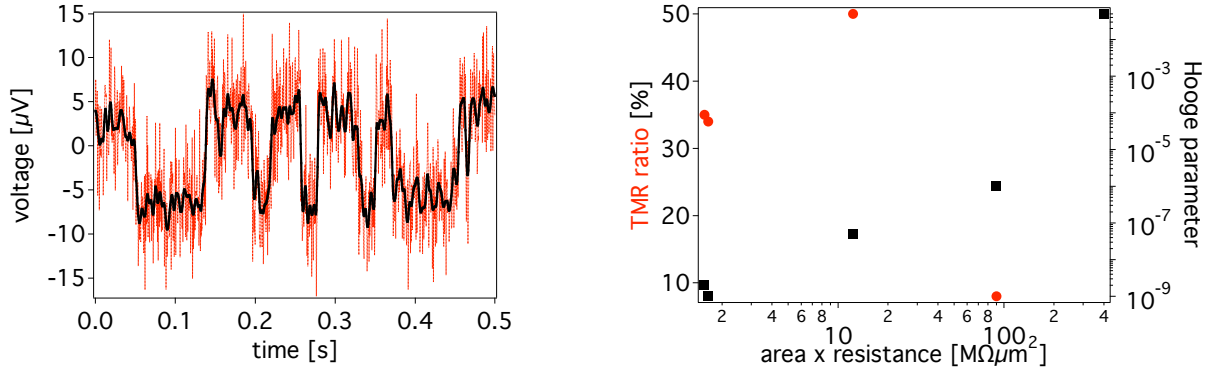
Figure 3.21: (Left) Voltage vs. time plot of the NTJ showing a 2 level fluctuator, the black line corresponds to smoothed values. (Right) Hooge paramter and TMR ratio of the different (non) magnetic tunnel junctions vs. their area resistance.

JAGADEESH MOODERA (MIT), Non Volatile Electronics, and our group. All measurements were done at the MIT and the results are published in [129].

3.7   Spin polarisation in ferromagnetic double layer electrodes

Another basic question concerning tunnel magnetoresistance is not finally answered: already the seminal work from Tedrow and Meservey showed that the behavior of electrons tunneling through a barrier only depends on the wave function of the first several atomic layers [130]. Another way to determine the effective length-scale of the tunneling electrons is the introduction of a nonmagnetic metallic layer (e.g. Cu, Cr) between one magnetic electrode and the tunnel barrier [131]. Again, the spin polarization decay length was found to be obviously less than 1 nm. Besides the very low decay length, Yuasa found strong oscillations in the TMR ratio in dependence on the interlayer thickness, but in epitaxial systems [132].

In this work, a further experiment was conducted, in which a second ferromagnet with a different spin-polarization is introduced between the magnetic electrode and the tunnel barrier. With this composite electrode, it is also possible to determine the effective thickness where electrons contribute to the tunneling current. The characteristic length of the contribution to the tunneling current should be given by an exponential decay. If that decay length is very short (a few monolayers) only the interface states determine the spin polarization, if the decay length is a few nanometers, also the bulk-states contribute.

To determine the spin polarization in different ferromagnetic materials, different top electrodes are used (e.g. Co, Ni, . . .). To determine the spin polarization decay length, a
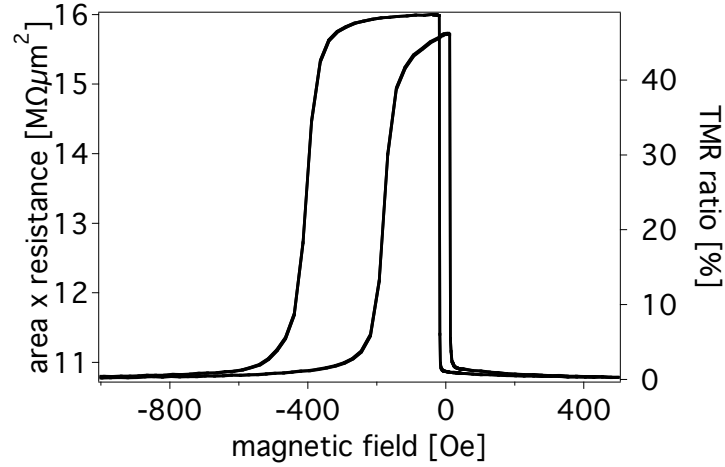
Figure 3.22: Magnetoresistance of an exchange biased magnetic tunnel junction with 0.5 nm Nickel interlayer at room temperature. Due to the clearly separated states the TMR ratio/ spin polarization can be exactly determined.

Nickel layer with variable thickness followed by a 3 nm thick $Co_{70}Fe_{30}$ layer forms the top electrode. The influence of this Nickel interlayer on the TMR ratio is investigated. The top electrode is always covered with Ta 3/ Cu 55/ Au 20. All layers have no intentionally induced anisotropy. As mentioned before the layer stack is 2 minutes annealed after sputtering at 523 K in a magnetic field of 1000 Oe and then field cooled to activate the exchange biasing. The stacks are patterned to squared junctions with sizes of 300^2, 200^2, 100^2, 22.5^2 and 7.5^2 μm^2.

Table 3.2 (section 3.2) shows the spin polarization values for all tested materials. The Brinkman fit leads to a barrier height of $\phi \geq 3.0\,eV$ and a barrier thickness of $d = 1.6$-$1.7\,nm$ (Al barrier 1.4 nm + oxidation). Clearly separated magnetic states are necessary to determine the spin polarization from the TMR ratio. Otherwise, every change of the magnetic behavior also changes the TMR ratio and apparently the calculated spin polarization. Figure 3.22 shows the major loop of an exchange biased MTJ with 0.5 nm Nickel interlayer at room temperature.

In addition to the separated magnetic states, one has to take extrinsic structural differences into account. LeClair inserted a thin Copper layer between one magnetic electrode and clearly demonstrated the differences between insertion below or above the tunnelling barrier [131]. In our case, MTJs with two Permalloy electrodes are prepared and show only a TMR ratio of ~ 50% at low temperatures. If a Gadolinium seed layer is introduced the TMR ratio reaches $\geq 70\,\%$ at low temperatures and fits the calculated value in table 3.2 [82].

Therefore - to address these uncertainties for the experiment with the Ni/ Co-Fe elec-
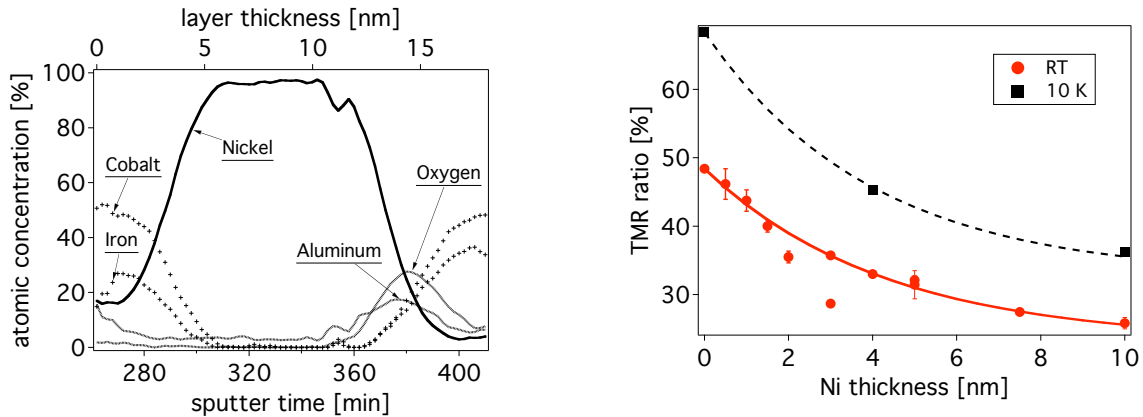
Figure 3.23: Left: Auger depth profile of the magnetic tunnel junction with a Nickel interlayer thickness of 10 nm. Only the region from the top to the bottom electrode is shown, the concentrations are calculated via the target factor analysis. Right:TMR ratio vs. the Ni interlayer thickness in an exchange biased Mn-Ir/ Co-Fe/ AlO$_x$/ Ni/ Co-Fe magnetic tunnel junction. The lines correspond to a fit described in the text.

trode - the structure below the tunnel barrier is never changed and the structure above is checked with Auger depth profile measurements. Within the resolution this technique (~ 1.5 nm) granular growth and/ or interdiffusion due to the annealing process would be clearly visible. Figure 3.23 shows an example, the Auger depth profile of the sample with a Nickel interlayer thickness of 10 nm. No interdiffusion or non-layer structure of Nickel and Cobalt-Iron is visible.

Figure 3.23 shows the TMR values of the MTJs with different Nickel interlayer thickness at room temperature and at 10 K. The curve has the expected form, it is possible to fit an exponential decay ($A + B \exp(-tC)$) to the measured values. A,B, and C are the fit variables and t the Nickel thickness. Assuming the 21.6 % TMR ratio of a pure Nickel electrode for infinite thickness (100 nm) at room temperature (32.7 % at 10 K) the fit leads to a spin polarization decay length of $1/C = 4.3\pm0.2$ nm at room temperature (4.0 ± 0.3 nm at 10 K) for the tunnelling electrons.

Two results are obvious at first glance: The room temperature and 10 K values are the same within their errors and (due to the large $1/c$ value) there is a contribution of the electrons beyond the interface. It is not possible to explain these results only by assuming granular growth and/ or interdiffusion at a length-scale below the resolution of our Auger microscope. Even for the 4 nm Nickel/ 3 nm Cobalt-Iron double-layer, there is still a difference of 33 % TMR ratio compared to 22 % for the pure Nickel layer at room temperature (45 % resp. 32 % at 10 K).

Although, this seems to contradict the previous results of LeClair or Meservey and Tedrow, the insertion of a second *ferromagnetic* layer is a different experiment. There is the same big difference comparing the results of Jedema [133] with the results of LeClair

[131]. The spin polarization decay length of the *tunnelling* electrons ($\lesssim 1\,\text{nm}$ in Cu at room temperature) is different from the spin diffusion length of the *conducting* electrons in a spin valve structure ($\sim 350\,\text{nm}$ in Cu at room temperature). The different nature of the shown experiment is also visible in the absence of a temperature dependence. Spin diffusion length-scales are always temperature dependent, because the spin scattering rate increases with increasing temperature.

There are a lot of publications about magnetic tunnel junctions, but only a few investigate composite electrodes. Ho found an enhancement of the TMR ratio of up to 4.45 times by adding Co or Co-Fe at the interface of the insulator (Al_2O_3) and the Ni-Fe electrode. But the very sharp TMR peaks in their major loops make it impossible to separate between a change of the coercive field and the contribution of the changed spin polarization and lead to wrong conclusions [134].

Zhu investigated a wedge shaped Co-Fe interlayer at one interface of a Py/ Al_2O_3/ Py tunnel junction and found a 'bulklike contribution' with a characteristic length of $0.8\,\text{nm}$ [135]. But in this length-scale, there is no analytical method available to rule out effects due to roughness or other spurious effects.

The spin polarisation decay length found here leads to a band-structure effect rather than to a spin diffusion length. The value of $4.2\,\text{nm}$ (within their errors) is independent of the temperature between $293\,\text{K}$ and $10\,\text{K}$. Also a hybridisation of the Nickel s-electrons and the Co-Fe d-electrons is possible, this would also explain the very different result for Nickel compared to Copper interlayers. Quantum well states (such as Yuasa found [132]) can not explain the investigated behaviour. The sputtered layers on amorphous Si-oixde substrates will de-phase the quantum well states in such a way, that they are averaged out.

The obtained results are very interesting, because one would expect a different picture [136]: If a conduction electron encounters a boundary between a ferromagnet and a metal it will be reflected or transmitted. The ratio between these two possibilities is mainly determined by the difference in their Fermi velocities. Without taking many body interaction into account, the spin of the electron is conserved (at least) until it has a momentum collision caused by lattice imperfections such as impurities or grain boundaries.

If a conduction electron encounters an interface between two ferromagnets there is another effect. Because of the spin of the electron, there will be an exchange interaction between the electron and the spin polarised states of the second ferromagnet. This interaction might also flip the spin of the electron and one has to take many body interactions into account. The electron gives up its individuality and is now part of the electron gas. This electron gas is in its equilibrium only at the average spin polarisation of the second ferromagnetic metal, so the spin should flip very fast.

But in both pictures generally used to explain the electron tunnelling, the *quantum-mechanical nature* of the tunnelling process itself is lacking. The next paragraphs try to take quantum-mechanics into account, by pointing out concepts rather than presenting formulas. Even if the reader might question the premise from the very beginning, it is (to the authors best knowledge) compatible to most spin-injection experiments through a tunnel barrier: *It is not possible to inject spin polarised current from a ferromagnet in the remanent state through a tunnel barrier into a non-magnetic semiconductor or metal.*

In 2000 SCHMIDT found a 'Fundamental obstacle for electrical spin injection from a ferromagnetic metal into a diffusive semiconductor' [137]. The highly different conductivities of the ferromagnet and the semiconductor lead (if investigating the chemical potentials) to a very poor spin-injection efficiency. He suggested the use of $100\,\%$ spin-polarised materials to overcome this obstacle. Only one months after publication, RASHBA solved the so called conductivity mismatch problem by introducing a tunnel barrier between the spin injector and the semiconductor [138]. He showed the possibility of a high spin injection ratio in such a device.

But there is also a fundamental obstacle when tunnelling from a ferromagnet through a barrier into a non-magnetic semiconductor (or metal) and its origin lies in quantum-mechanics: if an electron of the ferromagnet starts tunnelling, it has a spin parallel or anti-parallel to the magnetisation direction. The magnetisation *defines* a spin direction. 'During' the tunnelling process, the electronic wave-function has a certain probability to be found at one or at other side of the barrier. If the electron is now detected at the other side of the barrier, the wave-function collapses. But it collapses into a state, where the spin direction is not defined. Therefore, there is no spin injection.

If there is a ferromagnet at the other side of the barrier, the situation changes: the spin direction is again defined and one can measure the TMR effect. The same situation occurs, if a magnetic field is applied. A large external field also defines a spin-direction and spin-polarised currents can be detected. Although, one might immediately doubt this concept, due to the large number of successful spin-injection experiment, it is compatible with (to the authors best knowledge) most of them. Even more, now it is possible to explain the fundamental different nature of the experiments of LECLAIR compared with the composite electrodes of JEDEMA.

In our experiment with composite electrodes, a spin-direction is defined at both sides of the tunnel barrier. In JEDEMA'S first experiment [133], an all-metal spin-valve without tunnel barrier is used, whereas in the second experiment, a tunnel barrier was introduced [139]. In this article, spin precession is detected. But the precession is only detected with high external fields. The major loops are visible, because a small magnetic field is applied (no minor loop is shown) or due to spurious effects as suggested by JOHNSON [140]. LECLAIR investigated tunnelling from a ferromagnet into a metal such as Copper or Chromium followed by a second ferromaget [131]. He calculated an *upper limit* for the decay length of below $1\,\mathrm{nm}$. Exacly this behaviour is expected in the described model.

There are quite a few publications such as [141, 142] about spin injection through a tunnel barrier into a semiconductor with (circular) polarised light as the detected signal. But in these kind of experiments an external field is needed to create the circular polarised light out of the linear polarised one. The quantum-mechanical origin of the described concept is again obvious: the measurement (applied external field) changes the result.

Further theoretical calculations have to show, if it is possible to put this concept (it is more a concept than a model) into a solid physical formulation. If so, the consequences are quite obvious with a large impact on possible device configurations: it is not possible to inject spin polarised current from a ferromagnet in the remanent state through a tunnel barrier or directly into a non-magnetic semiconductor. Only the possibility to use materials

with 100 % spin-polarisation, the use of magnetic (at room temperature!) semiconductors or tunnel barriers remains.

Further investigations of MTJs with composite electrodes of different ferromagnetic materials are necessary and planned to show the relationship between the spin polarisation of the tunnelling electrons and the characteristic length scales in a ferromagnetic or metallic layer. Preparation with magnetic masks during the sputtering process instead of an annealing step to activate the exchange bias will exclude any uncertainties related to interdiffusion of Co-Fe and Ni.

In summary, the polarisation of $Co_{70}Fe_{30}$ is found to be 0.43 at room temperature (0.50 at 10 K), the polarisation of Nickel is much lower: 0.23 (0.28). The big difference between these two materials is used to determine the spin polarisation decay length of the tunnelling electrons. Therefore, magnetic tunnel junctions are prepared with a composite top electrode consisting of 3 nm Cobalt-Iron and a Nickel interlayer with variable thickness, the layer structure was carefully investigated by Auger depth profiles. The spin polarisation decay length of the tunnelling electrons propagating from the Cobalt-Iron into the Nickel layer and through the barrier is found to be 4.0 ± 0.3 nm at 10 K.

Chapter 4

Double barrier junctions

The development of double barrier tunnel junctions (DBJ), which consist of two stacked magnetic tunnel junctions (in this chapter the abbreviation SBJ for single barrier junction is used instead of MTJ), is interesting from the physical and the application point of view. On the one hand ballistic effects [143] and resonant states [144, 145] are predicted, leading to higher magnetoresistance values. On the other hand, it might be possible to build a multivalued logic and improve the bias voltage dependence in applications [62]. To prepare DBJs two different techniques are tested: Successive and complete oxidation. Figure 4.1 shows a scheme of these two methods.

In section 4.1 the second method is introduced, discussed and compared with the first one. That was done by SACHER partly under my guidance during his diploma work. For a closer look see [101].

4.1 Preparation by complete oxidation

In this section, the investigations of the magnetic tunnel junctions prepared with two barriers in one oxidation step are presented. The systematic investigations of the oxidation process on the one hand and the reduction process on the other hand is necessary to decide, if it is possible to prepare double barrier junctions with one oxidation step. No oxygen should be left in the ferromagnet, but also all metallic Aluminium has to be oxidised. A very simple model (only taking formation enthalpy into account) should clarify the question, if this might be possible at all:

$$3\text{FeO} + 2\text{Al} \rightharpoonup \text{Al}_2\text{O}_3 + 3\text{Fe} \qquad \Delta H = -205\,\text{kcal/mol} \qquad [146]$$
$$3\text{NiO} + 2\text{Al} \rightharpoonup \text{Al}_2\text{O}_3 + 3\text{Ni} \qquad \Delta H = -229\,\text{kcal/mol} \qquad [146]$$

Because these reactions free energy, the formation of Al_2O_3 is preferred. Furthermore, ZHANG [147] and ROOS [148] experimentally verified the Iron reduction.
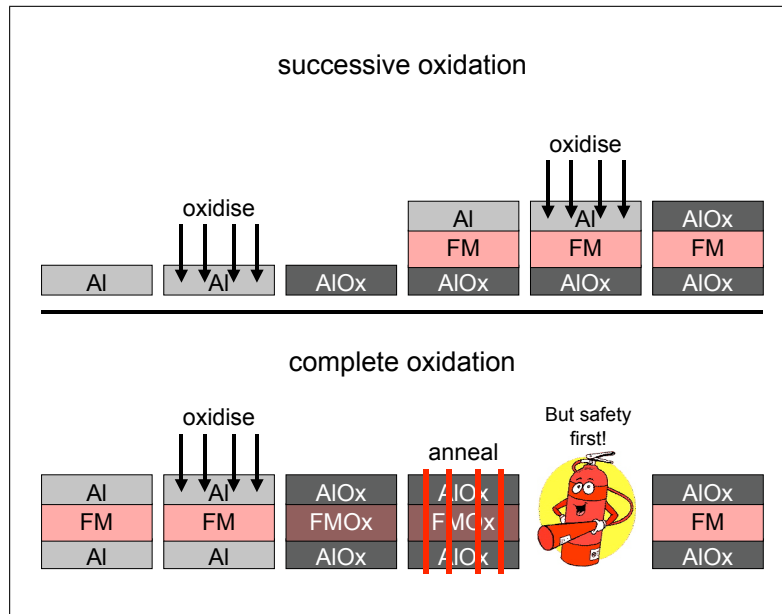
Figure 4.1: The two different oxidation techniques used to prepare double barrier junctions. Top: successive oxidation: Each of the two barriers is prepared like in a single barrier junction. Bottom: The two aluminum layers and the ferromagnet in between are oxidised together. The ferromagnet is reduced by thermal annealing.

4.1.1   Permalloy interlayer

Auger investigations of a 2.8 nm thick Aluminium layer on top of the 'standard' TMR stack without top electrode (Cu30 (nm)/ Mn-Ir15/ Co-Fe3/ Al2.8) are made to determine the depth of the oxidation process. Figure 4.2 (left) shows the result. After 200 s oxidation time the ratio saturates (100 s is used for 1.4 nm Al), the ratio of about 2:1 means 2/3 of the metallic Aluminium is oxidised. That corresponds to a maximum oxide thickness of about 2.6 nm (2 nm × 1.3 because of oxidation and Oxygen deposition). This value fits the theoretical and experimental oxidation depth found by Cabrera [149]. It is not necessary to oxidise the whole Aluminium in the double barrier junctions. One has to oxidise the upper Aluminium and deposit enough Oxygen in the interlayer. During the reduction step, the Oxygen should leave the interlayer and oxidise the bottom Aluminium.

To investigate that behaviour, double barrier junctions with Permalloy interlayer are prepared (Cu30 (nm)/ Py4/ Mn-Ir15/ Co-Fe3/ Al1.4/ Py x/ Al1.4). The ratio of Aluminium oxide to Aluminium is again determined for a constant oxidation time of 800 s. It can be clearly seen, that the Permalloy layer 'protects' the bottom Aluminium layer from oxidation. Starting at very thin Permalloy layer thickness of 1 nm the ratio saturates at 1:1. This means 50 % of the Aluminium is oxidised, viz. only the top barrier. MOKE measurements exhibit that a interlayer thickness of 2-3 nm Permalloy is necessary to have a ferromagnetic layer. At this layer thickness the oxidation of the bottom electrode is not
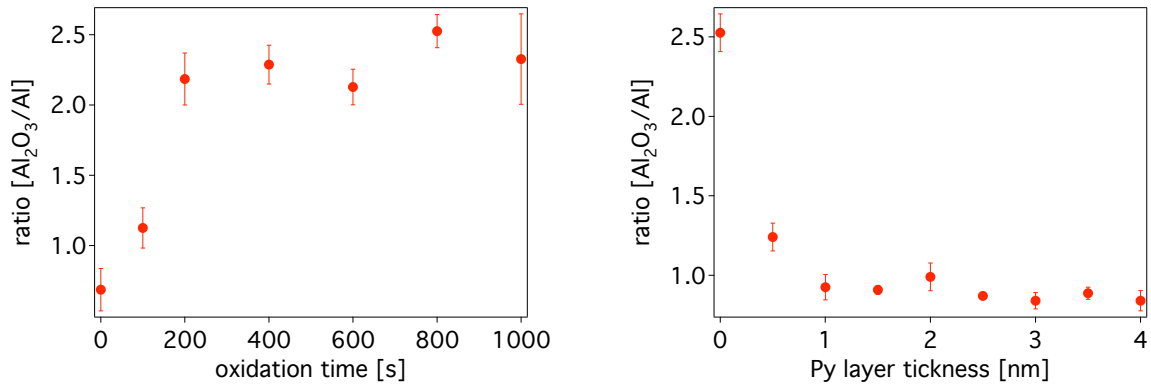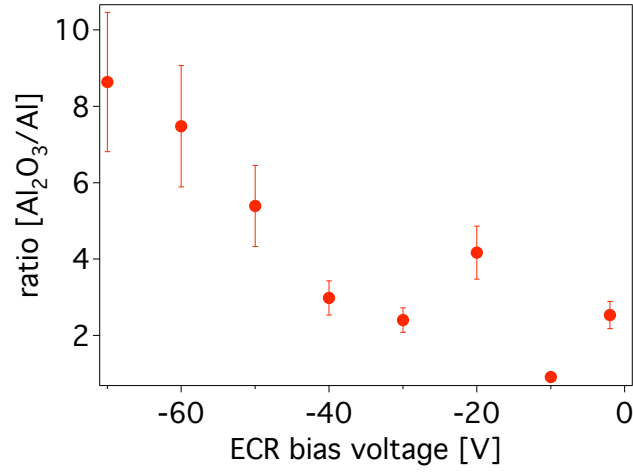
Figure 4.2: Ratio of Aluminium oxide to Aluminium determined by Auger depth profiling. Left: ratio vs. oxidation time without Permalloy. Right: ratio vs. Permalloy thickness, oxidation time 800 s. Layer stack Cu30 (nm)/ Py4/ Mn-Ir15/ Co-Fe3/ Al1.4/ Py x/ Al1.4.

possible.

There are a few possibilities to increase the oxidation depth. One option is to increase the temperature during oxidation. Aluminium needs a temperature of more than $300\,^{\circ}C$ to increase the oxidation depth [150], section 3.4 shows that this is not possible. The second option is to increase the microwave power of the ECR plasma oxidation (above the usual 275 W), but no significant improvement is found. Section 3.3 already showed the influence of the bias voltage on the oxidation and the characteristics of the magnetic tunnel junctions. Now this technique is used to increase the oxidation depth.

To determine the bias voltage dependence, samples of the type Cu30 (nm)/ Py4/ Mn-Ir15/ Co-Fe3/ Al1.4/ Py 1.5/ Al1.4 are prepared. Figure 4.3 shows the result of this investigation. A bias voltage of $-70\,V$ leads to an enormous increment of the Al_2O_3 ratio. Due to the higher penetration depth of the Ions the oxidation depth is also increased. But section 3.3 clearly showed that this also leads to a destruction of the TMR elements (at only 100 s ion bombardment). The Auger depth profile of the $-70\,V$ sample also shows the destruction of the layer structure. It can be concluded that it is not possible to deposit enough oxygen in the Al1.4/ Py 1.5/ Al1.4 layer stack without destruction of the layer structure. In DBJs the Py layer must be even thicker, 1.5 nm Permalloy are not ferromagnetic.

Therefore, the complete oxidation of double barrier junctions with a Permalloy middle electrode is not further investigated, but an Iron interlayer introduced, because Iron has (compared to Nickel) a larger formation enthalpy [146]. Additionally, it could by possible to produce the half metallic Fe_3O_4 with a predicted spin polarisation of 100 % [151].

Figure 4.3: Dependence of the ratio of Aluminium oxide to Aluminium determined by Auger depth profiling on the ECR bias voltage. The oxidation time is always 800 s. Layer stack Cu30 (nm)/ Py4/ Mn-Ir15/ Co-Fe3/ Al1.4/ Py 1.5/ Al1.4.

4.1.2   Iron interlayer

To investigate double barrier junctions prepared by complete oxidation and with Iron inter-layer, samples of the type Cu30(nm)/ Mn-Ir15/ Co-Fe3/ Al1.4/ Fe x/ Al0.8 are made. The top Aluminium layer thickness is reduced to simplify the deposition of Oxygen in the stack, but it is still possible to prepare a working magnetic tunnel junction [42]. Now, analogue to the samples with Permalloy interlayer, the oxidation of the layer stack with 6 nm Iron thickness is investigated leading to a ECR bias voltage of -10 V, 275 W microwave power, and an oxidation time of 200 s. With these parameters it is possible to prepare samples with the correct Oxygen/ Aluminium ratio and the parameter are compatible with MTJs (cf. 3.3).

This result is very promising. In contrast to the DBJs with Permalloy interlayer it is possible to oxidise 'through' the Iron and deposit Oxygen in the lower Aluminium layer. Therefore, it is interesting to examine the second preparation step: The reduction of the Iron. The industrial production of Iron uses Aluminium to reduce the Iron oxide, but this process is realised at very high temperatures of 1800 °C [152]. In contrast to this the used TMR samples sustain a temperature of 300 °C (see section 3.4). Nevertheless, the following investigations will answer the question, if it is possible to reduce the Iron at lower temperatures [147].

The samples are annealed up to 500 °C to investigate the reduction. Magnetic measurements are done to determine the magnetic behaviour of the samples, since metallic Iron is ferromagnetic, Fe_3O_4 ferrimagnetic, and Fe_2O_3/FeO paramagnetic. MOKE measurements of the samples exhibit only a hysteresis loop of the pinned Co-Fe layer, but no indication
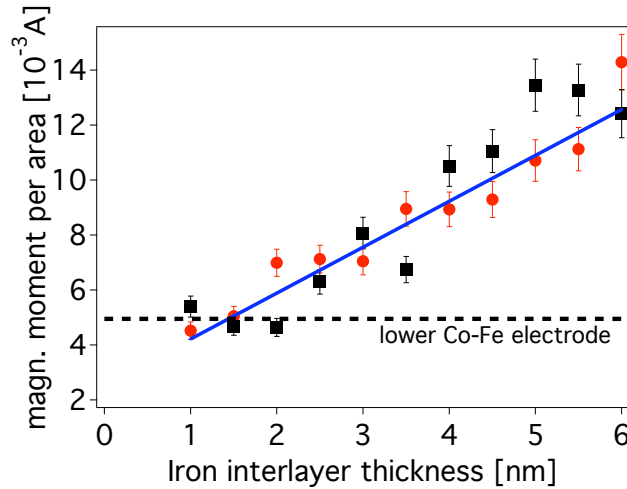
Figure 4.4: Normalised magnetic moment in an annealed double barrier junction (red 200 °C, black 400 °C). The blue line corresponds to a fit described in the text, the broken line corresponds to the magnetisation value of the lower Co-Fe electrode. Layer stack: Cu30(nm)/ Mn-Ir15/ Co-Fe3/ Al1.4/ Fe x/ Al0.8.

of a free Iron layer.

It is possible to think about at least two different explanations to understand this behaviour: The Iron is not ferromagnetic or it couples at the Co-Fe/ Mn-Ir double layer. The Iron is not ferromagnetic if it is (a) not reduced and still oxidised, (b) mixed/ alloyed with the Aluminium because Aluminium-Iron with more than 30 % Al is not ferromagnetic [153]. To separate these different effects from each other, the absolute magnetic moment of the layer stack is measured by AGM. If the Iron is still oxidised or alloyed there is no ferromagnetic signal, but if the reduced Iron couples with the Co-Fe the signal is increased.

Figure 4.4 shows the result of the samples annealed at 200 resp. 400 °C. The ferromagnetic signal is increasing with increasing the Iron interlayer thickness. The fit returns a slope of $1.67 \pm 0.08 \, \text{mA/nm}$ in agreement with Iron (bulk) found in literature: $1.7 \, \text{mA/nm}$ [154]. But already the value at 1 nm Fe corresponds to the magnetic moment of the bottom Co-Fe electrode [76]. This leads to the conclusion, that 1-2 nm Iron form an alloy/ mixture with the Aluminium or are still oxidised and the rest is coupled at the bottom Co-Fe electrode.

Figure 4.5 shows the major loop of an Iron DBJ prepared by complete oxidation and thermal anneal. Only two magnetic contributions are visible, the TMR ratio is 0.3 % at room temperature and 2.7 % at 10 K and the IV curve (not shown) clearly indicates a tunnelling process. Auger measurements indicate that the upper tunnel barrier is oxidised, but the lower barrier is destroyed probably due to the diffusion processes. The Iron is reduced, but the layer structure of the lower Aluminium and the Iron disappeared.

In summary, DBJs with Permalloy and Iron interlayer are prepared. In the Permalloy
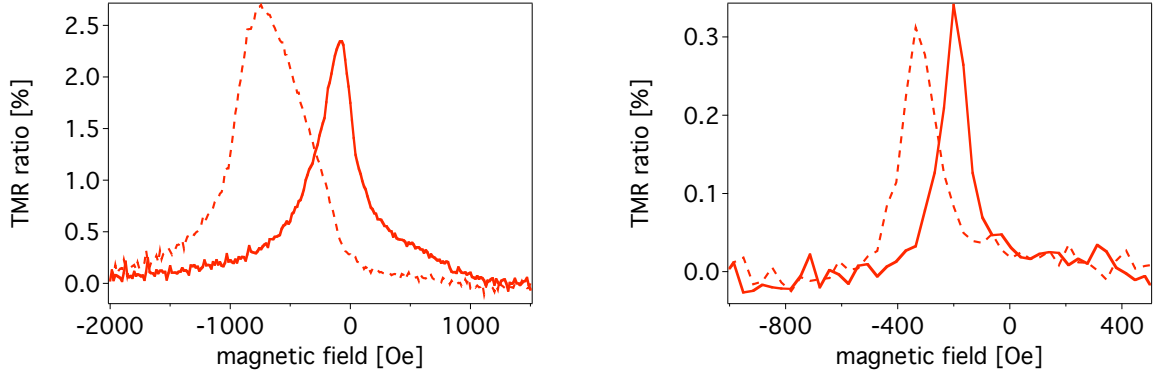
Figure 4.5: Magnetoresistance major loop of a double barrier junction prepared by complete oxidation and thermal annealing (1h @ 250 °C) at 10 K (left) and room temperature (right). Layer stack: Cu30(nm)/ Mn-Ir15/ Co-Fe3/ Al1.4/ Fe 4/ Al1.4/ Co-Fe6/ Mn-Ir11/ Ta3/ Cu55/ Au20.

samples, it is not possible to oxidise through the Permalloy layer at appropriate parameters. In double barrier junctions with Iron interlayer, it is possible to deposit enough Oxygen in the layer stack. Additionally, it is possible to reduce the Iron oxide to metallic Iron without destroying the upper tunnelling barrier. But the lower layer structure is changed and the Iron is partially alloyed with the Aluminium and magnetically partially coupled to the lower Co-Fe electrode. Therefore, further investigations with different materials could lead to a system, where the third condition (besides the oxidation and reduction) of an unchanged layer structure is also fulfilled.

4.2   Preparation by successive deposition and oxidation

In this section, the double barrier junctions prepared by successive steps of Aluminium deposition and oxidation are investigated. The base layer stack consists of Cu 30/ Py = $Ni_{80}Fe_{20}$ 4/ $Mn_{83}Ir_{17}$ 15/ $Co_{70}Fe_{30}$ 3/ Al 1.4 + Oxidation (all values in nm) on top of a thermally oxidized (100 nm) silicon wafer. As already discussed in detail, in SBJs 4 nm Py forms the top electrode, covered with Ta 3/ Cu 55/ Au 20.

In DBJs, Py with variable thickness forms the middle electrode followed by a second tunnel barrier (Al 1.4+Ox) and a 6 nm Co-Fe top electrode. Both oxidations are made with pure oxygen in a remote electron cyclotron resonance plasma with the same set of standard parameters (see section 3.3). The upper Co-Fe is also exchange biased by 11 nm Ir-Mn and again covered with Ta 3/ Cu 55/ Au 20. To activate the exchange biasing, the layer stack is annealed after sputtering at 523 K for ∼2 minutes in a magnetic field of
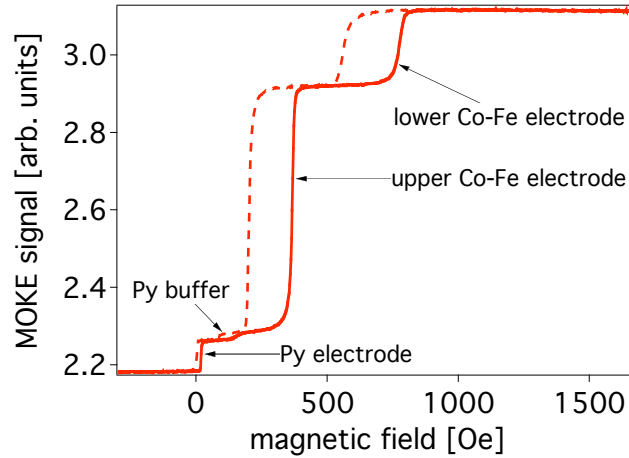
Figure 4.6: MOKE measurement of a double barrier junction with 4 nm Permalloy interlayer. It is possible to separate the 3 magnetic states from each other. Layer stack: Cu30 (nm)/ Py4/ Mn-Ir15/ Co-Fe3/ Al1.4 + Ox./ Py4/ Al1.4 + Ox./ Co-Fe6/ Mn-Ir11/ Ta.

1000 Oe. The layer thickness of the upper and lower Co-Fe electrode and the corresponding Mn-Ir thickness are optimised to have 3 clearly separated magnetic states using the results of section 3.2. Figure 4.6 shows the MOKE measurement of the described layer stack.

All measurements were done by conventional two probe technique without accessing the floating middle electrode. Also using magneto optical Kerr effect measurements of the layer stack up to the second tunnel barrier, a ferromagnetic limit of the Permalloy layer on top of the aluminum oxide of about 2 nm was found. In this section only permalloy interlayers with a larger thickness are investigated.

Because DBJs need two identical tunnel barriers, reproducibility is important for preparing the TMR layer stacks. The prepared reference SBJs show a mean TMR ratio ($\pm$ standard deviation) of 46.3 $\pm$ 1.7 % at room temperature and up to 73 % at 10 K, the mean value of the area-resistance of the barrier is 17.7 M$\Omega \mu$m^2. The Brinkman [16] fit (see section 1.2) with an effective electron mass of 0.4 m$_e$ [21] gives a mean barrier height of 2.9 $\pm$ 0.1 eV and an effective barrier thickness of 1.8 $\pm$ 0.1 nm, which is reasonable: the nominal aluminum oxide thickness should be 1.8 - 2.0 nm, the barrier asymmetry is -0.2 ± 0.3 eV.

To investigate the behaviour of a double barrier junction in principle, two single barrier junctions on one wafer are contacted. The current flows through the first barrier, the lower electrode, and then again through the second barrier. The distance between these two elements is about 100 μm. No ballistic or spin accumulation effects should be visible and a simple serial connection of the two tunnel elements is expected.

Figure 4.7 shows exactly that behaviour. The major loop of the two serially connected junctions fits precisely the addition of the two previously measured single junctions. The
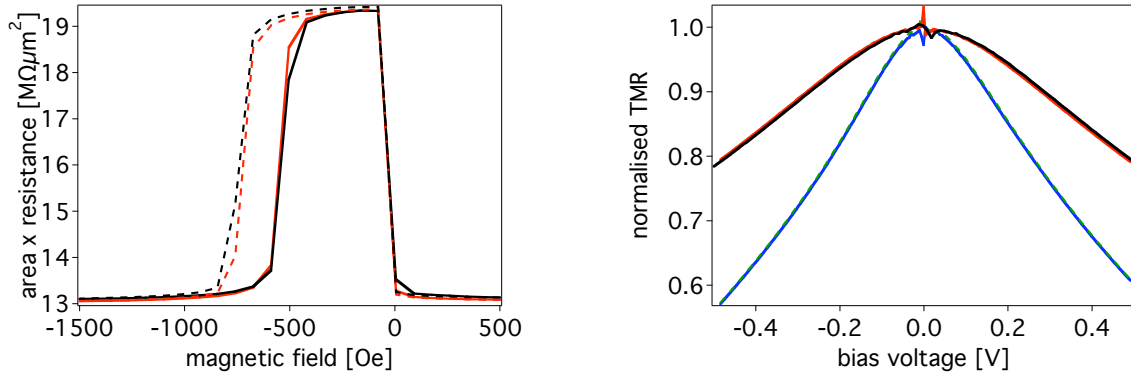
Figure 4.7: Two magnetic tunnel junctions are measured, then serially connected and measured again. The plot shows the added (black) measurements and the measured (red line) 'double barrier' junction. Left: Major loop, the single measurements are not shown. Right: TMR ratio vs. bias voltage. The two lower curves are used for the summation.

dependence of the TMR vs. the bias voltage is also reasonable. The calculated dependence also fits the measurement. The curves for the two used single barrier junctions are additionally plotted in the right figure.

Next, 'real' double barrrier junctions are investigated. Figure 4.8 shows a typical major loop of a DBJ (7 nm Py interlayer) with its three switching states. The DBJs show a TMR ratio of up to 38 % at room temperature (57 % @ 10K). An unchanged TMR ratio for a DBJ is expected, if (a) the spin polarization of all three electrodes is the same, (b) the tunnel electrons do not lose spin information during tunnelling and (c) there is no ballistic contribution. Thus, the smaller value of the TMR ratio in DBJs compared to SBJs has to be contributed to other effects discussed in the following parts.

The absence of ballistic effects in DBJs can be understood by calculating the contribution of the ballistic to the total current. This calculation was carried out for Co/ Al_2O_3 1.5/ Co 2/ Al_2O_3 1.5/ Co junctions at 30 mV bias voltage solving the Schrödinger equation of this system for free electrons for (a) the parallel and (b) the antiparallel state. Whereas the TMR amplitude raises from 44 % for usual tunneling to 115 % for ballistic transport, the ballistic current is a factor of 10^7 smaller than the diffusive part. This ratio can be improved, but it is not possible to reach comparable values for both currents. Thus, the larger TMR of the ballistic current is always masked by the diffusive part. The ballistic contributions are taken at voltages which do not exhibit a resonant quantum well enhancement. Both effects can clearly be discriminated from each other at T = 0 K.

To explain the discrepancy to the TMR amplitude of maximum 38 % (38 % 7 nm, 30 % 4 nm, 32 % 2.5 nm) in DBJs, the data are evaluated within a simple serial resistor model. The resistance R of the DBJ is always the sum of the resistances of the lower (R_1) and top (R_2) SBJ. The evaluation is based on the fact that the process preparing the first tunnel
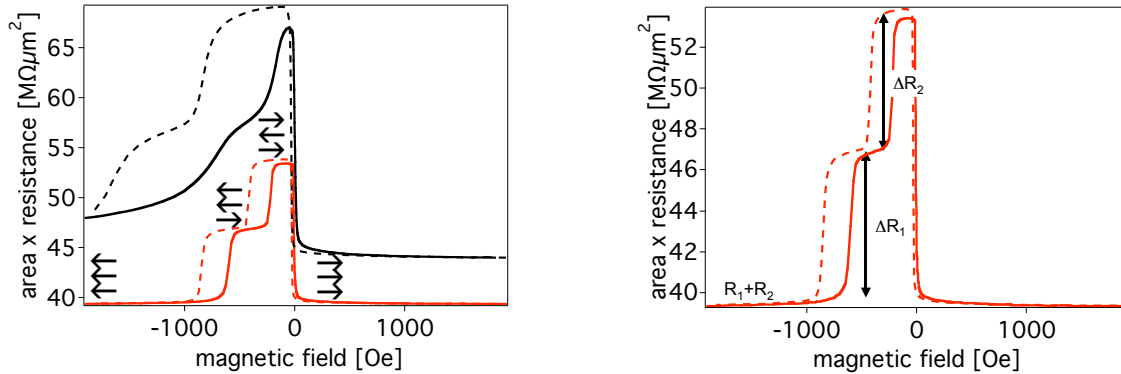
Figure 4.8: Left: Magnetoresistance of a double barrier junction with 7 nm Permalloy interlayer at 10 K (black curve) and room temperature (red curve). The arrows show the magnetic states of the three electrodes (field sweep from plus to minus). Right: The same double barrier junction with variables used in the text.

barrier is very reproducible and gives TMR amplitudes of 46.3 % with a standard deviation of only 1.7 %.

With this value, it is possible to separate the parameters of both barriers yielding the resistances and the TMR values of each junction independently. The known TMR amplitude of the lower junction is the only input parameter, because the absolute resistance change of every junctions can be read from the plot and the relative resistance change ΔR_1 is assumed to be 46.3 %: $\Delta R_1/0.463 = R_1$. Then, it is possible to calculate $R_2 = R - R_1$ (in saturation) and so on. The evaluation finally leads to a TMR ratio of the upper junction of about 20 % for 2.5 and 4 nm Py thickness and about 33 % for 7 nm. This also leads to reasonable resistances: 7 nm Permalloy interlayer for example gives $17.1 \, \mathrm{M\Omega\mu m^2}$ (lower barrier) and $22.8 \, \mathrm{M\Omega\mu m^2}$ (top barrier).

The consistency of the serial resistor model becomes clear by the bias voltage dependence plotted in fig. 4.9. The experimental fixing of the TMR amplitude of the first barrier enables the separation and leads to roughly the same resistance values for both barriers in every DBJ. Then, the voltage drop at each junction should be half of the bias voltage. Figure 2 shows exactly this behavior: The normalized TMR reaches ~ 0.77 at 500 mV for all of the DBJ compared to 0.77 at 240 mV for the reference SBJ.

Contrary to reference [62], we interpret the small deviations in the IV-characteristics for different Py interlayer thickness to be within the reproducibility error. This error is quite low in our junctions although small deviations of the barrier thickness do exponentially influence their resistances. No significant additional complex behaviour has been seen. Therefore, it is not necessary to use a more sophisticated model for (e.g.) ballistic electrons.

Although the TMR ratio of the double barrier junction with the highest TMR ratio so far (7 nm Py, 38 %) is lower at 10 mV bias voltage compared to the SBJ (highest TMR
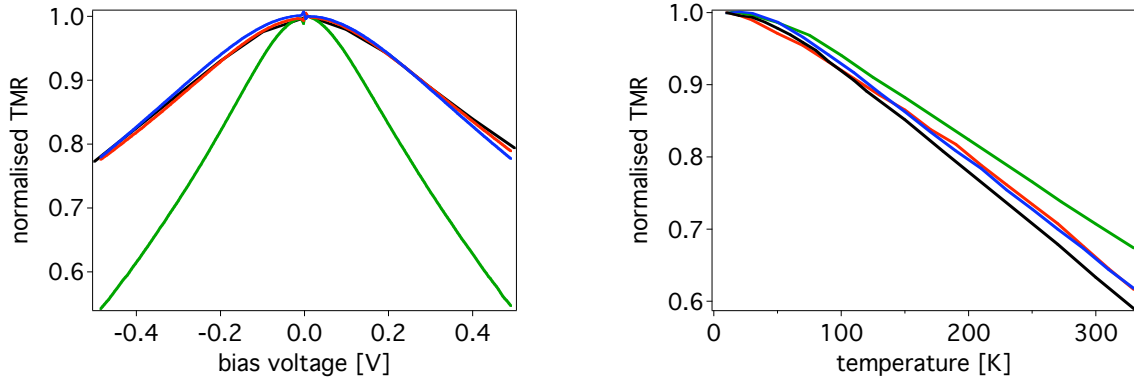
Figure 4.9: Bias voltage (left, room temperature) and temperature dependence (right) of the normalised TMR ratio in double barrier junctions with different Permalloy interlayer thickness and a reference junction. Reference single barrier junction green, 2.5 nm Py interlayer red, 4 nm black and 7 nm blue.

ratio 52 %), the value at 500 mV is 29 resp. 27 %. This improvement of the TMR value in the DBJ at appropriate bias voltages is very interesting for use in applications [62], if it is possible also to increase the TMR ratio of the top barrier to about 50 % (e.g. by using a different middle electrode with better growing conditions due to decreased roughness).

As already mentioned, ballistic effects can be excluded at room temperature. These effects, however, are characterized by a strong temperature dependence due to an increased spin scattering length at lower temperatures (4.3 ± 1.0 nm in Permalloy at low temperatures [155]). The TMR decrease with increasing temperature would be stronger than in a SBJ, because the contribution of the ballistic electrons on the TMR decreases.

This is not the case (fig. 4.9). No significantly different temperature dependence, as reported in [156], can be found. The slightly stronger decrease can be attributed to an enhanced spin independent tunneling current in the top barrier, which is also indicated by the lower TMR effect. Additionally, there is no systematic dependence on the Permalloy interlayer thickness, as it should be with ballistic electrons. Thus, the total temperature dependence is a weighted addition of the two single barrier junctions. The behaviour in figure 4.9 can again be explained by a serial connection of the two barriers in the DBJ.

Further experiments should show the contributions and the size of the ballistic current. This will be done with two different approaches. (a) The Permalloy interlayer is replaced by a Copper layer between the two tunnel barriers. In this structure no 'normal' TMR is present and only ballistic and/ or spin accumulation effects are visible. First experiments already show a very small TMR ratio clearly attributed to the magnetic behavior of the magnetic top and bottom electrodes. This is discussed in section 4.3.

(b) With a more sophisticated lithography process it is possible to apply a voltage at the Permalloy middle electrode. Then, both barriers can be measured separately and the

ballistic current and its magneto resistance can be shown by applying ground at the middle electrode, for example.

In summary, double barrier junctions with TMR values up to $38\,\%$ are prepared. The bias voltage dependence can be explained as a series of two single barrier junctions, leading to a drop of TMR vs. bias voltage to half of the single junctions. In addition, the temperature dependence of the double barrier junctions can be understood assuming only diffusive transport, even for small interlayer thickness. The improved bias voltage dependence in double barrier junctions leads to a larger TMR at higher voltages and thus DBJs seem to be promising candidates for applications. The results of this section are published in [157].
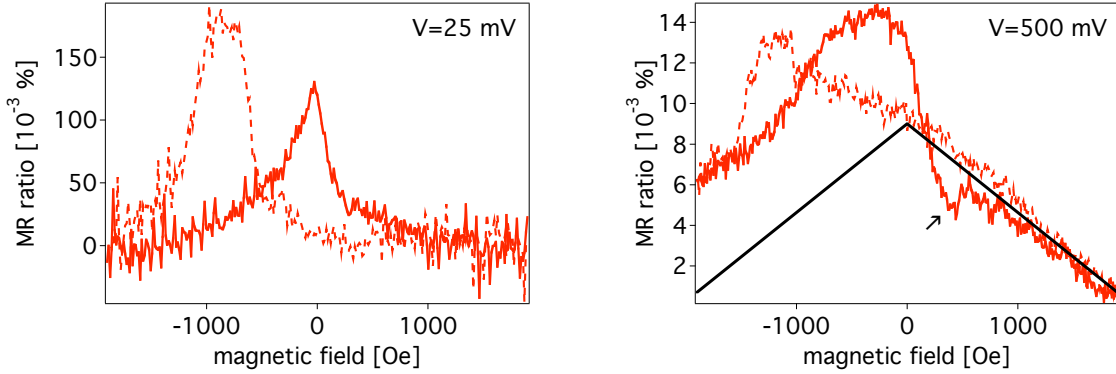
4.3 Copper interlayer

In this section, we again investigated double barrier junctions. The junctions are also prepared by successive steps of Aluminium deposition and oxidation. In the last section diffusive transport dominated the magnetoresistance. It is not necessary to assume ballistic transport or spin accumulation. But it is still possible, that a very small ballistic current or spin accumulation effect exists. To make this current visible, a Copper interlayer replaces the middle electrode in this section. Because both (serially connected) MTJs show no TMR effect [32], only the other effects are visible.

The investigation of the magnetic properties (section 3.2) showed that the Permalloy buffer below the Iridium Manganese is not necessary. So the base layer stack consists of Cu 30/ $Mn_{83}Ir_{17}$ 15/ $Co_{70}Fe_{30}$ 3/ Al 1.4 + Oxidation (all values in nm) on top of a thermally oxidized (100 nm) silicon wafer. In Cu DBJs, Cu with variable thickness forms the middle electrode followed by a second tunnel barrier (Al 1.4+Ox), an exchange biased Co-Fe 6 top electrode, and Ta 3/ Cu 55/ Au 20. To activate the exchange biasing, the layer stack is annealed after sputtering at $523\,\mathrm{K}$ for 2 minutes in a magnetic field of $1000\,\mathrm{Oe}$.

Copper double barrier junctions with interlayer thickness of 1-7 nm are prepared. All the presented measurements are done at $10\,\mathrm{K}$, the lowest temperature accessible with our measurement equipment. The junctions with a Cu layer thickness above $3\,\mathrm{nm}$ showed (within our measurement resolution) no magnetoresistive effect attributed to the magnetic switching of the bottom and top electrodes. Only the triangular baseline shown in figure 4.10 is always visible and increases with increasing bias voltage. The reason for this increase is unclear at present, but could be attributed to the paramagnetic behaviour of the Copper middle electrode.

Figure 4.10 shows the major loops of Copper double barrier junctions with 1 and $3\,\mathrm{nm}$ Copper middle electrode. Three different effects can be seen: the already mentioned triangular baseline, two peaks and in the right figure a very small negative dip in the curve. The bias voltage dependence of the triangle is clearly visible. The left figure shows a measurement at $25\,\mathrm{mV}$ bias voltage, the right figure a measurement at $500\,\mathrm{mV}$.

The two peaks are attributed to the magnetic switching behaviour of the bottom and top electrode controlled by MOKE measurements. These measurements also show a strong magnetic stray field interaction between the two exchange biased electrodes. Future ex-
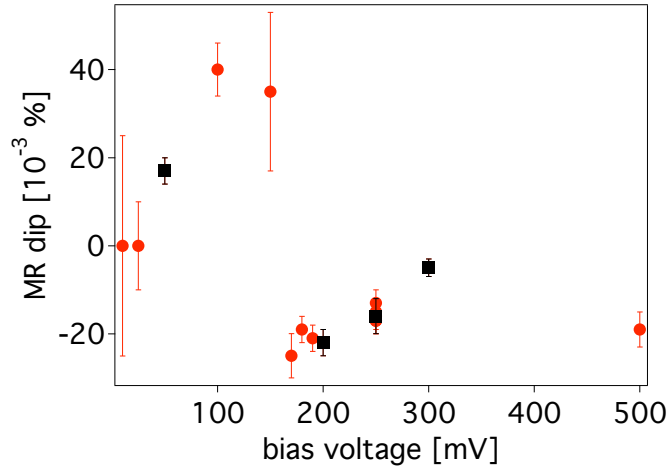
Figure 4.10: Major loops of two double barrier junctions with a copper interlayer at 10 K. Layer stack: Cu30 (nm)/ Mn-Ir15/ Co-Fe3/ Al1.4 + Ox./ Cu 1(left) resp. 3(right)/ Al1.4 + Ox./ Co-Fe6/ Mn-Ir11/ Ta3/ Cu55/ Au20. Please note the dip marked with an arrow and the triangular baseline.

periments will use only a exchange biased bottom electrode. Without a magnetic middle electrode there is no need to separate 3 states from each other and the 'normal' SBJ switching can be used (a simple Co-Fe or Ni-Fe top electrode).

Furthermore, the MR ratio of the peaks depends on the interlayer thickness. The 1 nm (2 nm, 3 nm) Cu DBJs show 0.15 % (0.05 %, 0.01 %) MR ratio. All DBJs have a doubled resistance compared to MTJs, a proof for a layer structure. Due to the decreased area, the resistance is much higher in granular systems. Double barrier junctions with a thicker interlayer show no peaks (resp. they are below the measurement resolution of 0.001 %). It is possible to explain this MR effect by spin accumulation effects in the middle electrode or by ballistic tunnelling through both barriers. Without accessing the middle electrode, there is no experimental way to separate these two explanations. Future experiments will access the middle electrode in DBJs with Permalloy as well as with Copper interlayer. Because the effects are so small, spurious effects like anisotropic magneto resistance (AMR) of the two magnetic electrodes are also imaginable (although, the AMR effect would not depend on the interlayer thickness at all).

The third and probably most interesting feature of the Copper double barrier junctions is the small dip marked in figure 4.10 with an arrow. This dip turned out to be bias voltage dependent, the amplitude of the dip in a 2 nm Cu DBJ in dependence on the bias voltage is shown in figure 4.11. This can can be described by one period of an oscillation with decreasing amplitude. Although, the investigated effects are very close to the resolution of the measurement equipment, the result is quite obvious. To prove that, the measurements are made in random order and at several voltages repeated. Furthermore, four single measurements are shown in figure 4.12 and 4.13 at the end of this paragraph.

This bias voltage dependence could be explained by defined electronic states at certain

Figure 4.11: Size of the dip marked in figure 4.10 in dependence on the bias voltage in a double barrier junction with a 2 nm Copper interlayer at 10 K. One period of an oscillation with decreasing amplitude is visible. The dips of the four black squares are presented in figure 4.12 and 4.13. Layer stack: Cu30 (nm)/ Mn-Ir15/ Co-Fe3/ Al1.4 + Ox./ Cu 2/ Al1.4 + Ox./ Co-Fe6/ Mn-Ir11/ Ta3/ Cu55/ Au20.

energy levels in any electrode. This electrode is most likely the Copper middle electrode, because it is a nearly 2 dimensional system (2 nm Copper leads to only 7 monolayers). However, this oscillation is very surprising, because of the lateral dimensions of $200 \times 200 \, \mu m^2$ and the non-epitaxial growth of the prepared systems. The roughness of all layers should de-phase all effects

In summary, double barrier junctions with different Copper interlayer thickness are investigated. An MR effect attributed to the magnetic switching behaviour of the two magnetic electrodes is found. This effect is strongly dependent on the Copper thickness. This could be explained by spin accumulation effects and/ or ballistic electrons. Taking the suggested explanation of section 3.7 into acccount, only ballistic electrons can explain the observed behaviour. Furthermore, a second smaller MR effect is found, oscillating with the applied voltage. Future experiments with access to the middle electrode and/ or at lower temperatures will uncover the origin of the oscillation and the MR effect.
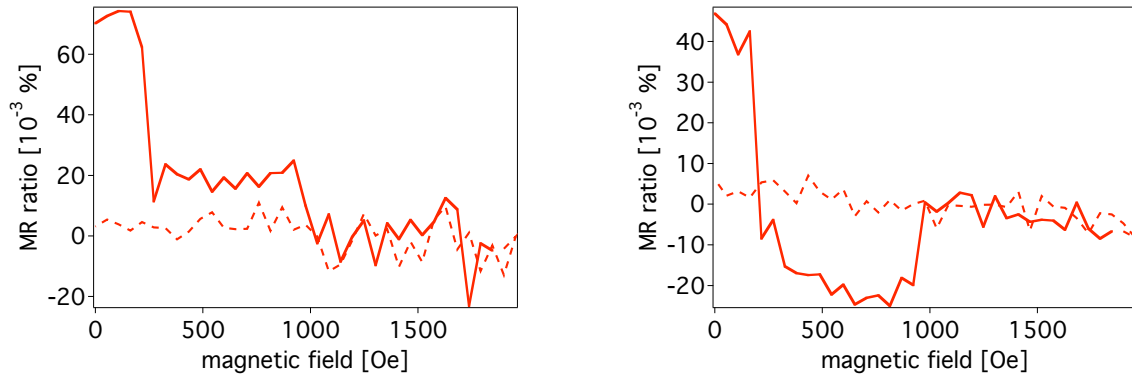
Figure 4.12: The dips of a double barrier junction with 2 nm Copper interlayer at 10 K, left 50 mV and right 200 mV bias voltage. Layer stack: Cu30 (nm)/ Mn-Ir15/ Co-Fe3/ Al1.4 + Ox./ Cu 2/ Al1.4 + Ox./ Co-Fe6/ Mn-Ir11/ Ta3/ Cu55/ Au20.
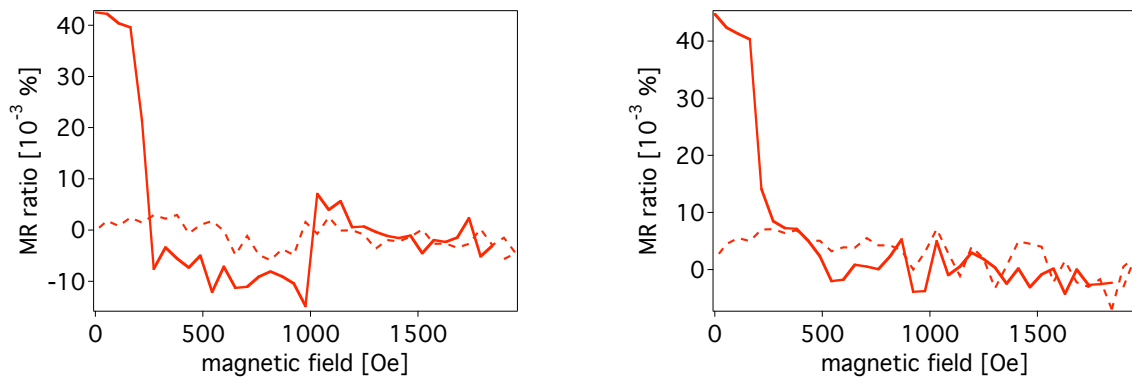
Figure 4.13: The dips of a double barrier junction with 2 nm Copper interlayer at 10 K, left 250 mV and right 300 mV bias voltage. Layer stack: Cu30 (nm)/ Mn-Ir15/ Co-Fe3/ Al1.4 + Ox./ Cu 2/ Al1.4 + Ox./ Co-Fe6/ Mn-Ir11/ Ta3/ Cu55/ Au20.

Chapter 5

Summary

Basics

In the first chapter the basics of tunnel magneto resistance are explained and the used definitions are introduced. The BRINKMAN model shows, how to obtain the barrier parameters (height, thickness and asymmetry) from the IV-curve. The JULLIERE model connects the spin polarisation of the used ferromagnet with the measured TMR ratios. These values can be compared to those received by other techniques like spin polarised tunnelling in a ferromagnet/ insulator/ superconductor junction, Andreev reflection, photo-emission or calculated density of states in the ferromagnet. The last part explains current crowding effects and how to avoid them and gives a simple model for exchange bias.

Preparation and characterisation techniques

In the second chapter the used preparation and characterisation techniques are presented. This includes transport measurements (at low temperatures) and the magnetic characterisation by alternating gradient magnetometer and magneto optical Kerr effect. The structural properties are investigated using Auger electron spectroscopy, atomic force microscopy and X-ray diffraction. The sample preparation is done by a magnetron sputter system with oxidation chamber. The base layer stack consists of Copper on top of a thermally oxidised Silicon-wafer and a Permalloy seed layer, followed by the anti-ferromagnet Iridium-Manganese, the exchange biased bottom Cobalt-Iron electrode, the Aluminium-oxide tunnel barrier, the Permalloy top electrode and some protection and conducting layers. A vacuum furnace is used to activate the exchange bias. Finally, an optical lithography system and an ion beam milling machine define the junctions.

Magnetic tunnel junctions

The structural properties of the magnetic tunnel junctions are investigated by X-ray diffraction measurements. The bottom Copper layer shows a weak (111)-texture. The Iridium-Manganese is deposited by rf-sputtering to lead to a stronger (111)-texture and larger

crystallites, increasing the exchange bias. Because the reference spectra of the γMn are missing in literature, it was not possible to determine its structure*.

The magnetic properties of the exchange biased layer stack are also investigated. It is possible to tailor the magnetic properties and completely separate the hysteresis loops of the two magnetic electrodes. The maximum surface coupling energy $J_{\text{ex}} = 0.27\,\text{mJ/m}^2$ can be further increased by using higher annealing temperatures to $J_{\text{ex}} = 0.32\,\text{mJ/m}^2$ (in accordance with literature).

Thereafter, the magneto-static orange peel (or Neel) coupling between the two ferromagnetic electrodes is measured. These values obtained by magneto optical Kerr effect measurements are compared to a model introduced by KOOLS using the RMS roughness and waviness of the layers. The calculated values strongly overestimate the experimental ones. This behaviour is always found in literature. To take the non-perfect roughness correlation between top and bottom barrier interface into account, this model is extended by a correlation factor. This correlation factor leads to a very good agreement between data and calculation and this factor is reasonable, because it is not expected to find perfectly correlated roughness of two different layers.

To oxidise the Aluminium layer, an ECR plasma oxidation source is used. This fabrication technique allows an additional DC substrate bias, enabling the control of the energy of the ions bombarding the Aluminium film. An ion energy between $3.3\,\text{eV}$ and $10\,\text{eV}$ leads to a high TMR ratio of $73\,\%$ at $10\,\text{K}$ and a barrier height of $2.8\,\text{eV}$. At these energies an optimum oxidation of the Aluminium film is obtained without oxidising the underlying electrode. By varying the oxidation time, the resistance can be tailored, maintaining the high TMR ratio. At larger energies, the results give evidence for an over-oxidation, the barrier becomes thicker and the height is reduced. This is accompanied by an extremely large area resistance and strongly reduced TMR ratios.

Investigating the annealing temperature behaviour of the prepared samples, two main diffusion processes are found by Auger depth profile measurements. The first is the accumulation of the Copper at the barrier at 400°C. The second is the accumulation of Manganese at the barrier from the antiferromagnetic Ir-Mn layer that pins the bottom electrode. This process already starts at 275°C. The result of this structural change is also visible in the magnetic properties. The coercive field of the bottom Co-Fe electrode is increased to up to 4 times of its initial value. The change of the effective spin polarisation of the bottom electrode leads also to a decrease of the TMR ratio. A third indicator is the change of the barrier properties obtained by the Brinkman-fit.

Also the dependence of the TMR ratio on low temperatures is investigated. Assuming the Bloch $T^{3/2}$ law and the Julliere model for the spin polarisation, only spin-wave (magnon) excitations can not explain the strong decay between $10\,\text{K}$ and $330\,\text{K}$ and an un-physically high Curie temperature is found. The fundamental question remains, if the application of Julliere's model and Bloch's law are justified. If so, one has to take the spin-independent conductance into account. This conductance could originate from phonon emission or absorption due to 2 state hopping, for example. But it is not necessary to

---

*Assuming the same peak positions compared to IrMn_3 (also cubic), it is strongly (111)-textured.

assume hopping to explain the temperature dependence of the TMR ratio. Different contributions in different models can also describe the temperature dependence of the TMR ratio, even without inelastic processes.

The noise properties of magnetic and non-magnetic tunnel junctions prepared in 3 different laboratories are investigated. $1/f$ and white noise was found in the investigated frequency range of 1 Hz to 10 kHz. The $1/f$ noise at 10 Hz and 100 mV scaled with the product of area and resistance. This is promising from the application point of view, but it has to be further investigated to determine its origin.

Finally, the polarisation of different ferromagnetic electrodes is investigated. The polarisation of $Co_{70}Fe_{30}$ is found to be 0.43 at room temperature (0.50 at 10 K). The polarisation of Nickel is much lower: 0.23 (0.28). The big difference between these two materials is used to determine the spin polarisation decay length of the tunnelling electrons. Therefore, magnetic tunnel junctions are prepared with a composite top electrode consisting of 4 nm Cobalt-Iron and a Nickel interlayer with variable thickness. The spin polarisation decay length of the tunnelling electrons propagating from the Cobalt-Iron into the Nickel layer and through the barrier is found to be 4.0 ± 0.3 nm at 10 K. A new concept is presented, explaining the conflicting results of very recent spin-injection experiments through a tunnel barrier into a non-ferromagnetic semiconductor or metal and the experiment with composite electrodes.

Double barrier junctions

Double barrier junctions with Permalloy and Iron interlayer are prepared using only one oxidation step. In the first case, it is not possible to oxidise deeper than the Permalloy layer at appropriate parameters. In double barrier junctions with Iron interlayer it is possible to deposit enough Oxygen in the layer stack. The Iron oxide is successfully reduced to metallic Iron and it is possible to keep the upper tunnelling barrier intact, but the lower layer structure is changed. Investigations of the physical properties of different ferromagnetic materials show no other promising candidate. Therefore, this is not further investigated at this time.

Double barrier junctions with TMR values of up to 38 % are prepared using successive steps of Aluminium deposition and oxidation. The bias voltage dependence can be explained as a series of two single barrier junctions, leading to a drop of TMR vs. bias voltage to half of the single junctions. In addition, the temperature dependence of the double barrier junctions can be understood assuming only diffusive transport, even for different interlayer thickness. The improved bias voltage dependence in double barrier junctions results in a larger TMR ratio at higher voltages. Thus, DBJs seem to be promising candidates for applications.

Double barrier junctions with different Copper interlayer thickness are also investigated. An MR effect attributed to the magnetic switching behaviour of the two magnetic electrodes is found. This effect is strongly dependent on the Copper thickness. This could be explained by spin accumulation effects and/ or ballistic electrons. Furthermore, a second smaller MR effect is found, oscillating with the applied voltage.
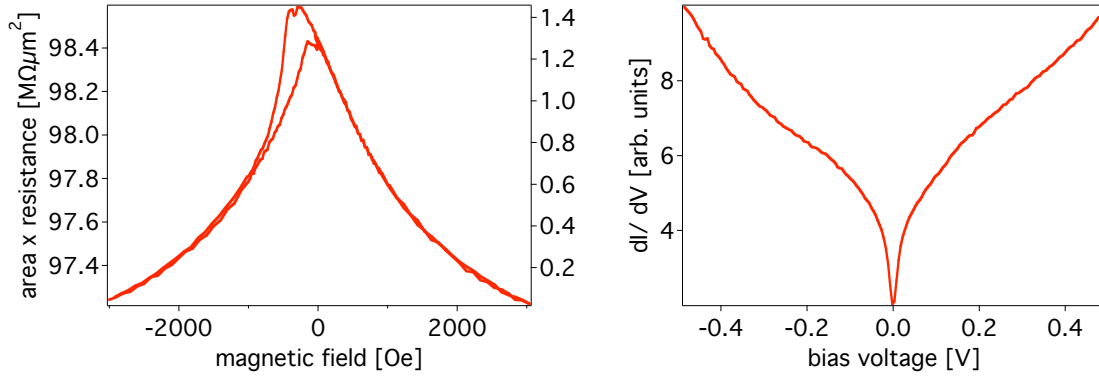
Figure 5.1: Proof of concept: Magnetic double barrier junction with a granular Ni-Fe interlayer (nominal layer thickness 1 nm). Magneto-resistance loop at room temperature shows the superparamagnetic behaviour of the interlayer [43] (left) and IV curve at 10 K shows Coulomb blockade effects [158].

Outlook

Some investigations in this thesis brought up new questions. The extension of the KOOLS model, explaining the orange peel coupling quantitatively, has to be proven. This is already in progress. Magnetic tunnel junctions with different ferromagnetic materials and different barrier thickness/ roughness are investigated. There are also new questions concerning the noise and its origin in magnetic tunnel junctions. Although, the TMR ratio is the most sensible indicator for the barrier quality, the $1/f$ noise depends more on the area-resistance product. Magnetic tunnel junctions with intentionally changed barrier properties (higher/ lower resistance, interface dusting) might show the physical origin of this behaviour.

The most exciting topics presented in this thesis are certainly the Ni/ Co-Fe composite electrodes and the DBJs with a Copper interlayer. The composite electrodes show a long spin polarisation decay length of 4 nm. Although no structural changes could be found, the annealing process might still be a uncertainty. Therefore an equivalent set of samples will be prepared with magnetic masks and without any annealing step. This is also in progress. The introduced model explaining spin-injection experiments through a tunnel barrier has to be put onto a solid foundation (or disproved).

All investigations of the copper DBJs might rather belong to the outlook than to the experimental part. The recent results show the interesting behaviour of these devices. This work is continued by BRINKMANN. Future experiments with access to the middle electrode and/ or at lower temperatures will show the origin of the oscillation and the MR effect. The last figure (5.1) in this thesis illustrates the interesting properties of double barrier junctions with granular (ferromagnetic) interlayer. This field still exhibits a lot of possible experiments such as investigation of co-tunnelling or Coulomb-blockade effects (cf. [158]).

Bibliography

[1] M. Julliere, Phys. Lett. **54A**, 225 (1975).

[2] M. N. Baibich *et al.*, Phys. Rev. Lett. **61**, 2472 (1988).

[3] G. Binasch, P. Grünberg, F. Saurenbach, and W. Zinn, Phys. Rev. B **39**, 4828 (1989).

[4] J. S. Moodera, L. R. Kinder, T. M. Wong, and R. Meservey, Phys. Rev. Lett. **74**, 3273 (1995).

[5] T. Miyazaki and N. Tezuka, J. Magn. Magn. Mater. **139**, 231 (1995).

[6] S. Mengel, *XMR-Technologien* (VDI-Technologiezentrum, 1997).

[7] J. Wecker and J. Bangert, *Magnetische Schichtsysteme* (Forschungszentrum Jülich, 1999), chap. D6: Nichtflüchtige Datenspeicherung in magnetischen Tunnelelementen: Das Magnetic Random Access Memory (MRAM).

[8] C. B. Duke, *Tunneling in solids* (Academic Press, 1969).

[9] E. L. Wolf, *Principles of electron tunneling spectroscopy* (Oxford University Press, 1985).

[10] J. G. Simmons, J. Appl. Phys. **34**, 238 (1963).

[11] J. G. Simmons, J. Appl. Phys. **34**, 1793 (1963).

[12] J. G. Simmons, J. Appl. Phys. **34**, 2581 (1963).

[13] R. Stratton, J. Phys. Chem. Solids **23**, 1177 (1962).

[14] R. H. Fowler and L. Nordheim, Proc. Roy. Soc. **A119**, 173 (1928).

[15] E. L. Murphy and R. H. Good jr., Phys. Rev. **102**, 1464 (1956).

[16] W. F. Brinkman, R. C. Dynes, and J. M. Rowell, J. Appl. Phys. **41**, 1915 (1970).

[17] Messiah, *Quantenmechanik I* (de Gruyter, 1976).

[18] W. A. Harrison, Phys. Rev. **123**, 85 (1961).

[19] J. Schmalhorst, PhD thesis, University of Bielefeld, 2001.

[20] W. H. Press, B. Flannery, S. Teukolsky, and W. Vetterling, *Numerical Recipes in C* (Cambridge University Press, 1988).

[21] A. M. Bratkovky, Phys. Rev. B **56**, 2344 (1997).

[22] J. Bardeen, L. N. Cooper, and J. R. Schrieffer, Phys. Rev **106**, 162 (1957).

[23] J. Bardeen, L. N. Cooper, and J. R. Schrieffer, Phys. Rev. **108**, 1157 (1957).

[24] I. Giaever, Phys. Rev. Lett. **5**, 147 (1960).

[25] I. Giaever, Phys. Rev. Lett. **5**, 464 (1960).

[26] P. M. Tedrow and R. Meservey, Phys. Rev. Lett. **27**, 919 (1971).

[27] R. Meservey and P. M. Tedrow, Phys. Rep. **238**, 173 (1994).

[28] Andreev, Sov. Phys. JETP **37**, 5015 (1988).

[29] D. A. Papaconstantopoulos, *Handbook of the Band Structures of Elemental Solids* (Plenum, New York, 1986).

[30] M. B. Stearns, J. Magn. Magn. Mater. **8**, 167 (1977).

[31] E. Y. Tsymbal and D. G. Pettifor, J. Phys. Cond. Mat. **9**, L411 (1997).

[32] P. R. LeClair, PhD thesis, University of Eindhoven, 2002.

[33] R. J. Pedersen and J. F. L. Vernon, Appl. Phys. Lett. **10**, 29 (1967).

[34] R. van de Verdonk, J. Nowak, R. Meservey, J. S. Moodera, and W. J. M. de Jonge, Appl. Phys. Lett. **71**, 2839 (1997).

[35] A. Fert and C. Vouille, *Magnetische Schichtsysteme* (Forschungszentrum Jülich, 1999), chap. D1: Magnetoresistance overview: AMR, GMR, TMR, CMR.

[36] W. H. Meiklejohn and C. P. Bean, Phys. Rev. **102**, 1413 (1956).

[37] W. H. Meiklejohn and C. P. Bean, Phys. Rev. **105**, 904 (1957).

[38] J. Nogues and I. K. Schuller, J. Magn. Magn. Mater. **192**, 203 (1999).

[39] A. E. Berkowitz and K. Takano, J. Magn. Magn. Mater. **200**, 552 (1999).

[40] U. Nowak, K. D. Usadel, J. Keller, P. Miltenyi, B. Beschoten, and G. Günterodt, Phys. Rev. B **66**, 014430 (2002).

[41] J. Keller, P. Miltenyi, B. Beschoten, G. Günterodt, U. Nowak, and K. D. Usadel, Phys. Rev. B **66**, 014431 (2002).

[42] M. Justus, PhD thesis, University of Bielefeld, 2003.

[43] A. Thomas, Diploma thesis, University of Bielefeld, 2000.

[44] D. Meyners, University of Bielefeld, personal notification.

[45] Keithley instruments model 2000 multimeter user's manual, 1994, chap. A Specifications.

[46] Instruction manual for bos/s power supply, chap. 7 Maintenance and calibration.

[47] Cio-dda06 user's manual, chap. 6 specifications.

[48] Bell model 6010 gauss/ tesla meter instruction manual, sec. 2 specifications.

[49] Oxford instruments operators handbook ccc1100 and ccc1104, October 2000, sec. 2 specification and data.

[50] D. Sudfeld, Examensarbeit, 2000, University of Bielefeld.

[51] P. S. Bechthold, *Magnetische Schichtsysteme* (Forschungszentrum Jülich, 1999), chap. C8: Magnetooptische Effekte: Phänomenologische Beschreibung und Anwendungen.

[52] Technical documentation of micromag model 2900.

[53] D. Briggs and M. P. Seah, *Practical Surface Analysis* (Wiley & Sons, 1990), chap. 4.

[54] Digital instruments, Microscope instruction manual.

[55] Allresist ar-p 535 and 5350, 2003, Specifications.

[56] X. F. Han, M. Oogane, T. Daibou, K. Yaoita, Y. Ando, H. Kubota, and T. Miyazaki, J. Magn. Soc. Japan **25**, 707 (2001).

[57] G. Andersen, Y. Huai, and L. Miloslawsky, J. Appl. Phys. **87**, 6989 (2000).

[58] M. Pakala, G. Anderson, and L. Miloslawsky, J. Appl. Phys. **87**, 6653 (2000).

[59] M. Mao *et al.*, IEEE Trans. Magn. **35**, 3913 (1999).

[60] H. Kikuchi, M. Sato, and K. Kobayashi, J. Appl. Phys. **87**, 6055 (2000).

[61] N. F. Hiromi, K. Saito, Y. Kamiguchi, H. Iwasaki, and M. Sahashi, J. Appl. Phys. **81**, 4004 (1997).

[62] Y. Saito, M. Amano, K. Nakajima, S. Takahashi, and M. Sagoi, J. Magn. Magn. Mater. **223**, 293 (2001).

[63] K. Yagami, M. Tsunoda, and M. Takahashi, J. Appl. Phys. **89**, 6609 (2001).

[64] M. Hayashi, Y. Ando, and T. Miyazaki, Jpn. J. Appl Phys. **40**, 1317 (2001).

[65] H. Brückl, University of Bielefeld, personal notification.

[66] W. Bond and W. L. Kaiser, J. Phys. Chem. Solids **16**, 44 (1960).

[67] C. Yeh et. al., Phys. Rev. B **46**, 10086 (1992).

[68] C. Kittel, *Introduction to solid state physics* (John Wiley, 1976).

[69] Swanson and Tatge, Natl. Bur. Stand. (U. S.), 1953, Circ. 539, I, 15.

[70] R. Nakatani, H. Hoshiya, K. Hoshino, and Y. Sugita, J. Magn. Magn. Mater. **173**, 321 (1997).

[71] T. B. Massalski, *Binary alloy phase diagrams* (ASM International, 1996).

[72] Smith and Yu, Penn. State University, University Park, Pennsylvania, USA, 1975, ICDD Grant-in-Aid.

[73] S. Yuasa et. al., Europhys. Lett. **52**, 344 (2000).

[74] J. Wecker, Siemens AG, personal notification.

[75] M. B. Stearns and Y. Cheng, J. Appl. Phys. **75**, 6895 (1994).

[76] G. Güntherodt and U. Rüdiger, *Magnetische Schichtsysteme* (Forschungszentrum Jülich, 1999), chap. A9: Magnetische Festkörper: ein Überblick.

[77] J. van Driel, F. R. de Boer, K.-M. H. Lenssen, and R. Coehoorn, J. Appl. Phys. **88**, 975 (2000).

[78] R. Jungblut, R. Coehoorn, M. T. Johnson, J. aan de Stegge, and A. Reinders, J. Appl. Phys. **75**, 6659 (1994).

[79] M. Urbaniak, J. Schmalhorst, A. Thomas, H. Brückl, G. Reiss, T. Lucinski, and F. Stobiecki, Unidirectional anisotropy in MnIr/ CoFe/ Al_2O_3/ NiFe tmr multilayer systems, submitted to physica solidi B, accepted for publication.

[80] J. S. Moodera and G. Mathon, J. Magn. Magn. Mater. **200**, 248 (1999).

[81] M. Tsunoda, K. Nishikawa, S. Ogata, and M. Takahashi, Appl. Phys. Lett. **80**, 3135 (2002).

[82] Y.-H. Fan et. al., University of Bielefeld, in preparation.

[83] J. S. Moodera, Massachusetts Institute of Technology, Ni 46 %, unpublished.

[84] S. Kämmerer, University of Bielefeld, Co_2SiMn 50 %, presented 2003 in Madrid.

[85] J. C. S. Kools, W. Kula, D. Mauri, and T. Lin, J. Appl. Phys. **85**, 4466 (1999).

[86] L. Neel, Comtes. Rendus **255**, 1676 (1962).

[87] J. Zhang and R. M. White, IEEE Trans. Magn. **30**, 4630 (1996).

[88] H. Kyung *et al.*, J. Appl. Phys. **89**, 2752 (2001).

[89] S. Iura, K. Yaoita, C. C. Yu, H. Kubota, and T. Miyazaki, J. Phys. D **79**, 3744 (1997).

[90] H. Kubota, T. Watabe, Y. Fukumoto, and T. Miyazaki, J. Magn. Soc. Japan **23**, 67 (1999).

[91] X.-F. Han, M. Oogane, H. Kubota, Y. Ando, and T. Miyazaki, Appl. Phys. Lett. **77**, 283 (2000).

[92] S. S. P. Parkin *et al.*, J. Appl. Phys. **85**, 5828 (1999).

[93] U. May, K. Samm, H. Kittur, J. Hauch, R. Calarco, U. Rüdiger, and G. Güntherodt, Appl. Phys. Lett. **78**, 2026 (2001).

[94] Z. G. Zhang, P. P. Freitas, A. R. Ramos, N. P. Barradas, and J. C. Soares, J. Appl. Phys. **91**, 8786 (2002).

[95] J. M. Daughton, J. Appl. Phys. **81**, 3758 (1997).

[96] P. Friedel and S. Gourrier, J. Phys. Chem. Solids **44**, 353 (1983).

[97] A. M. Bratkovsky, Appl. Phys. Lett. **72**, 2334 (1998).

[98] S. S. P. Parkin, International Symposium on Nanoscale Magnetism and Transport, Sendai, 2000.

[99] B. F. P. Roos, P. A. Beck, S. O. Demokritov, B. Hillebrands, and D. Ozkaya, J. Appl. Phys. **89**, 6656 (2001).

[100] A. Thomas, H. Brückl, M. D. Sacher, J. Schmalhorst, and G. Reiss, Aluminum oxidation by a remote electron cyclotron resonance plasma in magnetic tunnel junctions, J. Vac. Sci. Technol. B, accepted for publication October 2003.

[101] M. D. Sacher, Diploma thesis, University of Bielefeld, 2002.

[102] S. Cardoso, P. P. Freitas, C. de Jesus, P. Wei, and J. C. Soares, Appl. Phys. Lett. **76**, 610 (2000).

[103] P. J. Cumpson and M. P. Seah, Surf. Interface Anal. **25**, 430 (1997).

[104] R. C. Sousa, J. J. Sun, V. Soares, P. P. Freitas, A. Kling, M. F. da Silva, and J. C. Soares, Appl. Phys. Lett. **73**, 3288 (1998).

[105] S. Tehrani, J. M. Slaughter, E. Chen, M. Darlam, J. Shi, and M. de Herrera, IEEE Trans. Magn. **35**, 2814 (1999).

[106] B. R. Strohmeier, D. E. Leyden, R. S. Field, and D. M. Hercules, J. Catal. **94**, 514 (1985).

[107] M. Lo-Jacono and M. Schiavello, *Preparation of Catalysts* (Elsevier, Amsterdam, 1976).

[108] J. S. Moodera, J. Nowak, and R. J. M. van de Verdonk, Phys. Rev. Lett. **80**, 2941 (1998).

[109] A. H. MacDonald, T. Jungwirth, and M. Kasner, Phys. Rev. Lett. **81**, 705 (1998).

[110] C. H. Shang, J. Nowak, R. Jansen, and J. S. Moodera, Phys. Rev. B **58**, R2917 (1998).

[111] R. Meservey, D. Pereskevopoulos, and P. M. Tedrow, Phys. Rev. Lett. **37**, 858 (1976).

[112] B. Nadgorny *et al.*, Phys. Rev. B **61**, 3788 (2000).

[113] A. Vedyayev, D. Bagrets, A. Bagrets, and B. Dieny, Phys. Rev. B **63**, 64429 (2001).

[114] F. Guinea, Phys. Rev. B **58**, 9212 (1998).

[115] A. H. Davis, J. M. MacLaren, and P. LeClair, J. Appl. Phys. **89**, 7567 (2001).

[116] S. Zhang, P. M. Levy, A. C. Marley, and S. S. P. Parkin, Phys. Rev. Lett. **79**, 3744 (1997).

[117] D. T. Pierce, R. J. Celotta, J. Unguris, and H. C. Siegmann, Phys. Rev. B **26**, 2566 (1982).

[118] H. C. Siegmann, J. Phys. D **4**, 8395 (1992).

[119] V. Skumryev, S. Stoyanov, Y. Zhang, G. Hadjipanayis, D. Givord, and J. Nogues, nature **423**, 850 (2003).

[120] M. J. Buckingham, *Noise in electronic devices and systems* (Ellis Horwood, Chichester, West Sussex, UK, 1983).

[121] E. R. Nowak, R. D. Merithew, M. B. Weissman, I. Bloom, and S. S. P. Parkin, J. Appl. Phys. **84**, 6195 (1998).

[122] E. R. Nowak, M. B. Weissman, and S. S. P. Parkin, Appl. Phys. Lett. **74**, 600 (1999).

[123] S. Ingvarsson, J. Appl. Phys. **85**, 5270 (1999).

[124] S. Ingvarsson, G. Xiao, S. S. P. Parkin, W. J. Gallagher, G. Grinstein, and R. H. Koch, Phys. Rev. Lett. **85**, 3289 (2000).

[125] E. R. Nowak, P. Spradling, M. B. Weissman, and S. S. P. Parkin, Thin Solid Films **377-378**, 699 (2000).

[126] K. S. Kim, H. J. Shim, I. J. Hwang, B. K. Cho, J. H. Seok, and J.-T. Kim, J. Appl. Phys. **91**, 8804 (2002).

[127] M. Tondra, Non Volatile Electronics, in preparation.

[128] D. Song et. al., J. Appl. Phys. **87**, 5197 (2000).

[129] W. K. Park, J. S. Moodera, J. Taylor, M. Tondra, J. M. Daughton, A. Thomas, and H. Brückl, J. Appl. Phys. **93**, 7020 (2003).

[130] P. M. Tedrow and R. Meservey, Solid State. Commun. **16**, 71 (1975).

[131] P. LeClair, H. J. M. Swatgen, J. T. Kohlhepp, R. J. M. van de Veerdonk, and W. J. M. de Jonge, Phys. Rev. Lett. **84**, 2933 (2000).

[132] S. Yuasa, T. Nagahama, and Y. Suzuki, Science **297**, 234 (2002).

[133] F. J. Jedema, A. T. Filip, and B. J. van Wees, Nature **410**, 345 (2001).

[134] C. H. Ho, M.-T. Lin, Y. D. Yao, S. F. Lee, C. C. Liao, F. R. Chen, and J. J. Kai, J. Appl. Phys. **90**, 6222 (2001).

[135] T. Zhu *et al.*, Phys. Rev. B **66**, 094423 (2002).

[136] R. Meservey, Massachusetts Institute of Technology, personal notification.

[137] G. Schmidt, D. Ferrand, L. W. Molenkamp, A. T. Filip, and B. J. van Wees, Phys. Rev. B **62**, R4790 (2000).

[138] E. I. Rashba, Phys. Rev. B **62**, 16267 (2000).

[139] F. J. Jedema, H. B. Heersche, A. T. Filip, J. J. A. Baselmans, and B. J. van Wees, Nature **416**, 713 (2002).

[140] M. Johnson, Nature **416**, 809 (2002).

[141] V. Motsnyi, J. De Boeck, J. Das, W. van Roy, G. Borghs, E. Goovaerts, and V. I. Safarov, Appl. Phys. Lett. **81**, 265 (2002).

[142] T. Manago and H. Akinaga, Appl. Phys. Lett. **81**, 694 (2002).

[143] J. H. Lee *et al.*, J. Magn. Magn. Mater. **240**, 137 (2002).

[144] X. Zhang, B.-Z. Li, G. Su, and F.-C. Pu, Phys. Rev. B **56**, 5484 (1997).

[145] L. Sheng, Y. Chen, H. Y. Teng, and C. S. Ting, Phys. Rev. B **59**, 480 (1999).

[146] J. A. Dean, *Lange's Handbook of Chemistry* (McGraw-Hill Book Company, 1973).

[147] Z. Zhang, S. Cardoso, P. P. Freitas, P. Wei, N. Barradas, and J. C. Soares, Appl. Phys. Lett. **78**, 2911 (2001).

[148] B. F. P. Roos, PhD thesis, University of Kaiserslautern, 2001.

[149] N. Cabrera and N. F. Mott, Rep. Prog. Phys. **12**, 163 (1949).

[150] A. Atkinson, Review of modern physics **57**, 437 (1985).

[151] M. Sharma, C. Fery, S. X. Wang, T. C. Anthony, and J. H. Nickel, submitted to IEEE Trans. Magn.

[152] W. Schröter, K.-H. Lautenschläger, and H. Bibrack, *Taschenbuch der Chemie* (Verlag Harri Deutsch, 1990).

[153] *Metals Handbook* Vol. 8, 8 ed. (American Society for Metals, 1973).

[154] J. K. Watson, *Applications of Magnetism* (John Wiley & Sons, 1980).

[155] S. Dubois, L. Piraux, J. M. George, K. Ounadjela, J. L. Duvail, and A. Fert, Phys. Rev. B **60**, 477 (1999).

[156] J. H. Lee, K. I. Lee, W. L. Lee, K. H. Shin, J. S. Lee, K. Rhie, and B. C. Lee, J. Appl. Phys. **91**, 7956 (2002).

[157] A. Thomas, H. Brückl, J. Schmalhorst, and G. Reiss, Temperature and bias voltage dependence of $CoFe/AlO_x/Py/AlO_x/CoFe$ double barrier junctions, IEEE Trans. Magn., accepted for publication.

[158] P. LeClair and J. S. Moodera, Spin polarized tunneling through nano particles, presented at the ICM conference 2003, Rome, in preparation.

Acknowledgement

I have to thank a lot of people, because without their support this work would not be possible. Particularly, I want to thank my supervisors Dr. HUBERT BRÜCKL (DBJ calculations) and Prof. GÜNTER REISS as well as Dr. ANDREAS HÜTTEN and Dr. WILLI SCHEPPER who all always had time for all discussions relating my work.

Furthermore, I want to thank MARC SACHER (auger, AGM, CLAB600), JAN BORNEMEIER (wedgebonding), JÖRG SCHOTTER (optical lithography), VOLKER GÜTH (computer systems), PATRICK THOMAS (transport measurements) and DIRK MEYNERS (AFM) for measurements and help preparing the samples. Moreover, I thank the mechanical and electronic workshop for the fast and reliable implementation of my plans. I want to thank my colleagues at D2, because I really enjoyed my $4\frac{1}{2}$ years here. I gratefully acknowledge Dr. JAGADEESH S. MOODERA and Dr. WAN KYU PARK for the nice and prolific collaboration concerning the noise measurements.

Most of all I have to thank Dr. JAN SCHMALHORST and Dr. MAIK JUSTUS for their theoretical and practical help and the discussions with them.

Finally, I acknowledge Dr. PATRICK R. LECLAIR, Dr. JAGADEESH S. MOODERA and Dr. ROBERT MESERVEY for discussions relating my results and PETER JAGLOM for corrections of my English text.

Danksagung

Ich möchte mich an dieser Stelle bei allen bedanken, die zu dieser Arbeit beigetragen haben. Das ist zunächst mein Betreuer Hubert Brückl, der mir während meiner gesamten Zeit auf der einen Seite alle Freiheiten gelassen hat, aber andererseits immer Zeit für Diskussionen hatte und viele Ideen zu dieser Arbeit beigesteuert hat. Außerdem möchte ich mich meinem Professor Günter Reiss bedanken, der (zusammen mit Hubert) für die Finanzierung meiner Promotionsstelle und sehr gute Laborausstattung gesorgt hat. Darüber hinaus stand seine Tür und die der anderen Betreuer Andreas Hütten und Willi Schepper immer für alle Fragen offen, bei Andreas möchte ich mich außerdem für seine liebe Hilfe bedanken.

Mein Dank gilt auch allen Kollegen, mit denen ich zusammengearbeitet habe, insbesondere Marc Sacher, Jan Bornemeier, Jörg Schotter, Volker Güth, Patrick Thomas und Dirk Meyners, der diese Arbeit auch korrekturgelesen hat. Dank Euch hat es mir immer Spaß gemacht in Bielefeld zu arbeiten.

Ohne die unglaublich schnelle Hilfe in der Mechanikwerkstatt und die unglaublich

bürokratische Hilfe in der Elektronikwerkstatt wären viele Ideen nicht realisierbar gewesen. Außerdem möchte ich mich bei Wan Kyu Park und Jagadeesh Moodera für die nette Zusammenarbeit bedanken.

Am meisten bedanke ich mich aber bei Jan Schmalhorst und Maik Justus, die mir das nötige Handwerkszeug für erfolgreiches Arbeiten im Labor beigebracht haben.